

---

Electronic Theses and Dissertations, 2004-2019

---

2013

## Computational Approach To The Problems Of Electro- And Photo-catalysis

Sebastian Zuluaga  
*University of Central Florida*



Part of the [Physics Commons](#)

Find similar works at: <https://stars.library.ucf.edu/etd>

University of Central Florida Libraries <http://library.ucf.edu>

This Doctoral Dissertation (Open Access) is brought to you for free and open access by STARS. It has been accepted for inclusion in Electronic Theses and Dissertations, 2004-2019 by an authorized administrator of STARS. For more information, please contact [STARS@ucf.edu](mailto:STARS@ucf.edu).

---

### STARS Citation

Zuluaga, Sebastian, "Computational Approach To The Problems Of Electro- And Photo-catalysis" (2013). *Electronic Theses and Dissertations, 2004-2019*. 2812.

<https://stars.library.ucf.edu/etd/2812>

COMPUTATIONAL APPROACH TO THE PROBLEMS OF ELECTRO- AND  
PHOTO-CATALYSIS

by

SEBASTIAN ZULUAGA  
B.S. Physics Universidad Nacional de Colombia, 2008  
M.S. Physics University of Central Florida, 2010

A dissertation submitted in partial fulfillment of the requirements  
for the degree of Doctor of Philosophy  
in the Department of Physics  
in the College of Science  
at the University of Central Florida  
Orlando, Florida

Summer Term  
2013

Major Professor: Sergey Stolbov

© 2013 Sebastian Zuluaga

## ABSTRACT

The main objective of this work is to gain basis for rational design of catalysts used in fuel cells for conversion of chemical energy stored in hydrogen molecules into electric energy, as well as photo-catalysts used for hydrogen production from water under solar irradiation. This objective is achieved by applying the first principles computational approach to reveal relationship among compositions of materials under consideration, their electronic structure and catalytic activity.

A major part of the work is focused on electro-catalysts for hydrogen fuel cells. Platinum (Pt) is widely used in the electrodes of fuel cells due to its good catalytic properties. However, Pt is an expensive and scarce element, its catalytic activity is not optimal and also it suffers from CO poisoning at anode. Therefore the search for new catalytic materials is needed for large scale implementation of fuel cells. The main direction of search of more efficient electro-catalysts is based in the design in which an active element monoatomic layer (AE) is deposited on a metal substrate (MS) made of a cost-effective material. Two goals are achieved by doing this: on the one hand, the cost of the catalytic system is reduced by reducing the amount of the AE in the system and on the other hand the catalytic properties of the AE can be tuned through its interactions with the MS.

In the first part of this work the Pd-based alloys and layered structures have been studied as promising electro-catalysts for the ORR on the fuel cell cathodes, more precisely Pd-Co alloys and Pd/M/Pd (M=Co,Fe). There exists a robust model linking the activity of a surface toward ORR to computable thermodynamic properties of the system and further to the binding energies

of the ORR intermediates on the catalyst surface. A more challenging task is to find how to tune these binding energies through modification of the surface electronic structure that can be achieved by varying the surface composition and/or morphology. To resolve this challenge, the electronic structure, binding energies of intermediates and the ORR free energies have been calculated within the density functional theory (DFT) approximation. The results presented in this work show that in contrast to the widely accepted notion, the strain exerted by a substrate on AE hardly affects the surface activity toward ORR, while the hybridization of the electronic states of the AE-and MS-electronic states is the key factor controlling the catalytic properties of these systems. Next it is shown that the catalytic activity of the promising anode electrocatalysts, such as Pt/M, M=Au, Ru and Pd, is also determined by the AE-MS hybridization with a minor effect of the strain. Furthermore, we have shown that, if AE is weakly bound to the substrate (as it is for Pt/Au), surface reconstruction occurs. This leads to the breaking of the relation between the electronic structure of the clean surface and the reactivity of the system. Other kind of promising ORR catalysts is designed in the form of Ru nanoparticles modified by chalcogens. In this work, I present the results obtained for small Ru clusters and flat Ru facets modified with chalcogens (S, Se and Te). The O and OH binding energies are chosen as descriptors of the ORR. The results on the two systems are compared, concluding that large clusters with relative large flat facets have higher catalytic activity due to the absence of low coordinated and thus high reactive Ru atoms.

Regarding the problem of the hydrogen production via photo-catalytic splitting of water, one of the challenges is tuning the band gap of the photo-anodes to optimal levels. Graphitic carbon nitride (g-C<sub>3</sub>N<sub>4</sub>) is a promising material to be used as a photo-anode, however, a

reduction of the band gap width by rational doping of the material would improve the efficiency significantly. This issue is addressed in the last chapter of this work. Two problems are considered: a) the stability of the doped system and b) the band gap width. To address the first problem the ab-initio thermodynamics approach has been used, finding that the substitution of C and N with the doping agent (B, C, N, O, Si and P) is thermodynamically preferred over the interstitial addition of dopant to the g-C<sub>3</sub>N<sub>4</sub> structure. However, due to high kinetic energy barriers for the detachment of C and N atoms, involved in the substitution doping, the interstitial addition found to be kinetically more favorable. Since the density functional theory fails to reproduce the band gap of semiconductors correctly, the GW approximation was used to study the band gap of the system. The results indicate that the g-C<sub>3</sub>N<sub>4</sub> system maintain its semiconductor character if doped with B, O and P under certain conditions, while reducing the band gap.

## **ACKNOWLEDGMENTS**

I want to thank my advisor Doctor Sergey Stolbov for his encouragement, advisement and guidance during my Ph.D. I am also grateful to Doctor Talat Rahman and her group for the thoughtful discussion. Special thanks to all my professors and the physics department staff.

Also I would like to thank the UCF EXCEL program and the Physics Department for the financial support.

# TABLE OF CONTENTS

LIST OF FIGURES .....	xi
LIST OF TABLES .....	xviii
CHAPTER 1: INTRODUCTION .....	1
1.1 Conversion of the Hydrogen Chemical Energy Into Electric Power .....	2
1.2 Production of Hydrogen Chemical Energy .....	3
1.3 Thesis Objectives .....	5
CHAPTER 2: THEORETICAL BACKGROUND .....	8
2.1 Many-Body Problem in Condensed Matter .....	8
2.2 Adiabatic Approximation .....	9
2.3 Hartree Approximation .....	10
2.4 Hartree-Fock Approximation .....	15
2.5 Density Functional Theory .....	19
2.5.1 Hohenber– Kohn Theorem .....	20
2.5.2 Kohn– Sham Equations .....	22
2.5.3 Local Density Approximation .....	27
2.5.4 The Gradient Expansion .....	29
2.5.5 Generalized Gradient Approximation .....	30
2.6 GW Approximation .....	31

CHAPTER 3: FIRST PRINCIPLE STUDIES ON CATALYTIC SYSTEMS TOWARDS THE OXYGEN REDUCTION REACTION .....	35
3.1 Introduction .....	35
3.2 Pd-Co Alloy Surfaces.....	40
3.2.1 Computational Details .....	42
3.2.2 Results on O and OH Adsorption With 0.25% Mono Layer Coverage .....	45
3.2.3 Results on Co-Adsorption of the ORR Intermediates and Water.....	46
3.2.4 Reaction Free Energy Diagrams.....	50
3.2.5 Tracing the Reaction Energetics to the Electronic Structure of the Alloys.....	54
3.2.6 Conclusions .....	59
3.3 First Principle Calculations on Pd/X/Pd Sandwich Like Structures .....	60
3.3.1 Computational Details .....	63
3.3.2 Results on the Local Density of States .....	65
3.3.3 Results on O, OH and OOH Binding Energies .....	67
3.3.4 Free Energy Diagrams .....	70
3.3.5 Results on the Stability of the System .....	71
3.3.6 Conclusions .....	74
3.4 Strain and Hybridization Effect on Catalytically Active Monolayers on Metal Substrates	74
3.4.1 Computational Details .....	76

3.4.2 Results on the LDOS .....	77
3.4.3 Results on the system's reactivity towards the OH adsorption .....	80
3.4.4 Conclusions .....	83
3.5 First Principles Studies on Chalcogen Modified Ru Surfaces .....	83
3.5.1 Computational Details .....	86
3.5.2 Results on Chalcogens Binding to the Ru Surface .....	87
3.5.3 O and OH Binding Energy in Presence of Chalcogens .....	93
3.5.4 Conclusions .....	97
3.6 First Principle Studies of the Size and Shape Effects on the Reactivity of the Se Modified Ru Nanoparticles .....	98
3.6.1 Computational Details .....	100
3.6.2 Geometry and General Results on the Ru Nanoparticles .....	101
3.6.3 Results on the Se Formation Energy and Adsorption on the Ru Nano-Cluster .....	102
3.6.4 Results on the Oxygen Adsorption on the Se Modified Ru Nano-Cluster .....	107
3.6.5 Conclusions .....	110
CHAPTER 4: FIRST PRINCIPLES CALCULATIONS ON PHOTO-CATALYTIC SYSTEMS TOWARDS THE HYDROGEN EVOLUTION .....	112
4.1 Introduction .....	112
4.2 Doping Effects on the Electronic and Geometric Structure of Graphitic C <sub>3</sub> N <sub>4</sub> .....	113

4.2.1 Computational Details .....	115
4.2.2 Formation Energy and Geometry of the doped g-C <sub>3</sub> N <sub>4</sub> System.....	117
4.2.3 Effects on the Electronic Structure of the System due to the Addition of Dopants to the Dangling Bonds in g-C <sub>3</sub> N <sub>4</sub> .....	125
4.2.4 Results on C and N Substitution.....	128
4.2.5 Results on the Effects of Co-Doping.....	132
4.2.6 Conclusions .....	134
LIST OF REFERENCES.....	136

## LIST OF FIGURES

Figure 1: Top view of the surfaces: panel a: Pd(111), panel b: Pd<sub>0.75</sub>Co<sub>0.25</sub>, panel c: Pd<sub>0.5</sub>Co<sub>0.5</sub> and panel d: Pd/Pd<sub>0.75</sub>Co<sub>0.25</sub>. Light grey and dark blue balls represent the Pd and Co atoms, respectively. Black straight lines separate supercells. Black crosses mark the preferred adsorption sites for atomic oxygen. .... 44

Figure 2: The lowest energy configurations for the 0.5 ML hydroxyl adsorption (left panel) and OH–H<sub>2</sub>O co-adsorption (right panel). .... 48

Figure 3: The lowest energy configurations for the 0.5 ML hydroxyl adsorption (left panel) and OH – H<sub>2</sub>O co-adsorption (right panel). .... 49

Figure 4: Reaction free energy diagram built for Pd for the following intermediate adsorption configurations: 0.25 ML coverage of the adsorbates (thick solid lines), O – OH and OH – OH co-adsorption (thin solid lines), O – O and O – OH co-adsorption (dash lines), and O – H<sub>2</sub>O and OH – H<sub>2</sub>O co-adsorption (dash-dot lines). The arrowed line shows the U<sub>0</sub> determining reaction step. .... 51

Figure 5: Reaction free energy diagram built for Pd/Pd<sub>0.25</sub>Co<sub>0.75</sub>. Adsorption configurations and line code is the same as in Figure 4. .... 52

Figure 6: Spin-resolved LDOS of the surface atoms and adsorbed oxygen calculated for Pd<sub>0.25</sub>Co<sub>0.75</sub>. .... 54

Figure 7: Spin-summed LDOS of the surface Pd atom and adsorbed oxygen calculated for Pd(111). .... 55

Figure 8: Spin-summed LDOS of the surface Pd atom and adsorbed oxygen calculated for Pd/Pd<sub>0.25</sub>Co<sub>0.75</sub>(111). .... 57

Figure 9: Spin-summed LDOS of the Pd(111) surface. Pd atom calculated for pure Pd (solid line), Pd/Pd <sub>0.25</sub> Co <sub>0.75</sub> (dash line), Pd <sub>0.25</sub> Co <sub>0.75</sub> (dash-dot-dot line) and Pd <sub>0.5</sub> Co <sub>0.5</sub> (dot line). .....	58
Figure 10: Energy of the Pd d-band center counted for the Fermi-level as a function of the neighboring Co atoms. ....	59
Figure 11: Spin-summed Pd LDOS calculated for Pd/Pd <sub>0.25</sub> Co <sub>0.75</sub> (111) for the surface Pd atoms which have no Co neighbor (solid line) and has one Co neighbor (dash line). ....	59
Figure 12: Spin summed LDOS of d-states Pd atoms on the system surface for clean Pd(111) (black line), Pd/Co/Pd (blue line) and Pd/Fe/Pd (red line). ....	65
Figure 13: Spin resolved d-LDOS. Panel a: Pd/Fe/Pd system. Panel b: Pd/Co/Pd system. Black lines denote the d-states of Pd atoms at the top layer, while red lines denote the d-states of Fe or Co atoms (Fe d-states for panel a and Co d states for panel b) on the second layer. ....	67
Figure 14: Intermediates adsorbed on Pd/Fe/Pd system. Panel a: relaxed OH co-adsorbed with OH on Pd/Fe/Pd (0.5 ML coverage). Panel b: relaxed OH co-adsorbed with H <sub>2</sub> O on Pd/Fe/Pd (0.5 ML coverage). Panel c: relaxed OOH co-adsorbed with H <sub>2</sub> O on Pd/Fe/Pd (0.5 ML coverage). ....	70
Figure 15: ORR free energy diagrams for Pd(111) (black line), Pd/Co/Pd (blue line) and Pd/Fe/Pd (red line) in presence of 0.25 ML of H <sub>2</sub> O. Panel a: U=0 eV, panel b: U=0.548 eV. ....	71
Figure 16: Spin summed d-LDOS of surface Pd atoms on the Pd/Fe/Pd system. Black line corresponds to the pristine Pd/Fe/Pd system. Red line corresponds to the Pd/Fe/Pd system with one O atom in between the Pd and Fe layer (oxidized system). ....	73
Figure 17: Surface Pt atoms d-xy and d-xz LDOS. Left panels: Comparison between Pt/Ru and Pt-contr systems, right panels: Comparison between Pt/Au and Pt-expnd systems. Pt-contr stands	

for Pt slab contracted to the a-parameter of the hcp Ru bulk system, while Pt-expnd stands for Pt slab expanded to the a-parameter of the fcc Au bulk system. .... 77

Figure 18: d-xz LDOS comparison between Pt and Au slabs. Red line: d-xz states of the Au surface atom, black line: d-xz states of the Pt surface atom. .... 79

Figure 19: Band centers changes (respect to Pt slab surface atoms) Vs OH binding energy for Pt/Ru, Pt-contr, Pt, Pt/Au, Pt-expnd. Black line: total d-band center, red line: d-xy band center, green line: d-xz band center. .... 81

Figure 20: OH adsorbed on Pt/M surfaces. Panel a: M=Au, panel b: M=Ru. Grey, yellow, red, blue and light blue spheres denote Pt, Au, O, Ru and H atoms respectively..... 82

Figure 21: Chalcogens formation energy. Hollow symbols denote uniform chalcogen adsorption and solid symbols denote island formation (dimer and trimer). Black, green, blue and red lines denote formation energy of O, S, Se and Te respectively. .... 88

Figure 22: Upper panels: charge density redistribution upon chalcogen adsorption with isosurface set to  $\pm 0.024 e/\text{\AA}^3$ , yellow and blue spots represent excess and depletion of charge respectively. Grey balls represents Ru atoms. Lower panels: total charge density volume used in the Bader analysis with isosurface set to  $0.3 e/\text{\AA}^3$ . Panels a and e correspond to O adsorption, panels b and f corresponds to S adsorption, panels c and g corresponds to Se adsorption and panels d and h corresponds to Te adsorption. .... 90

Figure 23: LDOS for Ru Surface atoms and the adsorbed chalcogen atoms coordinated to the Ru atoms. Panel a: O adsorption, panel b: S adsorption, panel c: Se adsorption, panel d: Te adsorption. Black lines represent the d states of the surface Ru atoms coordinated to the chalcogen atom, while red, green, purple and blue lines denote O, S, Se and Te p states. .... 91

Figure 24: Electronic charge density redistribution upon two chalcogens (S and Te) adsorbed on neighboring hcp sites. Red and blue spots denote accumulation and depletion of charge respectively. Iso-surface value is set to  $0.08 e/\text{\AA}^3$ . Panel a: S atoms adsorption, panel b: Te atoms adsorption. Grey, yellow, and brown spheres denote Ru, S and Te atoms respectively. .... 92

Figure 25: O adsorbed on the chalcogen modified Ru surface. Red, green and gray spheres denote O, chalcogens and Ru atoms. Black lines symbolize the Unit cell. .... 93

Figure 26: Valence charge density redistribution upon adsorption of O, S and Te, isosurface is set to  $0.08 e/\text{\AA}^3$ . Panel a: O and S adsorbed in hcp neighbor sites, panel b: O and Te adsorbed in hcp neighbor sites. Yellow and blue spots denote excess and depletion of charge. Grey, red, yellow and brown balls denote Ru, O and S atoms. .... 96

Figure 27: Surface Ru atoms LDOS, panel a: chalcogens as first neighbors, panel b: chalcogens as second neighbors. Black lines denote Ru atoms with no chalcogen neighbors, while red, orange and blue lines denote Ru atoms with O, S and Te atoms as first or second neighbors respectively. .... 97

Figure 28: Optimized geometric structure of the 105-atom Ru cluster. The inserted numbers provide the binding energies for some Ru atoms..... 101

Figure 29: Relaxed Se/Ru system for 30, 50 and 65% Se coverage over the Ru 105-atoms cluster. .... 103

Figure 30: Se formation energy as a function of the Se coverage. Green line: Ru 105-atoms cluster, black line: Ru(0001) facet. .... 104

Figure 31: Valence charge density redistribution upon Se adsorption on Ru 93- and Ru 105-atom clusters cluster. Yellow spots denote excess of charge, while blue spots denote depletion of

charge. Panel a: Two Se atoms adsorbed on a flat facet of the Ru 93-atom cluster, panels b: Se adsorption around the apex of the Ru 105-atom cluster. The isosurface was set to  $\pm 0.06 \text{ e}/\text{\AA}^3$ . Grey and yellow spheres denote Ru and Se atoms respectively. .... 105

Figure 32: LDOS calculated for Ru atoms with and without Se bonded as first neighbors. Panel a: Ru atom in flat facet of the Ru 93-atom cluster, panel b: Ru atom belonging to the apex of the Ru 105-atom cluster. The black and red lines represent the densities of the Ru d-states calculated for the clean and Se-adsorbed clusters respectively, while the blue lines represent the Se p-states. .... 106

Figure 33: Oxygen adsorption sites on the Ru and Se/Ru 105-atom cluster. .... 107

Figure 34: Electronic charge density redistribution upon Se and O adsorption on Ru clusters, isosurface was set to  $0.04 \text{ e}/\text{\AA}^3$ . Panel a: Ru 93-atoms cluster, panel b: Ru 105-atoms cluster. Yellow and blue spots denote excess and depletion of charge respectively. Grey, red and yellow spheres denote Ru, O and Se atoms respectively. .... 109

Figure 35: G-C<sub>3</sub>N<sub>4</sub> structure. Panel a: Tri-s-triazine structure. Panel b: Valence charge density redistribution upon formation of the system, red and blue spots denotes accumulation and depletion of charge respectively. .... 118

Figure 36: Valence charge density redistribution upon formation of the system where the corner N atom has been replaced by C. Blue and red spots denotes depletion and excess of charge respectively. Grey and brown spheres denote N and C atoms respectively. .... 123

Figure 37: Energy barrier for N border atom detachment and transfer to the nearest dangling bonds. Panel a: detachment and transfer to upper layer dangling bonds. Panel b: detachment and

transfer to in-plane closest dangling bonds. The inserted figures show the position of the N atom in the initial state, while the arrow indicates the position of the N atom in the final state. .... 124

Figure 38: Valence charge density redistribution upon binding of B to the N's dangling bonds. Yellow and blue surfaces denote accumulation and depletion of charge respectively. The isosurface corresponds to  $\pm 0.15 \text{ e/\AA}^3$ . Brown, grey and green spheres denote C, N and B atoms respectively. .... 126

Figure 39: Total DOS for the doped systems under consideration. Panel a: addition of B to the dangling bonds. Panel b: addition of C to the dangling bonds. Panel c: addition of N to the dangling bonds. Panel d: addition of O to the dangling bonds. Panel e: addition of Si to the dangling bonds. Panel f: addition of P to the dangling bonds. .... 127

Figure 40: Projected LDOS for the system where a C atom has been adsorbed on the dangling bonds of  $g\text{-C}_3\text{N}_4$ . Black line:  $p_z$  states, blue line:  $p_x$  states, red line:  $p_y$  states. Panel a: projected LDOS for corner C atom (first C neighbor to the added C atom). Panel b: projected LDOS for border N atom (second N neighbor to the added C atom). Panel c: projected LDOS for border N atom (first N neighbor to the added C atom). .... 128

Figure 41: Total density of states for the system where one C has been replaced by one O atom. Panel a: O replacing corner C atom, no O-N bond is broken, only a small elongation of one of the O-(border N) bond is observed. Panel b: replacement of the middle C atom by O, rupture of one O-N bond is observed, leading to a high distortion of the original  $g\text{-C}_3\text{N}_4$  structure .... 129

Figure 42: Local density of states projection on  $p_x$ ,  $p_y$  and  $p_z$  states. Black lines:  $p_x$  states, red lines  $p_y$  states, green lines  $p_z$  states. Panel a: Local density of states of corner N atom first neighbor to O, panel b: Local density of states of corner N with no O neighbors. .... 130

Figure 43: Total DOS for border N atom replaced by B and P. Panel a: B replacement, panel b: P replacement. Inserted figures show the system's structure..... 131

Figure 44: Middle C atom LDOS. Black, red and green lines denote  $p_x$ ,  $p_y$  and  $p_z$  states respectively. Panel a: middle C atom with no B neighbors, panel b: middle C atom coordinated to one B atom..... 131

Figure 45: DOS comparison between B and P replacing a border N atom. Panel a: B doping, panel b: P doping, panel c: B and P co-doping. The inserted figures show the geometry of the systems under consideration. .... 133

## LIST OF TABLES

Table 1: Binding energies and zero point vibration energies calculated for O and OH adsorbed with 0.25 ML coverage on the preferred sites of the (111) surfaces of Pd and Pd-Co alloys. ....	46
Table 2: Binding energies of O and OH calculated for the co-adsorption configurations. ....	47
Table 3: O, OH and OOH binding and zero point energies for 0.25 ML coverage on Pd, Pd/Co/Pd and Pd/Fe/Pd, on the preferred adsorption site.....	67
Table 4: Binding energies of intermediates co-adsorbed with 0.25 ML coverage of OH and H <sub>2</sub> O, on the preferred adsorption site.....	68
Table 5: Binding energies of OH on Pt, Pt-contr, Pt/Ru, Pt-expnd and Pt/Au systems and the d-band center change of Pt atoms on the surface of these systems. Pt is used as reference for all the numbers.....	80
Table 6: Binding energy of the intermediates, O and OH, on clean Ru and 1/3 chalcogen covered Ru surfaces.....	94
Table 7: Ru surface atoms d-band center with one chalcogen as first neighbor.....	97
Table 8: Se effects on oxygen adsorption on the Ru nanoparticle.....	108
Table 9: Formation energies for B doping at T=298.15 K .....	120
Table 10: Formation energies for C and N self-doping at T=298.15 K.....	121
Table 11: Formation energies for O doping at T=298.15 K.....	121
Table 12: Formation energies for Si doping at T=298.15 K.....	121
Table 13: Formation energies for P doping at T=298.15 K. “*” denotes nonequivalent substitutions of middle C atoms due to the stacking configuration. This nonequivalent	

substitution leads to the higher hybridization between layers and the distortion of the in-plane symmetry of the system. .... 122

## CHAPTER 1: INTRODUCTION

In the past 10 to 15 years, a great progress has been made in application of first principles computational methods to surface science and nano-science. Currently, the first principles calculations are widely used to unveil the nature of novel and technologically important properties of solid surfaces and nanostructures and even to predict materials with desired properties. There are several factors contributed to this progress. First, the dramatically enhanced power of computers (work stations, clusters and high-performance supercomputers) made it feasible to perform the first-principles atomistic calculations for the systems with broken periodicity and low symmetry, such as surfaces and nanoparticles. Second, newly-developed very efficient computer codes utilize the improved, more accurate, first principles approximations. Finally, a number of robust models have been proposed, which link the material properties in question to the computable characteristics, such as electronic structure, vibrational spectra, binding energies of adsorbates. As a result, the first principles computational methods have become a powerful means for understanding the mechanisms underlying phenomena critical for technologically important applications and for design of advanced materials.

Among the most exciting and promising applications of the first principles methods are those related to so-called hydrogen economy that is a cycle comprised of three main stages: a) production of hydrogen, which can be achieved by different means, for example it can be obtained from fossil fuels, thermolysis, or photo-catalytic water splitting; b) storage of hydrogen; and c) conversion of the chemical energy stored in hydrogen molecules into electric energy using hydrogen fuel cells. Note that the product of reactions in the fuel cells is clean water. Therefore,

if hydrogen is produced by the photo-catalytic splitting of water under solar irradiation, it makes a perfectly clean and renewable cycle of energy production. Importantly, all three stages of the cycle work. However, in current designs, some elements of this scheme (mostly catalysts) are too expensive and not quite efficient. New materials are needed to reduce the cost and increase effectiveness of this technology. This is thus not surprising that an enormous effort has been made to discover these materials, and the first principles computational approach is extensively used to provide a basis for the future discoveries.

In this work, first principles methods are applied to understand the relationships between the composition, electronic structure and properties of the key elements of the above scheme, namely, electro-catalysts responsible for the energy conversion in fuel cells and photo-anodes used for the photo-catalytic splitting of water.

### **1.1 Conversion of the Hydrogen Chemical Energy Into Electric Power**

Fuel cells, such as the proton exchange membrane fuel cells (PEMFC) and the direct methanol fuel cells (DMFC) convert the hydrogen chemical energy into electric power. As clean renewable sources of energy they can offer great advantages for various applications, however, a number of obstacles remain to their large scale implementation. First, fuel cells are unacceptably expensive, since the Pt-based catalysts used in both electrodes of the fuel cell, make up a major part of the cost. Search for new electro-catalytic materials with a reduced loading of precious metals is critical for commercialization of PEMFC and DMFC. Second, performance of both PEMFC and DMFC suffers from low rate of the oxygen reduction reaction (ORR) on the Pt

cathode, which decreases the onset potential for ORR ( $\sim 0.9\text{V}$  vs standard hydrogen electrode (SHE), compared to  $1.23\text{ V}$  (SHE) of ideal potential), and hence reduces fuel cell efficiency [1].

Clearly, the great advantages of fuel cells can be efficiently utilized only if the cost of the electrodes is dramatically reduced and their electro-catalytic properties are significantly improved. The search of new electro-catalysts for ORR is conducted in several directions. One of them focuses on the systems including the Pt monolayer deposited on a Pt-free substrate. The Adzic and Mavrikakis research groups combining experimental studies and first principles calculations have made a significant progress in this direction [2, 3, 4, 5, 6]. The authors have found some Pt/M structures with the ORR activity comparable or even higher than that on bulk Pt. These works also provide insight into the mechanisms of formation of the layered surface structures and their effect on the ORR energetics. Since such catalysts are mostly synthesized in the form of the 2 - 5 nm nanoparticles, surface atoms (Pt) make a significant fraction of volume of the nanoparticles. The Pt load is still high, which is a disadvantage of these systems. It is thus not surprising that much effort has been made to find efficient Pt-free electro-catalysts for ORR.

## **1.2 Production of Hydrogen Chemical Energy**

Photo-Catalytic water splitting into its constituents using solar energy is the most interesting and clean way to produce hydrogen. Photo-catalytic materials provide an efficient way to harvest the solar energy converting it into hydrogen chemical energy. However, several obstacles have to be overcome before they are able to compete with other sources of hydrogen.

Photo-catalytic systems split the water molecule by establishing a potential difference between the two electrodes using a photon, in this case a photon coming from the sun. After the potential difference between the electrodes has been established, the process follows as ordinary electrolysis. This sets the first requirement for the photo-catalytic material, since 1.23 eV are needed in order to split the water molecule into its constituents, the photo-catalytic material should be a semiconductor with a band gap higher than 1.23 eV. The second requirement comes from the desire to use the sun as source of photons, the highest intensity in the solar spectrum is reached in the visible range, which spans between 380 and 780 nm. Then a semiconductor with a band gap between 3.26 and 1.59 eV is desired. The third requirement arises from the position of the valence and conduction bands,  $H^+/H_2$  reduction and  $O_2/H_2O$  oxidation potentials should be situated within the band gap of the semiconductor. The fourth requirement deals with the electronic carriers mobility, when the photon is adsorbed on the semiconductor and the electron-hole pair is created, the recombination of the electron hole pair is an undesired effect, then high carrier mobility is preferred. Finally the material should be stable, maintaining its structure through the reaction.

The oxygen evolution was first reported by Boddy[7] in 1968, but was not until 4 years later that Fujishima and Honda[8] reported the photo-electro-chemical water splitting that various semiconductor materials started to be tested as photo-catalysts. Among the several semiconductors studied[9] having desirable band gaps, some of them suffer of having the edge of the valence and conduction band in the wrong position. This is the case of  $MoS_2$ ,  $WO_3$  and  $Fe_2O_3$  among other. On the other hand, materials such as  $TiO_2$ [10, 11] and  $K_3Ta_3B_2O_{12}$ [12, 13] which are very stable materials and highly efficient as photo-catalytic systems, adsorb light only

in the UV range of the solar spectrum. While other materials such as CdS with a band gap of 2.4 eV is not stable. Therefore the search for semiconductor materials with the previously mentioned properties is a topic of extensive research.

### 1.3 Thesis Objectives

The purpose of this thesis is to study and analyze the factors controlling the properties of several electro- and photo-catalytic systems using density functional theory. The results are divided into two chapters (chapters 3 and 4), one containing the analysis of electro-catalytic systems towards the ORR and the second containing the analysis of photo-catalytic systems towards the hydrogen evolution reaction.

In order to study the catalytic activity of the different systems towards the ORR, chapter 3 starts by giving a description of the model used to study this reaction. In order to characterize the catalytic activity of the different systems we used the d-band center model to characterize the O, OH and OOH binding energies, which in turn are used as descriptors of the ORR.

On section 3.2 and 3.3 we discuss, compare and contrast the results obtained for Pd-Co systems. Section 3.2 deals with  $\text{Pd}_{1-x}\text{-Co}_x$  alloys with varying Co concentration  $x = 0, 0.25,$  and  $0.5,$  as well as the  $\text{Pd}_{0.75}\text{Co}_{0.25}(111)$  alloy covered with one monolayer of Pd ( $\text{Pd}/\text{Pd}_{0.75}\text{Co}_{0.25}$ ). The reaction energetics is traced to the electronic structure of the alloy surfaces in order to reveal the main factors controlling the ORR in the system. Based on these results, section 3.3 presents our results on the rational design of two Pd based systems comprised of a Pd substrate followed by a monolayer of Co or Fe and Pd monolayer on top, ( $\text{Pd}/\text{Co}/\text{Pd}$ ) and ( $\text{Pd}/\text{Fe}/\text{Pd}$ ) systems. On

both sections the O, OH and OOH adsorption energies are used as descriptors of the ORR, the electronic structure of the Pd and Co atoms is analyzed, finding the hybridization between Pd and Co atoms the key factor controlling the enhancement in the system catalytic activity.

On section 3.4 we focus on the Pt/MS (MS= Ru, Pt and Au) system, studying and analyzing the strain and hybridization effects and its contributions to the change of the Pt d states. In this section we will use the OH binding energy as a descriptor of the system's catalytic activity towards the ORR.

To conclude with chapter 3, on section 3.5 and 3.6 we present our density functional theory based calculations results explaining the experimentally observed electro catalytic activity towards the ORR enhancement on chalcogen (O, S, Se and Te) modified Ru surfaces and small clusters. On section 3.4 the chalcogen adsorption and island formation is studied. The O adsorption energy is used as a descriptor of the system's electro-catalytic activity toward the ORR and the effect of chalcogens on the Ru(0001) surfaces's catalytic activity is analyzed. On section 3.5 the size and shape effects on the reactivity of the Se modified small Ru nanoparticles (1.2 nm in size Ru nanoparticles) are studied and compared to the results obtained on section 3.4, allowing us to draw conclusions on the ORR process and electronic structure of the experimentally observed 2nm -5nm Ru clusters, where systematic first principles studies are still not feasible.

The photo-catalytic materials topic is addressed on chapter 4, where the band gap of g-C<sub>3</sub>N<sub>4</sub>, which is a promising material to be used as photo-anode, is analyzed. On section 4.2 we study and systematically analyze the changes in the electronic structure of g-C<sub>3</sub>N<sub>4</sub> caused by

doping the system with B, self C and N doping, O, P and Si atoms. These elements were chosen as dopants because they contain the same, or similar, amount of valence electrons as C and N and are expected to be good candidates to replace N or C atom, slightly altering the band gap, without destroying the original system's electronic structure.

## CHAPTER 2: THEORETICAL BACKGROUND

This chapter presents the basic ideas used in solving the many body problem in condensed matter. We will start by stating the quantum many body problem ruled by Schrödinger equation, which in general give rise to a coupled differential equation with many degrees of freedom. On the second section of this chapter we will present the basic ideas of the Born-Oppenheimer approximation where the movement of the ions is decoupled from the movement of the electrons in the system, reducing the number of coupled degrees of freedom in the problem. Next, we present the basic ideas, similarities and differences of the Hartree, Hartree-Fock approximations and Density Functional Theory. To conclude with this chapter the GW formalism is presented.

### 2.1 Many-Body Problem in Condensed Matter

Most of important material properties, such as cohesive energy, character of conductivity and surface reactivity, are determined by behavior of valence electron. The valence electrons are essentially quantum system that can be described using quantum mechanics methods. In particular the electronic states can be found as a solution to the Schrödinger equation

$$\hat{H}\Psi = E\Psi, \tag{2.1}$$

where  $E$  are the eigenvalues and  $\Psi$  the eigenstates. The Hamiltonian used to describe a crystal or a nanoparticle, a collection of nucleus and electrons, follows the general form:

$$\hat{H} = \frac{\hbar^2}{2} \sum_{I=1}^P \frac{1}{M_I} \nabla_I^2 - \frac{\hbar^2}{2m} \sum_{i=1}^N \nabla_i^2 + \frac{e^2}{2} \sum_{I=1}^P \sum_{J \neq I}^P \frac{Z_I Z_J}{|R_I - R_J|} + \frac{e^2}{2} \sum_{i=1}^N \sum_{j \neq i}^N \frac{1}{|r_i - r_j|} - e^2 \sum_{I=1}^P \sum_{i=1}^N \frac{Z_I}{|R_I - r_i|}, \quad (2.2)$$

where  $R_I$  are the coordinate of each one of the  $P$  nucleus,  $M_I$  and  $Z_i$  are their masses and nuclear charges respectively, and  $r_i$  are the coordinates of each one of the  $N$  electrons.

The Schrödinger equation with the Hamiltonian described on (2.2) is a partial differential equation with  $3(N + P)$  coupled degrees of freedom, which cannot be easily decoupled and can be solved analytically only for a few of cases, such as hydrogenoid atoms or the  $H_2^+$  molecule. Systems such as surfaces and nanoparticles may contain hundreds of nucleus and thousands of electrons, in order to solve these we will use several approximations.

## 2.2 Adiabatic Approximation

In order to simplify the above problem, it can be argued that the electrons move much faster than the nucleus. In fact, the ratio of masses between an electron and a proton is  $1/1836$ , which means that velocity of the nucleus would be less than 3 percent of the electron's velocity in the case of the hydrogen atom, when the electron and the nucleus have the same kinetic energy. Then, it is possible to assume that the cloud of electrons surrounding the nucleus reacts instantaneously to its movement, while staying in the ground state for each particular spatial configuration of the nucleus. This allows us to decouple the nucleus wave function and the electronic wave function, and write the total (nucleus plus electron) wave function as the product of these two. This can be summarized in the Born-Oppenheimer approximation[14] as follows:

$$\psi(R, r, t) = \sum_n \theta_n(R, t) \Phi_n(R, r), \quad (2.3)$$

where  $\theta_n(R, t)$  are the wave function of the nucleus while  $\Phi_n(R, r)$  correspond to (the electronic wave functions) the Eigen states of the time independent Schrödinger equation:

$$\hat{h}_e \Phi_n(R, r) = E_n(R) \Phi_n(R, r), \quad (2.4)$$

where the electronic Hamiltonian  $\hat{h}_e$  is given by:

$$\hat{h}_e = -\frac{\hbar^2}{2m} \sum_{i=1}^N \nabla_i^2 - e^2 \sum_{I=1}^P \sum_{i=1}^N \frac{Z_I}{|R_I - r_i|} + \frac{e^2}{2} \sum_{i=1}^N \sum_{j \neq i}^N \frac{1}{|r_i - r_j|}, \quad (2.5)$$

the first term is the kinetic energy contributions, the second term corresponds to the electron-nucleus interaction and the last term takes into account the interaction between electrons. This is still a partial differential equation with  $3N$  coupled degrees of freedom, which cannot be solved exactly. We thus need more approximations.

### 2.3 Hartree Approximation

In 1928 Douglas Rayner Hartree proposed that the total electron wave function can be written as the product of individual one-electron orbitals. He proposed that electrons in an atom will feel what is known as the Self-Consistent Field[15, 16] (HSCF), which is the effective field generated by the nucleus plus the one generated by the other electrons. To describe this idea the total wave electron function was written as:

$$\Phi_n(r) = \prod_{i=1}^N \varphi_i(r_i). \quad (2.6)$$

At this point we should mention that for now on we will use Hartree units, where  $m_e$ ,  $e$ ,  $\hbar$  and  $\frac{1}{4\pi\epsilon_0}$  are equal to the unity.

The Hamiltonian will be given by the equation (2.5), which we will rewrite as:

$$\hat{h}_e = \sum_{i=1}^N \hat{h}_{1(i)} + \frac{1}{2} \sum_{i=1}^N \sum_{j \neq i} \hat{v}_{2(i,j)}, \quad (2.7)$$

where  $\hat{h}_{1(i)}$  contains the kinetic contribution plus the electron-nucleus and electron-external field contribution:

$$\hat{h}_{1(i)} = -\frac{1}{2} \nabla_{r_i}^2 + \hat{v}_{\text{ext}}(R, r_i) \quad (2.8)$$

and  $\hat{v}_{2(i,j)}$  describes the electron-electron Coulomb interaction:

$$\hat{v}_{2(i,j)} = \frac{1}{|r_i - r_j|}. \quad (2.9)$$

Doing this, we have two contributions to the total energy  $E_{\text{HSCF}}$ ,

$E^{(1)} = \langle \Phi | \sum_{i=1}^N \hat{h}_{1(i)} | \Phi \rangle$  and  $E^{(2)} = \langle \Phi | \frac{1}{2} \sum_{i=1}^N \sum_{j \neq i} \hat{v}_{2(i,j)} | \Phi \rangle$ . The first one can be written as:

$$E^{(1)} = \sum_{i=1}^N \int \Phi^*(r) \hat{h}_{1(i)} \Phi(r) dr. \quad (2.10)$$

Replacing the total electron wave function with the product of the individual one-electron orbitals, equation (2.6), and taking into account that the one electron orbitals are normalized to 1, we obtain:

$$E^{(1)} = \sum_{i=1}^N \int \dots \int \varphi_1^*(r_1) \dots \varphi_N^*(r_N) \hat{h}_{1(i)} \varphi_1(r_1) \dots \varphi_N(r_N) dr_1 \dots dr_N,$$

which can be rewritten as:

$$E^{(1)} = \sum_{i=1}^N E_{ii}, \quad (2.11)$$

where

$$E_{ii} = \int \varphi_i^*(r_i) \hat{h}_{1(i)} \varphi_i(r_i) dr_i. \quad (2.12)$$

The second contribution  $E^{(2)}$  can be treated in a similar way:

$$E^{(2)} = \frac{1}{2} \sum_{i=1}^N \sum_{i \neq j}^N J_{ij}, \quad (2.13)$$

where  $J_{ij}$  is:

$$J_{ij} = \int \frac{\rho_i(r_i) \rho_j(r_j)}{|r_i - r_j|} dr_i dr_j, \quad (2.14)$$

then we can write the HSCF energy as:

$$E_{HSCF} = \sum_{i=1}^N E_{ii} + \frac{1}{2} \sum_{i=1}^N \sum_{i \neq j}^N J_{ij}. \quad (2.15)$$

Now, since the first  $N$  one-electron orbitals construct the ground state of the system (state with lower energy), the variation of the system  $E_{HSCF}$  energy with respect to  $\varphi_i^*(r_i)$  is 0, in other words:  $\frac{\delta E_{HSCF}}{\delta \varphi_i^*(r_i)} = 0$ . Then, using Lagrange multipliers with the constrain  $\int |\varphi_i(r_i)|^2 dr_i - 1 = 0$ ,

we can write:

$$\frac{\delta}{\delta \varphi_i^*(r_i)} [E_{HSCF} - \sum_{i=1}^N \varepsilon_i (\int |\varphi_i(r_i)|^2 dr_i - 1)] = 0, \quad (2.16)$$

where  $\varepsilon_i$  are the Lagrange multipliers. Also it is important to say at this point that we will assume that the states  $\varphi_i(r_i)$  are not coupled to the  $\varphi_i^*(r_i)$ . The variation of the second term on the left hand side with respect to  $\varphi_i^*(r_i)$  is a straight forward procedure and can be written as:

$$\frac{\delta}{\delta\varphi_i^*(r_i)} \sum_{i=1}^N \varepsilon_i (\int |\varphi_i(r_i)|^2 dr_i - 1) = \varepsilon_i \varphi_i(r_i), \quad (2.17)$$

while the variation of  $E_{HSCF}$  will have 3 terms that according to equations (2.8), (2.12), (2.14) and (2.15) will be:

$$\frac{\delta}{\delta\varphi_i^*(r_i)} [\sum_{i=1}^N \int \varphi_i^*(r_i) v_{ext} \varphi_i(r_i) dr_i] = v_{ext} \varphi_i(r_i), \quad (2.18)$$

$$\frac{\delta}{\delta\varphi_i^*(r_i)} [\sum_{i=1}^N \int \varphi_i^*(r_i) \frac{-1}{2} \nabla_{r_i}^2 \varphi_i(r_i) dr_i] = \frac{-1}{2} \nabla_{r_i}^2 \varphi_i(r_i), \quad (2.19)$$

$$\frac{\delta}{\delta\varphi_i^*(r_i)} [\sum_{i=1}^N \sum_{i \neq j} \int \int \varphi_i^*(r_i) \varphi_i(r_i) v_{2(i,j)} \varphi_j^*(r_j) \varphi_j(r_j) dr_i dr_j] = \sum_{i \neq j} \int \frac{\varphi_j(r_j)}{|r_i - r_j|} dr_j \varphi_i(r_i). \quad (2.20)$$

Plugging this back into equation (2.16), we get the following one-particle Schrödinger equation:

$$[\frac{-1}{2} \nabla_{r_i}^2 + v_{ext} + \sum_{i \neq j} \int \frac{\varphi_j(r_j)}{|r_i - r_j|} dr_j] \varphi_i(r_i) = \varepsilon_i \varphi_i(r_i). \quad (2.21)$$

The second and third term on the left hand side of the equation can be combined into one effective potential. Then, the potential experienced by one electron will be comprised of the potential generated by the nucleus plus the electric potential generated by all the other electrons, as originally proposed by Hartree:

$$v_{eff}^{(H)} = v_{ext} + \sum_{i \neq j}^N \int \frac{\varphi_j(r_j)}{|r_i - r_j|} dr_j. \quad (2.22)$$

It is important to mention that in the HSCF formality, the sum of the Eigen values  $\varepsilon_i$  does not equal the total energy of the system under consideration. This can be easily seen by multiplying equation (2.21) by  $\varphi_i^*(r_i)$  and integrating over the whole space, which leads to:

$$\varepsilon_i = E_{ii} + \sum_{i \neq j}^N J_{ij},$$

leading immediately to:

$$E_{HSCF} = \sum_{i=1}^N \varepsilon_i - \frac{1}{2} \sum_{i=1}^N \sum_{i \neq j}^N J_{ij}. \quad (2.23)$$

Equation (2.21) represents a set of N coupled differential equations, where the potential depends on Eigen functions, see equation (2.22). This Schrödinger equation has to be solved iteratively starting with a trial wave function and again recalculating the effective potential until convergence is achieved.

The problem with Hartree approximation is that treats the electrons as distinguishable particles when in reality they are not. The problem lies in the construction of the wave function, equation (2.6), which does not follow the Pauli's principle. This leads to the Hartree-Fock approximation.

## 2.4 Hartree-Fock Approximation

In 1930 J. C. Slater[17] and V. A. Fock point out that the Hartree method could be improved by writing the wave function not as a product of the one-electron orbitals, but as a linear combination of such functions with permuted indices. In the work done by Fock [18, 19] the exchange effects are included, but his work was too abstract in order to be successfully implemented. In 1935 Hartree reformulates his original work based on Slater's and Fock's work, this is known as the Hartree-Fock approximation.

In the Hartree-Fock approximation the total wave function is constructed as the well-known Slater determinant of  $N$  one-electron orbital wave functions. Doing this, the Pauli's principle that requires an antisymmetric total wave function under the exchange of two electrons is satisfied. In order to show the general properties and features of this method we will use a two electron system, the generalization to  $N$  particles will be obvious. We will start by writing the total wave function as:

$$\Phi(x_1, x_2) = \frac{1}{\sqrt{2}}[\varphi_1(1)\varphi_2(2) - \varphi_1(2)\varphi_2(1)], \quad (2.24)$$

where the  $i$  in  $\varphi_i(j)$  refers to the  $i$ th one-electron orbital and the  $j$  to the spatial and spin coordinates of the electron  $j$  condensed in one variable  $x_j = (r_j, \sigma_j)$ .

The Hamiltonian will have the general form shown in equation (2.7) and again we will have two contributions to the energy that we will call  $E^{(1)}$  and  $E^{(2)}$ . We will start by writing  $E^{(1)}$ :

$$E^{(1)} = \int \int \Phi^*(x_1, x_2)[\hat{h}_{1(1)} + \hat{h}_{1(2)}] \Phi(x_1, x_2) dx_1 dx_2, \quad (2.25)$$

giving rise to 8 terms of the form:

$$E_{ijklm}^{(1)} = \frac{1}{2} \int \int \varphi_1^*(i) \varphi_2^*(j) \hat{h}_{1(k)} \varphi_1(l) \varphi_2(m) dx_1 dx_2,$$

where  $i \neq j$  and  $l \neq m$  (due to antisymmetric nature of the total wave function  $\Phi(x_1, x_2)$ ). Among this terms we have  $E_{12212}^{(1)} = E_{21121}^{(1)}$  and  $E_{21221}^{(1)} = E_{12112}^{(1)}$ , all the other terms vanish because they contain terms of the form  $\int \varphi_2^*(m) \varphi_1(m) dx_m$  which are equal to zero due the orthonormal nature of the one-electron orbital functions. On the other hand,

$$\begin{aligned} E_{12112}^{(1)} &= \frac{1}{2} \int \varphi_1^*(1) \hat{h}_{1(1)} \varphi_1(1) dx_1 \int \varphi_2^*(2) \varphi_2(2) dx_2 \\ &= \frac{1}{2} \int \varphi_1^*(1) \hat{h}_{1(1)} \varphi_1(1) dx_1 = \frac{1}{2} E_{11} \end{aligned} \quad (2.26)$$

and

$$E_{21121}^{(1)} = \frac{1}{2} \int \varphi_2^*(1) \hat{h}_{1(1)} \varphi_2(1) dx_1 = \frac{1}{2} E_{22}, \quad (2.27)$$

then we can write  $E^{(1)}$  as:

$$E^{(1)} = \frac{1}{2} \left( E_{12212}^{(1)} + E_{21121}^{(1)} + E_{21221}^{(1)} + E_{12112}^{(1)} \right) = E_{11} + E_{22}. \quad (2.28)$$

This can easily be generalized to an N electron system as:

$$E^{(1)} = \sum_{i=1}^N E_{ii}. \quad (2.29)$$

the energy  $E^{(2)}$  coming from the electron-electron interaction has four terms of the form:

$$E_{ijklmn}^{(2)} = \frac{1}{2} \int \int \varphi_1^*(i) \varphi_2^*(j) \hat{v}_{2(k,l)} \varphi_1(m) \varphi_2(n) dx_1 dx_2.$$

Again, the 1/2 factor comes from the normalization of the Slater determinant. Due to the nature of the  $\hat{v}_{2(k,l)}$  operator (see equation (2.9)) and the construction of the wave function through the Slater determinant, we have  $k \neq l$ ,  $i \neq j$  and  $m \neq n$ : This gives rise to two kind of terms, the first one when  $i=k=m$  and  $j=l=n$ , and the second one when  $i=k=n$  and  $j=l=m$ . The first kind are called Coulomb integrals and have exactly the same expression as the ones found in the Hartree approximation (see equation (2.14)):

$$J_{ij} = E_{ijij}^{(2)} = \frac{1}{2} \int \int \varphi_1^*(i) \varphi_2^*(j) \hat{v}_{2(i,j)} \varphi_1(i) \varphi_2(j) dx_1 dx_2. \quad (2.30)$$

The second kinds of terms are called exchange integrals and have the form:

$$K_{ij} = E_{ijji}^{(2)} = \frac{-1}{2} \int \int \varphi_1^*(i) \varphi_2^*(j) \hat{v}_{2(i,j)} \varphi_1(j) \varphi_2(i) dx_1 dx_2. \quad (2.31)$$

The similarity between these two equations is remarkable, the difference lies in the fact that in the last equation  $\varphi_1$  and  $\varphi_1^*$  are associated to different electrons. The  $K_{ij}$  contributions to the energy have no classical interpretation, it comes from the construction of the total wave function as a Slater determinant of the one-electron orbitals (implemented to satisfy Pauli's principle), the negative character of these terms comes, again, from the construction of the total wave function, but the physical interpretation is that the exchange interaction reduces the Coulomb interaction by pushing electrons away from each other resulting in a lack of electronic density.

Coming back to the energy  $E^{(2)}$ , we have 4 terms contributing to this energy, but due to symmetry of the  $\hat{v}_{2(i,j)}$  operator ( $\hat{v}_{2(i,j)} = \hat{v}_{2(j,i)}$ ), two of them are identical to the other two allowing us to write the  $E^{(2)}$  as:

$$E^{(2)} = \frac{1}{2} \left[ E_{121212}^{(2)} + E_{212121}^{(2)} - E_{121221}^{(2)} - E_{212112}^{(2)} \right] = J_{12} - K_{12}. \quad (2.32)$$

These results can easily be generalized to an N electron system as:

$$E^{(2)} = \frac{1}{2} \sum_{i=1}^N \sum_{j \neq i}^N (J_{ij} - K_{ij}), \quad (2.33)$$

allowing us to write the total energy of the system  $E_{HF}$  as:

$$E_{HF} = \sum_{i=1}^N E_{ii} + \frac{1}{2} \sum_{i=1}^N \sum_{j \neq i}^N (J_{ij} - K_{ij}), \quad (2.34)$$

where the 1/2 factor is included to avoid the doubled counting in the sum, also is important to notice that the term  $i=j$  could have been included in the sum because the self-interaction diagonal terms of  $J_{ii}$  exactly cancels with the corresponding  $K_{ii}$  terms.

In an analogous way as the one previously described in the Hartree approximation, minimization of  $E_{HF}$  respect to  $\varphi_1^*(i)$ , using Lagrange multipliers with the orthonormalization constrain, leads to the one electron Schrödinger equations:

$$\hat{h}_{1(1)}\varphi_i(x) + \sum_{j \neq i}^N \left[ \int \varphi_j^*(1) \hat{v}_{2(1,2)} \varphi_j(1) dx_1 \right] \varphi_i(x) - \sum_{j \neq i}^N \left[ \int \varphi_j^*(1) \hat{v}_{2(1,2)} \varphi_i(1) dx_1 \right] \varphi_j(x) = \varepsilon_i \varphi_i(x), \quad (2.35)$$

the first term correspond to the kinetic and the electron-nucleus interaction (see equation (2.8)), the second term is direct coulomb interaction  $\hat{J}_i$  (obtained also in the Hartree approximation) and finally we have the exchange term  $\hat{K}_j$ , which is not a diagonal operator in the sense that when applied to an orbital  $\varphi_i$  produces a different orbital  $\varphi_j$ . This is:

$$\hat{K}_j \varphi_i(x_2) = [\int \varphi_j^*(1) \hat{v}_{2(1,2)} \varphi_i(1) dx_1] \varphi_j(x_2). \quad (2.36)$$

It can be easily seen from equation (2.35) that:

$$\varepsilon_i = E_{ii} + \sum_{j \neq i}^N J_{ij} - K_{ij}, \quad (2.37)$$

allowing us to write  $E_{HF}$  as:

$$E_{HF} = \sum_{i=1}^N \varepsilon_i - \sum_{i=1}^N \sum_{j \neq i}^N J_{ij} - K_{ij}. \quad (2.38)$$

In the same way as in the Hartree formalism, equation (2.35) has to be solved iteratively starting from a trial wave function, until convergence is achieved.

The Hartree-Fock formalism accounts for most of the total energy, but fails to take into account for correlation effects. One of the efficient means to take into account this effect is the Density Functional Theory (DFT), This will be discussed in the following section.

## 2.5 Density Functional Theory

At the same time as Hartree developed his approximation previously described on 1927, L. H. Thomas and E. Fermi, independently, work and proposed what today is known as the Thomas-Fermi theory. The idea was to assume that the fundamental variable of the many body electronic problem was the charge density  $\rho(r)$ , where the energy of the system is a functional of the density.

Thomas-Fermi theory suffers of several problems and in general does not reproduce correctly the system's energy. It is worth mentioning because it sets up the basis of the DFT

which is very successful in attempting to solve the many bodies problem and improves the energy accuracy obtained in the Hartree and Hartree-Fock approximations.

The Density Functional Theory, as its name suggests, is a theory based on the functional of the charge density, the difference with the Hartree and Hartree-Fock approximations lies in the fact that in the latter two the electron orbitals are the base of the approximation and have physical meaning, while in the DFT the electrons orbitals have no physical meaning. The one-electron orbitals are used as an artificial mathematical tool to reproduce the charge density, which, as we mentioned earlier, is the base of this theory.

The density functional theory is based on the Hohenberg-Kohn theorem, which is, in fact, divided in two theorems [20]:

### 2.5.1 Hohenber– Kohn Theorem

**Hohenberg-Kohn theorem Part a:** "The external potential  $v_{ext}(r)$  is (to within a constant) a unequivocally determined by the electronic charge density"[ 21].

*Proof:* The proof is based on reduction to the absurdity and begins assuming that there are two potentials,  $v_{ext}(r)$  and  $v'_{ext}(r)$ , both giving rise to the same electronic density  $\rho(r)$ . The Hamiltonians will be given by  $\hat{H} = \hat{T} + \hat{V}_{ext} + \hat{U}_{e-e}$  and  $\hat{H}' = \hat{T} + \hat{V}'_{ext} + \hat{U}_{e-e}$  with ground state wave function and energy  $\Phi, \Phi'$ , and  $E_0 = \langle \Phi | \hat{H} | \Phi \rangle$ ,  $E'_0 = \langle \Phi' | \hat{H} | \Phi' \rangle$  respectively. Then, the variational principle tells us that:

$$E_0 \leq \langle \Phi' | \hat{H} | \Phi' \rangle \tag{2.39}$$

$$E_0 \leq \langle \Phi' | \widehat{H} + \widehat{H}' - \widehat{H}' | \Phi' \rangle \quad (2.40)$$

$$E_0 \leq \langle \Phi' | \widehat{H}' | \Phi' \rangle + \langle \Phi' | \widehat{H} - \widehat{H}' | \Phi' \rangle \quad (2.41)$$

$$E_0 \leq E'_0 + \langle \Phi' | \widehat{V}_{ext} - \widehat{V}'_{ext} | \Phi' \rangle \quad (2.42)$$

$$E_0 \leq E'_0 + \int \rho(r) [v_{ext}(r) - v'_{ext}(r)] dr. \quad (2.43)$$

In the same way interchanging the prime sign in equation (2.39) we get:

$$E'_0 \leq E_0 - \int \rho(r) [v_{ext}(r) - v'_{ext}(r)] dr, \quad (2.44)$$

adding this two equations (43 and 44) we found the clear contradiction  $0 < 0$ , which lead us to the conclusion that the external potential is univocally determined by the charge density. This concludes the proof.

On the other hand, the energy of the system is indeed a functional of  $\rho(r)$ :

$$E[\rho(r)] = T[\rho(r)] + U_{ee}[\rho(r)] + V_{ext}[\rho(r)],$$

where  $T[\rho(r)]$ ,  $U_{ee}[\rho(r)]$  and  $V_{ext}[\rho(r)]$  denotes the kinetic, electron-electron interaction and external potential contributions to the energy respectively. Then, doing  $F[\rho(r)] = T[\rho(r)] + U_{ee}[\rho(r)]$  and  $V_{ext}[\rho(r)] = \int \rho(r) v_{ext} dr$  we get:

$$E[\rho(r)] = F[\rho(r)] + \int \rho(r) v_{ext} dr, \quad (2.45)$$

which lead us to the second theorem:

**Hohenberg-Kohn theorem Part b:** The density  $\rho(r)$  that minimizes the total energy functional (equation (2.45)) is the ground state density, this is:

$$E_0 = E[\rho(r)] \leq E[\tilde{\rho}(r)]. \quad (2.46)$$

*Proof:* see reference [21 page 57]

### 2.5.2 Kohn–Sham Equations

In 1965 Kohn and Sham [22] found that a non-interacting system of electrons will be exactly described by an anti-symmetric wave function, such as the one given by the Slater determinant. Doing so the ground state density matrix is:

$$\rho(r) = \sum_{i=1}^N f_i \varphi_i(r) \varphi_i^*(r), \quad (2.47)$$

where  $\varphi_i(r)$  are the one electron orbitals and  $f_i$  are the corresponding occupation number. The Hamiltonian of such non-interacting reference system will be given by:

$$\hat{H} = \sum_{i=1}^N \left[ -\frac{1}{2} \nabla_i^2 + v_R(r_i) \right], \quad (2.48)$$

where  $N$  is the number of electrons and  $v_R$  is the potential of the non-interacting system called reference potential. The key point is that the reference potential  $v_R$  is such that will produce the same density  $\rho(r)$  of the real interacting system and then the Hohenberg-Kohn's theorem ensures that the ground state energy of the interacting and non-interacting systems coincides. As it was mentioned earlier, the ground state wave function of such non-interacting system of electrons will be given by the Slater determinant:

$$\Phi(r) = \frac{1}{\sqrt{N_S}} SD[\varphi_1(r_1)\varphi_2(r_2)\varphi_3(r_3) \dots \varphi_{N_S}(r_{N_S})], \quad (2.49)$$

with  $N_s=N/2$  (two electrons per level), the ground state charge density will be given by equation (2.47), with  $f_i=2$  for  $i \leq N/2$  and  $f_i=0$  for  $i \geq N/2$ , this is:

$$\rho(r) = 2 \sum_{i=1}^{N/2} |\varphi_i(r)|^2. \quad (2.50)$$

At this point it is important to say that one electron orbitals  $\varphi_i$  do not represent real electrons (this is just a mathematical tool used to reach our goal). The real physical meaning is the sum of the square norm of these quasi particles orbitals, see equation (2.50), which coincides with the ground state charge density of the real electron-electron interacting system.

These quasi particle orbitals, or Kohn-Sham orbitals, will be the first  $N_s$  solutions to the following eigenvalue problem:

$$\hat{H}_{K-S}\varphi_i = \varepsilon_i\varphi_i, \quad (2.51)$$

where  $\hat{H}_{K-S}$  is the one electron Hamiltonian:

$$\hat{H}_{K-S} = -\frac{1}{2}\nabla_i^2 + v_R(r_i). \quad (2.52)$$

Equation (2.51) and (2.50) are known as Kohn-Sham equations. Now we will focus on finding the reference potential, we will start by assuming that the kinetic energy of the full interacting system can be written as:

$$T_R[\rho] = -\frac{1}{2}\sum_{i=1}^{N_S} \langle \varphi_i | \nabla^2 | \varphi_i \rangle. \quad (2.53)$$

Now, the universal density functional  $F[\rho]$  is:

$$F[\rho] = T_R[\rho] + \frac{1}{2} \int \int \frac{\rho(r)\rho(r')}{|r-r'|} dr dr' + E_{xc}[\rho]. \quad (2.54)$$

Is important to note that all the information about the kinetic correlation ignored in  $T_R[\rho]$  is contained in  $E_{xc}[\rho]$ : Plugging  $F[\rho]$  into the energy functional  $E[\rho] = F[\rho] + \int \rho(r)v_{ext}(r) dr$ , we get:

$$E_{KS}[\rho] = T_R[\rho] + \int \rho(r)v_{ext}(r) dr + \frac{1}{2} \int \int \frac{\rho(r)\rho(r')}{|r-r'|} dr dr' + E_{xc}[\rho], \quad (2.55)$$

then using Lagrange multipliers and the constrain  $\int \rho(r) dr = N$  we obtain:

$$\frac{\delta}{\delta\rho(r)} (E_{KS}[\rho] - \mu(\int \rho(r) dr - N)) = 0 \quad (2.56)$$

$$\frac{\delta T_R[\rho]}{\delta\rho(r)} + v_{ext}(r) + \int \frac{\rho(r')}{|r-r'|} dr' + \frac{\delta E_{xc}[\rho]}{\delta\rho(r)} = \mu. \quad (2.57)$$

The energy functional of the non-interacting system  $E_R[\rho]$  is:

$$E_R[\rho] = T_R[\rho] + \int \rho(r)v_R(r) dr. \quad (2.58)$$

Using again the Lagrange multipliers and the restriction  $\int \rho(r) dr = N$ , we get:

$$\frac{\delta}{\delta\rho(r)} (E_R[\rho] - \mu_R(\int \rho(r) dr - N)) = 0 \quad (2.59)$$

$$\frac{\delta T_R[\rho]}{\delta\rho(r)} + v_R(r) = \mu_R. \quad (2.60)$$

Since the energy of the non-interacting system should be equal to the energy of the interacting one and the number of particles is the same in both systems, the chemical potentials

$\mu_R$  and  $\mu$ , see equations (2.57) and (2.60), are equal to each other. Then we are able to write the reference potential  $v_R$  as:

$$v_R(r) = v_{ext}(r) + \int \frac{\rho(r')}{|r-r'|} dr' + \frac{\delta E_{xc}[\rho]}{\delta \rho(r)}. \quad (2.61)$$

At this point it is important to note that the reference potential  $v_R$  is a function of the charge density  $\rho(r)$ , which is a function of the Kohn-Sham orbitals  $\varphi_i(r)$ . This means that equations (2.50), (2.51) and (2.61) have to be solved self consistently.

Now we are in the position to evaluate the energy of the interacting system, see equation (2.55), by writing the external potential in terms of the reference potential via equation (2.61) we have:

$$E_{KS}[\rho] = T_R[\rho] + \int \rho(r)v_R dr - \frac{1}{2} \int \int \frac{\rho(r)\rho(r')}{|r-r'|} dr dr' + E_{xc}[\rho] - \int \rho(r) \frac{\delta E_{xc}[\rho]}{\delta \rho(r)} dr \quad (2.62)$$

$$E_{KS}[\rho] = 2 \sum_{i=1}^N \varepsilon_i - \frac{1}{2} \int \int \frac{\rho(r)\rho(r')}{|r-r'|} dr dr' + E_{xc}[\rho] - \int \rho(r) \frac{\delta E_{xc}[\rho]}{\delta \rho(r)} dr. \quad (2.63)$$

A similar equation is obtained for spin polarized systems:

$$E_{KS}[\rho_\uparrow, \rho_\downarrow] = \sum_{s=1}^2 \sum_{i=1}^N \varepsilon_{i,s} - \frac{1}{2} \int \int \frac{\rho(r)\rho(r')}{|r-r'|} dr dr' + E_{xc}[\rho_\uparrow, \rho_\downarrow] - \int \rho(r) \frac{\delta E_{xc}[\rho_\uparrow, \rho_\downarrow]}{\delta \rho(r)} dr. \quad (2.64)$$

The first two terms are known, while the last two terms containing the exchange and correlation contributions  $E_{xc}$  are still unknown. We can split the term  $E_{xc}$  into an exchange and a correlation term as:

$$E_{xc} = E_x[\rho] + E_c[\rho]. \quad (2.65)$$

(We changed to the non-spin polarized case, since it has a simpler notation. Generalization to spin polarized case will be done when needed.)

The expression for the exchange term  $E_x[\rho]$  is provided by the Hartree-Fock method, see equation (2.31) which will be rewritten as:

$$E_x[\rho] = \sum_{i>j} K_{ij}, \quad (2.66)$$

where:

$$K_{ij} = \int \int \varphi_i^*(r_i) \varphi_j^*(r_j) \frac{1}{|r_i - r_j|} \varphi_i(r_j) \varphi_j(r_i) dr_i dr_j, \quad (2.67)$$

leaving, in principle,  $E_c[\rho]$  as the only unknown in the expression the system's energy  $E_{KS}[\rho]$ .

In 1927 and 1928 independently Thomas and Fermi proposed to express the kinetic, exchange and correlation contributions to the energy as:

$$E_\alpha[\rho(r)] = \int \rho(r) \epsilon_\alpha(\rho) dr, \quad (2.68)$$

where  $\epsilon_\alpha(\rho)$  is the energy density and  $\alpha$  stands for kinetic, exchange or correlation. In the case of uniform electron gas the expression for the exchange energy density can be simplified as:

$$\epsilon_\alpha^{hom} = -\frac{3}{4} \left(\frac{3}{\pi}\right)^{\frac{1}{3}} \rho^{\frac{1}{3}}(r)$$

$$\epsilon_\alpha^{hom} = -\frac{0.548}{r_s}, \quad (2.69)$$

where  $r_s = \sqrt[3]{\frac{3}{4\pi\rho}}$  is the mean inter-electronic distance expressed in atomic units. As can be seen, the denser the system (small distance between electrons), the higher the contribution of the exchange term. Unfortunately the determination of the correlation energy is a difficult many body problem, even for the homogenous gas, and there is not a simple expression for the correlation contribution to the energy.

In 1971 L. Hedin and B. I. Lundqvist proposed an expression for the correlation contribution  $\epsilon_c$  [23]:

$$\epsilon_c = -C\left[\left(1 + \left(\frac{r_s}{A}\right)^3\right) \ln\left(1 + \frac{A}{r_s}\right) + \frac{r_s}{2A} + \left(\frac{r_s}{A}\right)^2 - \frac{1}{3}\right], \quad (2.70)$$

where  $C$  and  $A$  are constants. Also, an Exact solution, in the very high and low charge density regime was proposed by Perdew and Zunger in (1981) [24]:

$$\epsilon_c^{PZ}[\rho] = \begin{cases} A\ln(r_s) + B + Cr_s \ln(r_s) + Dr_s, & r_s \leq 1 \\ \frac{\gamma}{1 + \beta_1\sqrt{r_s} + \beta_2 r_s}, & r_s > 1 \end{cases} \quad (2.71)$$

where  $A, B, C, D, \beta_1, \beta_2$  and  $\gamma$  are constants. As mentioned earlier the previous expressions for the exchange and correlation contribution to the energy are accurate for the homogenous electron gas ( $\rho$  does not depend on  $r$ ), the search for an expression for a real inhomogeneous gas will lead us the local density approximation (LDA) and gradient expansions.

### 2.5.3 Local Density Approximation

In the LDA formalism the inhomogeneous electron charge density is considered to be locally homogenous. The expression for the exchange and correlation energy density is given by:

$$\tilde{\epsilon}_{XC}^{LDA}[\rho(r)] = \frac{1}{2} \int \frac{\tilde{\rho}_{XC}^{LDA}(r,r')}{|r-r'|} dr', \quad (2.72)$$

where  $\tilde{\rho}_{XC}^{LDA}$  is the exchange and correlation hole (for the homogeneous electron gas) and is given by:

$$\tilde{\rho}_{XC}^{LDA} = \rho(r) \cdot [\tilde{g}^h(|r-r'|, \rho(r)) - 1], \quad (2.73)$$

where  $\tilde{g}^h(|r-r'|, \rho(r))$  is the pair correlation function for the homogeneous electron gas (It is local because depends only on the charge density at the point  $r$  and the distance between the point  $r$  and  $r'$ ) and of course the exchange and correlation energy will take the same form of equation (2.68):

$$E_{XC}^{LDA}[\rho(r)] = \int \rho(r) \tilde{\epsilon}_{XC}^{LDA}(\rho) dr. \quad (2.74)$$

In practice the LDA exchange and correlation contribution to energy  $E_{XC}^{LDA}[\rho(r)]$  is calculated by writing the exchange and correlation energy density as the sum of the exchange and correlation energy densities:

$$\tilde{\epsilon}_{XC}^{LDA}[\rho(r)] = \tilde{\epsilon}_X^{LDA}[\rho(r)] + \tilde{\epsilon}_C^{LDA}[\rho(r)], \quad (2.75)$$

where  $\tilde{\epsilon}_X^{LDA}[\rho(r)]$  is given by the exchange energy density of the homogeneous electron gas, see equation (2.69), and  $\tilde{\epsilon}_C^{LDA}[\rho(r)]$  as one of the approximations for the homogeneous electron gas previously discussed, see equation (2.70) or (2.71).

The LDA works well for system where the electronic density does not vary abruptly and somehow is uniform such as in metals.

At this point it is important to note that it may seem logical to use the exact expression for the exchange energy given by equation (2.66), while using the LDA for the correlation contribution to the energy to improve the LDA performance. In fact by doing so, the results obtained by LDA do not significantly improve. The reason behind this lies in the fact that the separation of the exchange and correlation energy into  $E_X$  and  $E_C$  is just a matter of practicality, both terms are connected and by taking  $E_X$  at a higher level of accuracy it cannot compensate for the errors made in  $E_C$ , also the exchange term described in equation (2.66) was obtained by constructing the total wave function as a Slater determinant (an arbitrary form).

In order to improve the results of the LDA and take into account the inhomogeneities in the charge density, an expansion in the charge density in terms of the gradient and higher order derivatives can be done. This is known as the gradient expansion.

#### 2.5.4 The Gradient Expansion

The exchange and correlation energy functional can be written as:

$$E_{XC}^{LDA}[\rho(r)] = \int \rho(r) \epsilon_{XC}[\rho(r)] F_{XC}[\rho(r), \nabla\rho(r), \nabla^2\rho(r) \dots] dr, \quad (2.76)$$

where an expansion to the fourth order of  $F_{XC}[\rho(r), \nabla\rho(r), \nabla^2\rho(r) \dots]$  takes the form:

$$F_{XC}[\rho(r), \nabla\rho(r), \nabla^2\rho(r) \dots] = 1 + \frac{10}{81} p + \frac{146}{2025} q^2 - \frac{73}{405} qp + Dp^2 + O(\nabla p^6), \quad (2.77)$$

$$\text{where } p = \frac{|\nabla\rho(r)|^2}{4(3\pi^2)^{\frac{2}{3}}\rho^{\frac{8}{3}}(r)} \text{ and } q = \frac{\nabla\rho^2(r)}{4(3\pi^2)^{\frac{2}{3}}\rho^{\frac{5}{3}}(r)}.$$

The first two coefficients of the expansion are exact, while the third one is an approximation and the fourth,  $D$ , is unknown. An expansion of the energy up to a second order is known to be a crude approximation valid only for densities that vary slowly. The expansion has several problems, for example is not monotonically convergent and has singularities that are only canceled when an infinite number of terms are taken into account.

To solve these problems, a functional that mimics the summation to infinite order, while verifying certain conditions such as long range decay is required. These have been called generalized gradient approximations (GGAs).

### 2.5.5 Generalized Gradient Approximation

Several GGAs have been proposed, among them we have the Langreth-Mehl functional, BLYP functional and the one proposed by Perdew, Burke and Ernzerhof (PBE) in 1996, which is one of the most widely used [25]. In the PBE approximation, the enhancement factor corresponding to the exchange contribution is written as:

$$F_X(s) = 1 + k - \frac{k}{1 + \frac{\mu s^2}{k}}, \quad (2.78)$$

where  $\mu=0.21951$ ;  $k=0.804$  and  $s = \frac{|\nabla\rho(r)|}{2k_F\rho}$ , while the correlation contribution to the energy is given by:

$$E_C^{GGA} = \int \rho(r) [\epsilon_C^{LDA}(\rho, \xi) + H(\rho, \xi, t)] dr, \quad (2.79)$$

where  $H(\rho, \xi, t)$  is a function of the charge density  $\rho$ , the magnetization  $\xi$ , while  $t$  is also function of  $\rho$  and  $\xi$  which can be found in the literature [21].

## 2.6 GW Approximation

In the previous sections we have discussed how to solve the many body electronic problem, it has been shown that all the contributions to the energy are known exactly except for the exchange and correlation terms. The exact form of the exchange contribution was described in the Hartree-Fock section, leaving the correlation contribution as the big unknown. As we have mentioned in the previous sections, extensive work towards the solution of this problem has been made, making the DFT theory a reliable tool to describe many body systems. On the other hand, a major problem is constituted by the fact that the DFT is based on the Hohenberg-Kohn theorem, which is only valid for the ground state, therefore the DFT fails to describe excited states and as a consequence usually underestimate the band gap of semiconductors. In 1965 Hedin [26] made a major contribution to the solution of this problem by showing how excited states can be described by approximating the self-energy contribution to the energy as a direct product of the green function and the screened Coulomb potential. In this section we will describe the basic ideas behind the GW approximation as were written by Hedin in 1965. We will start by writing the quasi particle Schrödinger equations as:

$$\left(\frac{-\hbar^2}{2m}\nabla^2 + v_{ext}(R, r_i) + v_H\right)\varphi_i(r_i) + \int \Sigma(r, r', E_i)\varphi_i(r')dr' = E_i\varphi_i(r_i), \quad (2.80)$$

where the  $v_H$  is the Hartree potential given by the third term in equation (2.21) and  $E_i$  denotes the quasi particle energy,  $\Sigma(r, r', E_i)$  is the self-energy term, which can be approximated as an expansion of the single particle Green functions  $G$  and the screened Coulomb interaction  $W$  as follows:

$$\begin{aligned} \Sigma(r, r', t) &= i\hbar G(r, r', t)W(r, r', t + \delta) - \\ &\hbar^2 \int \int G(r, r_3, t)G(r_3, r_4, t)G(r_4, r', t)W(r, r_4, t)W(r_3, r', t) dr_3 dr_4 + \dots \end{aligned} \quad (2.81)$$

In the GW approximation, as the name suggest, only the first term of the expansion is taken into account:

$$\Sigma(r, r', t) = i\hbar G(r, r', t)W(r, r', t + \delta). \quad (2.82)$$

In order to calculate the self-energy contribution to the quasi particle energy we should work in the frequency domain by doing a Fourier transformation of the self-energy:

$$\Sigma(r, r', t) = \frac{i\hbar}{2\pi} \int G(r, r', \omega + \omega') W(r, r', \omega') e^{i\omega' t} d\omega'. \quad (2.83)$$

Our task now is to find the green function and the screened Coulomb potential. In principle the Green function satisfies the following equation:

$$\left( \frac{-\hbar^2}{2m} \nabla^2 + v_{ext}(R, r_i) + v_H \right) G(r, r', E) + \int \Sigma(r, r', E) G(r'', r', E) dr'' = \delta(r - r'). \quad (2.84)$$

On the other hand, if the Green function for a simpler approximation (DFT) is known, then the true Green function can be calculated using the Dyson equation:

$$G(r, r', E) = G_0(r, r', E) + \iint G_0(r, r_1, E) \Delta \Sigma(r_1, r_2, E) G(r_2, r', E) dr_1 dr_2, \quad (2.85)$$

where  $\Delta \Sigma(r_1, r_2, E)$  is the perturbation given by  $\Delta \Sigma(r_1, r_2, E) = \Sigma(r_1, r_2, E) + v(r_1, r_2)$ , with  $v(r_1, r_2)$  the interaction potential of the reference system. Right hand side of equation (2.85) is a functional of  $G$ :  $G=F(G)$ , then equation (2.85) is a fixed point problem. Now,  $F(G)$  is a contraction ( $|F(G)-F(G')| < \alpha |G-G'|$ , whit  $\alpha < 1$ ), then the Banach' contraction theorem ensures a

unique solution for the equation (2.85) and by repeatedly replacing  $G$  on the right hand side of the equation by  $G_0 + G_0\Delta\Sigma(r_1, r_2, E)G$  (by itself) the following symbolic equation is obtained:

$$G(r, r', E) = G_0 + G_0\Delta\Sigma G_0 + G_0\Delta\Sigma G_0\Delta\Sigma G_0 + G_0\Delta\Sigma G_0\Delta\Sigma G_0\Delta\Sigma G_0 + \dots, \quad (2.86)$$

Which is known to converge rapidly,, which allow us to in the case of  $G_0W_0$  calculation, only the first term in the equation above is taken into account, which is well known for non-interacting electrons:

$$G_0(r, r', \omega) = \sum_{i=1}^N \frac{\varphi_i(r)\varphi_i^*(r')}{\omega - \varepsilon_i + i\eta(\varepsilon_i - \mu)}, \quad (2.87)$$

where  $\eta$  is a positive infinitesimal constant and  $\mu$  is the Fermi energy of the system.

On the other hand, the screened coulomb potential  $W(r, r', \omega)$  is given by:

$$W(r, r', \omega) = \int \varepsilon^{-1}(r, r'', \omega) v(r'', r') dr'', \quad (2.88)$$

or can be written in reciprocal space as:

$$W_{G, G'}(q, \omega) = \frac{4\pi e^2}{|q+G||q+G'|} \varepsilon_{G, G'}^{-1}(q, \omega), \quad (2.89)$$

with  $v(r, r') = 1/|r-r'|$  and the inverse of the dielectric function  $\varepsilon$  calculated in the random phase approximation:

$$\varepsilon(r, r'', \omega) = \delta(r - r'') - \int v(r, r''') \chi_0(r''', r', \omega) dr''', \quad (2.90)$$

which can also be written in the reciprocal space as:

$$\varepsilon_{G, G''}(q, \omega) = \delta_{G, G''} - \frac{4\pi e^2}{|q+G||q+G''|} \chi_{0G, G'}(q, \omega), \quad (2.91)$$

while the response function  $\chi_{0G,G'}$  is given by:

$$\chi_{0G,G'}(q, \omega) = \frac{1}{\Omega} \sum_{n,n',k} 2\omega_k (f_{n',k+q} - f_{n,k}).$$

$$\frac{\langle \varphi_{n',k+q} | e^{i(q+G)r} | \varphi_{n,k} \rangle \langle \varphi_{n,k} | e^{-i(q+G')r'} | \varphi_{n',k+q} \rangle}{\varepsilon_{n',k+q} - \varepsilon_{n,k} - \omega - i\eta}. \quad (2.92)$$

As mentioned earlier, in the case of the  $G_0W_0$  approximation the response function and the Green function are calculated using the quasi particles orbitals obtained by DFT.

## CHAPTER 3: FIRST PRINCIPLE STUDIES ON CATALYTIC SYSTEMS TOWARDS THE OXYGEN REDUCTION REACTION

### 3.1 Introduction

As described in Chapter 1, the search for new cost-effective and highly active electrocatalysts for the oxygen reduction reaction (ORR) is of great importance. The most efficient way to search is the rational tuning of the catalytic properties of the material by modification of the surface composition and/or morphology. Such rational search requires, however, understanding of the relationship among the surface composition, electronic structure, reactivity and activity toward ORR. One of the goals of the present work is to reveal important details of this relationship. To approach this challenging task, first, it is described what is known about this reaction.

The ORR is a complex multi-step reaction that may include many steps. As summarized by Adzic [27], two main pathways are possible: a) direct four electron reduction to H<sub>2</sub>O (in acid media):



b) peroxide pathway:



followed by



The second step in the pathway (b) has a very high reversible potential that significantly reduce the efficiency of the ORR.

The ORR has been extensively studied on Pt surfaces. It has been suggested that the 4-electron pathway is predominant for Pt. The DFT based calculations show that the activation energy barriers for O<sub>2</sub> dissociation on flat Pt surfaces are high and therefore the molecular adsorption is thus preferred [28]. In this case ORR may proceed through the following steps:



in this notation, “\*” denotes the adsorption site at the cathode surface. If oxygen is dissociated upon adsorption, the ORR pathway takes the path of equation (3.7) and (3.8) only.

The ORR highly depends on the adsorption energies of O, OH and OOH intermediates, The authors in [29] and [30] have constructed (O and OH adsorption energies) hyper-volcano diagrams for several metallic surfaces, showing that in order to obtain an optimal catalytic material the O and OH adsorption energies have to be reduced in the case of Pd and Ru and increased in the case of Ag. On the other hand, it has been shown a linear relation between the O and OH adsorption energies, as well as between O and OOH adsorption energies [31], suggesting

that the O adsorption energy is a good descriptor of the catalytic activity towards the ORR [32,33].

In this work, the binding energy, also called adsorption energy, characterizing the bonding of an atom or intermediate (X) with the surface under consideration was calculated as follows:

$$E_B(X) = E(\text{slab}) + E(X) - E(X/\text{slab}), \quad (3.9)$$

where  $E$  denotes the calculated total DFT energy per supercell,  $E(\text{slab})$  denotes the DFT energy of the clean surface under consideration,  $E(X)$  is the DFT energy of the insolated atom or intermediate and  $E(X/\text{slab})$  denotes the DFT energy of the atom or intermediate X adsorbed on the surface. Since the total energies of stable systems are negative,  $E_B(X)$  is positive if adsorption of a specie on the slab is favorable.

The valence charge density redistribution upon addition of an atom or intermediate (X) to the system will be used to explain the mechanisms controlling the bonding of the atom or intermediate (X) to the surface. It was defined as:

$$\delta\rho_{add} = \rho_{X/system}(r) - \rho_{system}(r) - \rho_X(r), \quad (3.10)$$

where  $\rho_{X/system}(r)$  is the valence charge density of system under consideration with the adsorbed atom or specie (X),  $\rho_{system}(r)$  is the valence charge density of the pristine system (with no atom or spice adsorbed) and finally  $\rho_X(r)$  describes the valence charge density of the insolated added atom or specie (X) at the position in the system under consideration.

In order to describe the energies of the reaction depicted in equations (3.4) through (3.8) we used the technique proposed by Nørskov and co-authors [29], where they set the reference potential as  $\mu(H^+ + e^-) = \frac{1}{2}\mu(H_2)$ . Within this approach, the reaction free energy  $\Delta G$  is calculated for each reaction step, which is defined as the difference between free energies of the initial and final states of the step. In general, it includes six terms:

$$\Delta G = \Delta E + \Delta ZPE - T\Delta S + \Delta G_U + \Delta G_{field} + \Delta G_{pH}. \quad (3.11)$$

Here  $\Delta E$  is the reaction energies obtained from DFT total energies of the catalyst surface with possible configurations of adsorbed reactants or intermediates. The DFT-based calculations of vibrational frequencies of adsorbates are used to define zero point energy corrections  $\Delta ZPE$ . Entropic contribution  $T\Delta S$  is approximated by the gas phase reaction entropy of reactants or intermediates taken from a NIST database [34] (translational contributions are subtracted for adsorbed species). If a reaction step involves the electron and proton transfer, the relevant bias effects are taken into account by shifting the energy by doing  $\Delta G_U = -eU$ , where  $U$  is the electrode potential and  $e$  is a transferred charge. The term  $\Delta G_{field}$  is a contribution of interaction of an adsorbate with the local electric field in the electric double layer formed in the vicinity of the cathode [35]. Finally, for non-zero pH the concentrational entropy correction is added:  $\Delta G_{pH}(pH) = kT \cdot \ln(10) \cdot pH$ . Since the ORR proceeds in acidic media ( $pH \approx 0$ ), in this work this term will be neglected. As  $\Delta G$  is calculated for each step of electro-catalytic reaction, a diagram of the free energies of these configurations is built as a function of the electrode potential.

Within this model, the onset potential  $U_0$  is defined as the potential difference between the two electrodes of the fuel cell at zero current. It can be estimated as the maximum value of  $U$

at which the reaction is still exothermic. The onset potential will be ruled by the lowest energy step (in equation (3.11) of the ORR reaction depicted in equation (3.4) through equation (3.8). Two scenarios are possible: a) for low reactive systems (systems with lower reactivity than the optimal one), the onset potential will be ruled by the adsorption of OOH (see equation (3.5)),  $U_0 = \Delta G(O_2) - \Delta G(OOH)$  and b) for highly reactive systems (systems with higher reactivity than the optimal one), the onset potential will be ruled by the OH adsorption, if  $\Delta G(O) > 2\Delta G(OH)$  then  $U_0 = \Delta G(OH)$ , otherwise  $U_0 = \Delta G(O) - \Delta G(OH)$ . Here  $\Delta G(O)$ ,  $\Delta G(OH)$  and  $\Delta G(OOH)$  denote the free energies of the  $H_2 + O^*$ ,  $1/2 \cdot H_2 + OH^*$  and  $1/2 \cdot H_2 + OOH^*$  states respectively, counted from the free energy of the final state ( $H_2O + *$ ).

Among the terms contributing to the free energy described in equation (3.11), the most important is the first one (As we mention above  $\Delta G_{pH}$  will be neglected, while  $\Delta G_{field}$  is also negligible due to the small effect of the electric field on the binding energy of O, OH and OOH[35]). It has been shown in [29] that the onset potential  $U_o$  is determined by the reaction in equation (3.7) and (3.8) for highly reactive systems, while for low reactive systems the onset potential is determined by the reaction in equations (3.4) and (3.5). The changes in free energies of the  $O^* + 2(H^+ + e^-)$ ,  $HO^* + (H^+ + e^-)$  and  $OOH^* + 3(H^+ + e^-)$  states are thus the key characteristics of electro-catalysts for both molecular and dissociative adsorption of  $O_2$ . Taking as a reference the free energy of the final state of the reaction ( $H_2O$  in gas phase), one can express  $\Delta E$  in equation (3.11) through binding energies of the intermediates and total energies of molecules in gas phase. For the states described by equations (3.6), (3.7) and (3.8), it makes:

$$\Delta E(O) = E_{tot}(H_2) + E_{tot}(O) - E_{tot}(H_2O) - E_B(O^*) \quad (3.12)$$

$$\Delta E(OH) = \frac{1}{2}E_{tot}(H_2) + E_{tot}(OH) - E_{tot}(H_2O) - E_B(OH^*) \quad (3.13)$$

$$\Delta E(OOH) = \frac{3}{2}E_{tot}(H_2) + E_{tot}(OOH) - 2E_{tot}(H_2O) - E_B(OOH^*). \quad (3.14)$$

The first three terms in equation (3.12), (3.13) and (3.14) are gas phase constant which do not depends on the catalytic system under consideration. The entropy contribution to the free energy  $\Delta G$  in equation (3.11) and the zero point energy depends on the vibration frequencies of the molecules and do not strongly change upon adsorption. Therefore, in a good approximation the free energy diagram is determined by the binding energy of O, OH and OOH.

### 3.2 Pd-Co Alloy Surfaces

In this work we focus on the  $Pd_{1-x}Co_x$  system. These alloys has been studied experimentally and exhibit activity toward ORR comparable to Pt[36, 37], they are also highly tolerant to the presence of methanol [38, 39], which is important for use in DMFC, and they are much less expensive that the Pt-based catalysts. The best electro-catalytic performance of these alloys has been observed for the Co concentration  $x = 0.2$  to  $0.33$  [37, 38]. For such concentration range, the alloys maintains the fcc structure. At elevated temperature they undergo surface segregation, which lead to formation the Pd monolayer (skin) on the alloy surface [39]. However, as suggested and confirmed in the present work, this segregation is a desirable effect, which leads to the enhancement of the ORR rate.

According to Ruban et al. in ref[40] a Pd segregation towards the surface in Pd-Co and Pd-Fe system is expected due to the large difference in surface segregation energies between Pd

and Co/Fe. Concerning Pd-Co systems, Wei et al. in ref[55] have prepared Pd-Co alloys at various pH values and characterized its catalytic activity towards the ORR. The XRD patterns showed that the Pd-Co alloys maintain the FCC structure of Pd for all the pH at which the samples were prepared. However, for the sample prepared at pH 13, the XRD pattern suggests that the sample preparation at high pH values leads to the incomplete formation of Pd-Co alloys. Furthermore the authors were able to determine that the Pd-Co alloys with a Pd rich surface have a higher catalytic activity than the Pd-Co alloys whose surface was comprised of a large amount of Co oxide. Similar results were found by Shao and coworkers in ref[39], where they performed XRD measurements on Pd-Co alloys, the authors were able to determine that the Pd and Co atoms were mixed completely forming a FCC structure. Furthermore, their results indicate that the Pd atoms are segregated towards the surface during annealing at high temperatures.

In previous work, Lamos and Balbuena used a simple three layer slab made up with Pd, Pd<sub>0.5</sub>Co<sub>0.5</sub>, and Pd<sub>0.75</sub>Co<sub>0.25</sub> layers to model the segregated Pd<sub>0.75</sub>Co<sub>0.25</sub> (111) surface [41]. The authors have calculated the adsorption energies of intermediates and built the free energy reaction diagrams for two possible reaction pathways using the Nørskov and co-worker model [29]. In this work they attempt to describe the mechanisms controlling the catalytic activity of Pd-Co alloys, However, several questions still have to be answered. For example, in [42] the authors argue that the contraction of the Pd-Pd bonds upon alloying is responsible for the enhancement in the catalytic activity of the system, more precisely, the authors argue an enhancement in the catalytic activity due to a change of only 0.05 eV in the adsorption energy of O. We believe this change is too small in order to produce the enhancement in the catalytic activity reported in the experiment. Pd atoms in the overlayer make bonds with Co atoms located

in the second layer, Cobalt has quite delocalized d-states, which should result in a strong hybridization with the d-states of Pd. The spin-polarized local densities of electronic states (LDOS) should form a wide d-band overlapping with the dPd-states. One can thus expect a significant modification of the Pd d-band upon the dCo–dPd hybridization which, in turn, will change the adsorption energies. This important effect has not been studied yet for this system.

The studies carried out on ref[41] considered an adsorbate coverage of 0.25 monolayer (ML). For other systems [29, 43, 44], it has been shown that there is a strong dependence of the reaction energetics with the intermediates and water coverage. To the extent of our knowledge, this effect has not been studied in Pd-Co alloys.

In the present work, we address the issues raised above. We report the results of accurate systematic computational studies of various factors which may control the ORR rate, including effects of co-adsorbed intermediates and water on the ORR energetics. We compare and contrast the results obtained for Pd–Co alloys with varying Co concentration  $x = 0, 0.25, \text{ and } 0.5$ , as well as the  $\text{Pd}_{0.75}\text{Co}_{0.25}(111)$  alloy covered with one monolayer of Pd (Pd/Pd<sub>0.75</sub>Co<sub>0.25</sub>). The reaction energetics are traced to the electronic structure of the alloy surfaces in order to reveal the main factors controlling the ORR in the system.

### **3.2.1 Computational Details**

The experimentally observed Pd-Co electro-catalysts systems are found to be in form of 4 nm to 11 nm nanoparticles [37,45]. Particles of such size range have large flat facets developed at their surfaces. We thus use the flat surface approximation to describe the catalytic properties of this system. Since the materials under consideration have the fcc structure, we calculate the

ORR characteristics on Pd-Co(111) surface. This surface is known to be the most stable one and the (111) facets are expected to dominate the surface.

For all system under consideration, the electronic structure, energetics and equilibrium atomic configurations are obtained using the VASP5.2 code [46] with projector augmented wave potentials [47] and the Perdew-Burke-Ernzerhof (PBE) version of the generalized gradient approximation (GGA) for the exchange and correlation functional [48]. All systems, except for clean Pd, were calculated taking into account spin polarization. In order to maintain periodicity we use supercells with a 5 layer Pd-Co slab and vacuum layer of 15 Å. For all calculations, the supercells had the (2x2) in-plane periodicity (see Figure 1). The (7x7x1) k-point samplings in Brillouin zone used in this work provide sufficient accuracy for the characteristics obtained by integration in the reciprocal space. The cut of energy of 400 eV was used for the plane wave expansion of wave functions and the 600 eV cut of energy was used for the charge density. To achieve structural relaxation, a self-consistent electronic structure calculation was followed by calculation of the forces acting on each atom. Based on this information the atomic positions were optimized to obtain equilibrium geometric structures in which forces acting on atoms do not exceed 0.02 eV/Å.

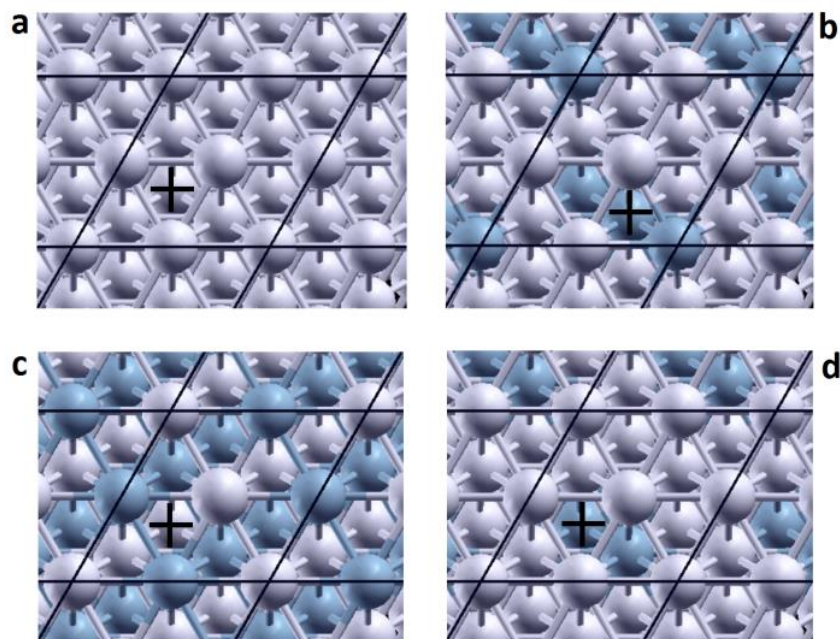


**Figure 1: Top view of the surfaces: panel a: Pd(111), panel b: Pd<sub>0.75</sub>Co<sub>0.25</sub>, panel c: Pd<sub>0.5</sub>Co<sub>0.5</sub> and panel d: Pd/Pd<sub>0.75</sub>Co<sub>0.25</sub>. Light grey and dark blue balls represent the Pd and Co atoms, respectively. Black straight lines separate supercells. Black crosses mark the preferred adsorption sites for atomic oxygen.**

To obtain  $\Delta ZPE$  used in equation (3.11), we have calculated the vibrational frequencies of the adsorbed O and OH using the finite-difference method. Since the masses of the ORR intermediates are much smaller than those of the substrate only the adsorbate modes were taken into account, while the slab atoms were considered frozen. Five displacements were used for each direction with the step of 0.015 Å. The zero point energies obtained from the vibrational frequencies were used to calculate the  $\Delta ZPE$  contributions to the reaction free energies. Entropic contributions to the reaction free energies were calculated as described in the introduction to this chapter.

The geometric structures of clean and adsorbed surfaces shown in this section have been plotted using the Xcrysden software [49].

### 3.2.2 Results on O and OH Adsorption With 0.25% Mono Layer Coverage

As mentioned earlier, four different systems were taken under consideration to model the Pd and Pd-Co alloys, these are: Pd(111), Pd<sub>0.75</sub>Co<sub>0.25</sub>(111), Pd<sub>0.5</sub>Co<sub>0.5</sub>(111) and Pd/Pd<sub>0.75</sub>Co<sub>0.25</sub>(111). First, a geometry optimization of the system was performed, followed by the calculation of the binding energies of the intermediates (O, OH and H<sub>2</sub>O) via equation (3.9).

For all systems under consideration, the binding energies were calculated for the atomic O adsorbed on all non-equivalent symmetric sites for the supercells with (2x2) in-plane periodicity. We have found that for all surfaces the hollow sites are preferred for O adsorption (these sites are marked with crosses in Figure 1). The  $E_B(O)$  values for the preferred adsorption sites are listed in the first four rows of Table 1. As it can be seen from Figure 1, for the non-segregated alloys, oxygen prefers to make bonds with the surface Co atoms. In the case of Pd<sub>0.75</sub>Co<sub>0.25</sub>, it makes one O–Co and two O–Pd bonds with  $E_B(O)$  larger than that for pure Pd. In the case of Pd<sub>0.5</sub>Co<sub>0.5</sub>, there are two O–Co and one O–Pd bonds, which results in further strengthening of oxygen bonding to the surface. It is important to note that the oxygen – surface bonding is found to be weaker for Pd/Pd<sub>0.75</sub>Co<sub>0.25</sub> than for pure Pd. This result supports the assumption [29, 30] that an optimal catalyst for ORR has to have lower  $E_B(O)$  than that for Pd. On the other hand, the stronger oxygen – surface bonding found for the non-segregated alloys, suggests that these materials will not catalyze ORR efficiently. We thus exclude them from further consideration.

**Table 1: Binding energies and zero point vibration energies calculated for O and OH adsorbed with 0.25 ML coverage on the preferred sites of the (111) surfaces of Pd and Pd-Co alloys.**

Adsorbate	Slab	$E_B$ (eV)	ZPE (eV)
O	Pd	4.568	0.0695
	Pd <sub>0.75</sub> Co <sub>0.25</sub>	4.930	0.0626
	Pd <sub>0.50</sub> Co <sub>0.50</sub>	5.620	0.0634
	Pd/ Pd <sub>0.75</sub> Co <sub>0.25</sub>	4.414	0.0690
OH	Pd	2.508	0.3309
	Pd <sub>0.75</sub> Co <sub>0.25</sub>	3.032	0.3318
	Pd <sub>0.50</sub> Co <sub>0.50</sub>	3.464	0.3418
	Pd/ Pd <sub>0.75</sub> Co <sub>0.25</sub>	2.522	0.3310

Since, in the course of ORR, hydroxyl may be formed upon “landing” of a proton and electron on the adsorbed oxygen,  $E_B(OH)$  were calculated for the preferred adsorption sites obtained for atomic O. These results are shown in the last four rows of Table 1. Note that changes in  $E_B(O)$  and  $E_B(OH)$  upon varying of the catalyst composition have the same trend, with a slight deviation from a linear relation.

### 3.2.3 Results on Co-Adsorption of the ORR Intermediates and Water

Although it is not easy to measure the coverage of the ORR intermediates in real reaction environment and it depends on electrode potential and varies from one material to other, there are indications [43, 50,51] that, in general at the fuel cell operation conditions, the coverage is higher than the 0.25 ML considered above. Furthermore, in the course of the reaction, the intermediates occur to be co-adsorbed with each other or with H<sub>2</sub>O at the neighboring surface sites. To study the effect of such co-adsorption we have calculated  $E_B(O)$ ,  $E_B(OH)$ , and  $E_B(H_2O)$  for the 0.5 ML coverage of each specie, as well as for the O–OH, O–H<sub>2</sub>O, and OH–H<sub>2</sub>O co-adsorption using the (2x2) supercell. These calculations were performed for Pd and

Pd/Pd<sub>0.75</sub>Co<sub>0.25</sub>. In initial configurations, O and OH were placed at neighboring hollow sites, which are found to be most stable for the 0.25 ML coverage, while water molecule was placed at a top site. To avoid an artificial force cancelation at symmetric sites, position and orientation of the adsorbates were slightly disturbed.

**Table 2: Binding energies of O and OH calculated for the co-adsorption configurations.**

Slab	Co-adsorbate	$E_B(\text{O})$ , eV	$E_B(\text{OH})$ , eV
Pd	O	3.989	2.004
	OH	4.038	2.793
	H <sub>2</sub> O	4.791	2.909
Pd/Pd <sub>0.75</sub> Co <sub>0.25</sub>	O	3.730	2.068
	OH	4.038	2.718
	H <sub>2</sub> O	4.487	2.855

The relaxed configurations obtained for Pd/Pd<sub>0.75</sub>Co<sub>0.25</sub> are shown in Figure 2 and Figure 3, while the calculated binding energy values are listed in the Table 2. As we can see from Figure 2, O atoms adsorbed with 0.5 ML coverage keeps staying at hollow sites reflecting symmetry of the system. Due to electronic charge transfer from the metal surface, oxygen atoms become negatively charged and thus repel each other. This repulsion causes an increase in the total energy of the system, which leads to a significant decrease in the binding energy. Indeed, the increase in the O coverage from 0.25 ML to 0.5 ML causes the decrease in  $E_B(\text{O})$  by 0.579 eV and 0.684 eV for Pd and Pd/Pd<sub>0.75</sub>Co<sub>0.25</sub>, respectively (see Tables 1 and 2).

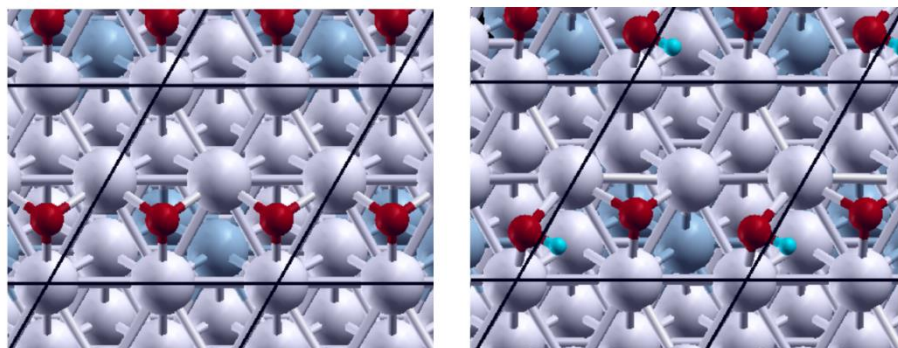


**Figure 2: The lowest energy configurations for the 0.5 ML hydroxyl adsorption (left panel) and OH–H<sub>2</sub>O co-adsorption (right panel).**

For the O–OH co-adsorption, we found that OH moves upon relaxation from the fcc hollow site to a bridge and tilts towards O adsorbed at the next fcc hollow site. This behavior may be explained as a result of attraction between positively charged H and negatively charged O (hydrogen bonds). This reordering reduces the total energy of the system. However, the overall effect is a significant weakening of both OH and O bonding to both Pd and Pd/Pd<sub>0.75</sub>Co<sub>0.25</sub> caused by O–OH repulsion.

We find the hydroxyl adsorbed with 0.5 ML coverage to have two stable configurations. The first one is achieved if in an initial configuration two OH are placed in two neighboring fcc hollow sites and tilted by a few degrees (to avoid artificial force cancelation). In this case (in the course of relaxation) both molecules keep staying at these hollow sites and take positions normal to the surface. However, it appears to be a local minimum with  $E_B(OH)$  equal to 1.812 eV and 1.962 eV for Pd and Pd/Pd<sub>0.75</sub>Co<sub>0.25</sub>, respectively. Indeed, if we initially tilt OH by  $\sim 30^\circ$  and move by 0.03 Å from the symmetric position (which is achievable within the frustrated rotation vibrational mode), the adsorbates undergo restructuring upon relaxation which results in the configuration shown in the left panel of Figure 3. This configuration is found to be much more

stable than the symmetric one. As a result we can conclude that upon increase in hydroxyl coverage from 0.25 ML to 0.5 ML the OH bonding to metal surface strengthens with an increase in  $E_B(OH)$  of 0.185 eV and 0.196 eV for Pd and Pd/Pd<sub>0.75</sub>Co<sub>0.25</sub>, respectively. The hydrogen bonds made between the adsorbed species for the arrangement of OH shown in the figure, lead to the decrease in the total energy of this system and hence to the increase in  $E_B(OH)$ .

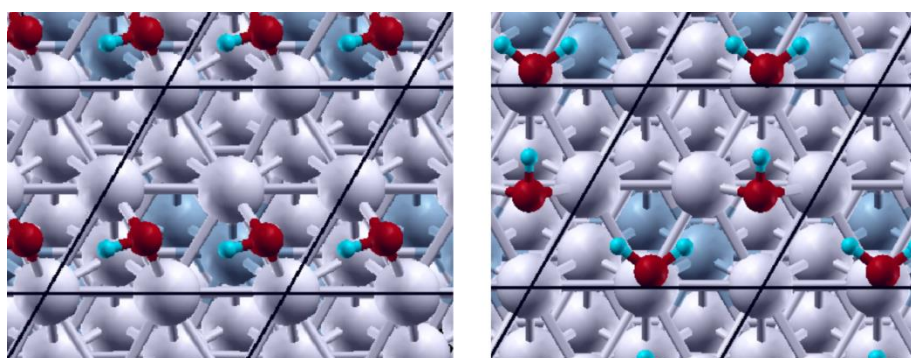


**Figure 3:** The lowest energy configurations for the 0.5 ML hydroxyl adsorption (left panel) and OH – H<sub>2</sub>O co-adsorption (right panel).

Co-adsorption with water also affects energetics and geometrical structure of the ORR intermediates. we find that in the O–H<sub>2</sub>O co-adsorbed structure, the O atoms stay at the initial hollow site, while H<sub>2</sub>O slightly shifts from the center of the top site and tilts to make hydrogen bonds with O. As a result, the co-adsorption causes increase in  $E_B(O)$  by 0.223 eV and 0.073 eV for Pd and Pd/Pd<sub>0.75</sub>Co<sub>0.25</sub>, respectively.

The co-adsorption of hydroxyl with water also strengthens the OH bonds to the catalyst surface:  $E_B(OH)$  increases upon the co-adsorption by 0.301 eV and 0.333 eV for Pd and Pd/Pd<sub>0.75</sub>Co<sub>0.25</sub>, respectively. Note that similar effect has been reported for other metal surfaces [29, 52]. As seen from Figure 3 panel **b**, in the OH–H<sub>2</sub>O structure, OH is shifted significantly

from the hollow toward the bridge sites and tilted to make hydrogen bonds with H<sub>2</sub>O, which stabilize the system. The water molecules are also found to be stabilized on the surfaces upon O and OH co-adsorption. For example, as compared to 0.25 ML H<sub>2</sub>O adsorption, binding energy of water to Pd(111) is increased from 0.299 eV to 0.448 eV and to 0.585 eV upon O and OH co-adsorption, respectively.

### 3.2.4 Reaction Free Energy Diagrams

The calculated adsorption energies, as well as the zero point energies (shown in Table 1) and the entropic contributions were used to build the reaction free energy diagrams. We focus on the reaction steps described by equations (3.7) and (3.8). Since the systems under consideration are highly reactive towards the O adsorption, we thus include the following states in the diagrams:  $\frac{1}{2}O_2+H_2$  gas phase,  $O^*+H_2$ ,  $*OH+\frac{1}{2}H_2$ , and  $H_2O+*$ . These states are likely to be the rate limiting for ORR [29]. The diagrams were constructed for Pd and Pd/Pd<sub>0.75</sub>Co<sub>0.25</sub> with the 0.25 ML and 0.5 ML coverage of adsorbates, as well as for configurations with O–OH, O–H<sub>2</sub>O, and OH–H<sub>2</sub>O co-adsorption. Figure 4 and Figure 5 show the diagrams built for  $U=0$  (the last term contributing to the energy in equation (3.11),  $\Delta G_{pH}$ , is neglected)

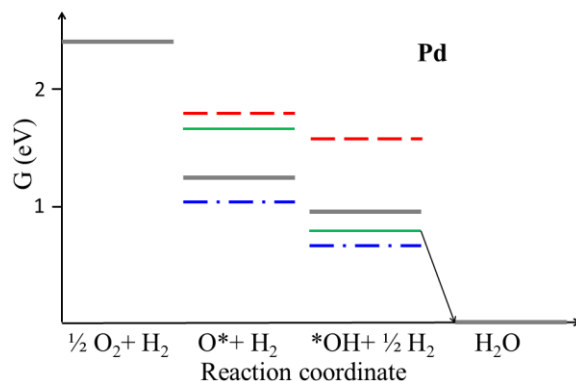


**Figure 4: Reaction free energy diagram built for Pd for the following intermediate adsorption configurations: 0.25 ML coverage of the adsorbates (thick solid lines), O – OH and OH – OH co-adsorption (thin solid lines), O – O and O – OH co-adsorption (dash lines), and O – H<sub>2</sub>O and OH – H<sub>2</sub>O co-adsorption (dash-dot lines). The arrowed line shows the  $U_0$  determining reaction step.**

Since 0.25 ML coverage of the ORR intermediates is used in many calculations [4, 5, 41, 42, 53] to characterize electro-catalytic activity of metal or alloy surfaces, we first built the reaction free energy diagrams for this coverage. As seen from Figure 4 and Figure 5, for both Pd and Pd/Pd<sub>0.75</sub>Co<sub>0.25</sub>,  $\Delta G(O) - \Delta G(OH)$  is much smaller than  $\Delta G(OH)$ . Therefore, within the model that we use, the onset potential is determined by the  $O^* + H^+ + e^- \rightarrow HO^*$  reaction step and its value can be estimated as  $U_0 = \Delta G(O) - \Delta G(OH)$ . This estimate results in  $U_0$  equal to 0.30 V and 0.37 V for Pd and Pd/Pd<sub>0.75</sub>Co<sub>0.25</sub>, respectively, which are much smaller than the experimental values. It is important to note that this model operates with the thermodynamic quantities and does not take into account kinetic barriers. Therefore, it is expected to overestimate the  $U_0$  values. The fact that our calculations result in  $U_0$  smaller than in experiment suggests that the modeling of the ORR with the 0.25 ML coverage of intermediates considered above is not realistic. There are some indications that the solvent effects can only slightly change the energetics of these reaction steps [54]. Therefore we focus here on the coverage and co-adsorption effects. As shown in Figure 4 and Figure 5, the ORR energetics changes dramatically

upon co-adsorption and variation of coverage of the intermediates. The co-adsorption with oxygen causes a significant increase in both  $\Delta G(O)$  and  $\Delta G(OH)$ . However, the  $\Delta G(O) - \Delta G(OH)$  difference does not change appreciable and hence  $U_0$  remain small. Water co-adsorption slightly improves the reaction energetics. Since it stabilizes the OH adsorption more than the O one, the  $\Delta G(O) - \Delta G(OH)$  difference increases giving  $U_0$  equal to 0.38 V and 0.63 V for Pd and Pd/Pd<sub>0.75</sub>Co<sub>0.25</sub>, respectively. Note that we modeled co-adsorption of O and OH with 0.25 ML of H<sub>2</sub>O which is certainly less than the water coverage in real reaction environment. One may expect that higher coverage of the co-adsorbed water can further improve the reaction energetics.

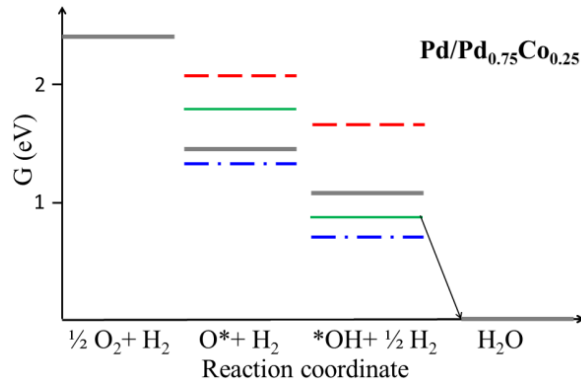


**Figure 5: Reaction free energy diagram built for Pd/Pd<sub>0.25</sub>Co<sub>0.75</sub>. Adsorption configurations and line code is the same as in Figure 4.**

The most pronounced effect is caused by hydroxyl co-adsorption. As shown in Tables 1 and 2,  $E_B(O)$  decreases significantly upon OH co-adsorption, while the increase in the OH coverage from 0.25 ML to 0.5 ML slightly stabilizes the system. This effect leads to a significant increase in  $\Delta G(O)$  and decrease in  $\Delta G(OH)$ . As a result, we obtain for both Pd and Pd/Pd<sub>0.75</sub>Co<sub>0.25</sub>  $\Delta G(O)$  to be greater than  $2\Delta G(OH)$ , which makes the  $HO^* + H^+ + e^- \rightarrow H_2O + ^*$  reaction step determining for the onset potential. Applying  $U_0 = \Delta G(OH)$ , we find  $U_0$  to be equal

to 0.79 V and 0.87 V for Pd and Pd/Pd<sub>0.75</sub>Co<sub>0.25</sub>, respectively. These results are in a very good agreement with experiment [55]. This finding raises the question whether the OH co-adsorption really determines the reaction energetics, or the agreement with experiment is a result of cancellation of effects which have not been taken into account? It is clear that overall effect of the hydroxyl co-adsorption on ORR can be important if the probability for O and OH, as well as for OH and OH, to be adsorbed at neighboring sites in the course of the reaction is high. Hydroxyl can be formed as a result of several possible reaction steps: a)  $O^* + H^+ + e^- \rightarrow HO^*$ , b)  $*OOH + * \rightarrow O^* + HO^*$ , c)  $HOOH^* + * \rightarrow 2HO^*$  [4]. If water is involved in reaction implicitly it also produces OH at some steps [43]. It was also shown that for OH co-adsorbed with water in an O<sub>2</sub> free environment on Pt(111) the OH–OH interaction is attractive up to the 1/3 ML coverage of OH [43, 50]. Based on this consideration, one may expect that in real reaction environment, in which all adsorbate configurations corresponding to various reaction steps are present, the probability of the O–OH and OH–OH co-adsorption is high and its effect in the ORR energetics can be substantial.

As we have mentioned earlier, the OH co-adsorption was found to be favorable for the reaction energetic. However, it is known [1, 56] that increase in the OH coverage can reduce the ORR rate by blocking active sites for the O<sub>2</sub> adsorption. These two (thermodynamic and kinetic) effects may be competing. On the other hand, as discussed above, the O – OH and OH – OH co-adsorption can be achieved without significant increase in the OH coverage.

### 3.2.5 Tracing the Reaction Energetics to the Electronic Structure of the Alloys

As shown above, the binding energies of the ORR intermediates and hence the reaction free energies change significantly upon variation of composition of the Pd-Co alloys. Since chemisorption is determined by hybridization between the electronic states of adsorbate and surface atoms, in this subsection, we evaluate the effect of the surface composition on the hybridization by analyzing LDOS of the adsorbed oxygen and surface atoms for the alloys under consideration. As a representative example, in Figure 6, we show LDOS of the Pd d-states and Co d-states of the surface atoms and p O-states of the adsorbed oxygen calculated for the Pd<sub>0.75</sub>Co<sub>0.25</sub> alloy. One can see that the hybridization of the Pd d-states and O p-states with the spin-polarized d Co states induces spin-polarization for the formers. The non-occupied states of O, which are important for chemisorptions, are formed in the system due to hybridization with the spin-down Co d-states. Since the initial Pd d-states are mostly overlapped energetically with the spin-up Co d-states, their hybridization determines the alloying effect on the Pd LDOS. As we shall see, this effect leads to a low-energy shift of the Pd d-band.

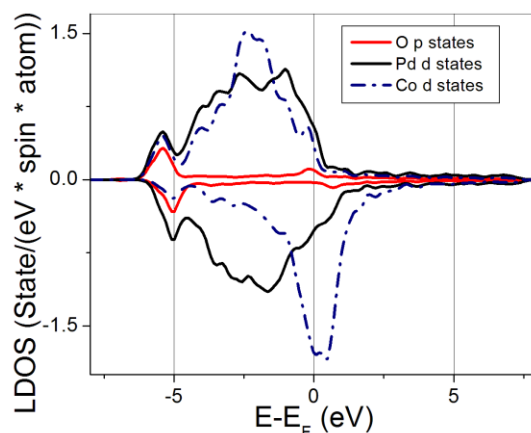
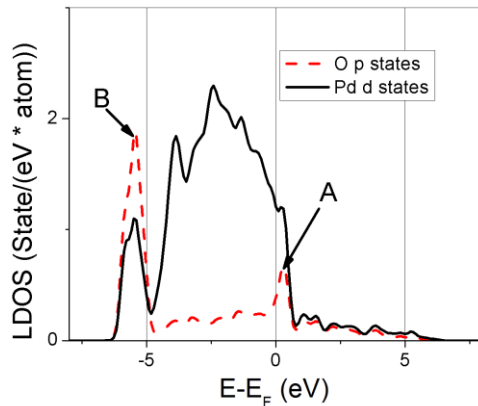


Figure 6: Spin-resolved LDOS of the surface atoms and adsorbed oxygen calculated for Pd<sub>0.25</sub>Co<sub>0.75</sub>.

Since the spin-polarized LDOS has a quite complicated structure, to evaluate the overall effect of hybridization on the chemisorptions of oxygen, we analyze the summed spin-up and spin-down LDOS. As we have shown above the Pd/Pd<sub>0.75</sub>Co<sub>0.25</sub> structure has the most promising reaction energetic among the alloys under consideration. Therefore, we compare and contrast the summed d Pd and p O LDOS for this alloy surface and clean Pd surface (as a reference), both adsorbed with oxygen (see Figure 7 and Figure 8). One can see two distinguished peaks (A and B) formed in the O p LDOS which align with two Pd d LDOS peaks. This suggests a significant hybridization between the O p-states and the Pd d-states resulting in formation of anti-bonding and bonding states represented by A and B peaks, respectively. It is known that the lesser anti-bonding states are populated, the stronger covalent bonding is. Taking into account that the A peak in both systems is almost totally depopulated, we can thus use the ratio of the A peak intensity to the B peak intensity as a qualitative descriptor of the strength the pO – dPd covalent bonding in the systems. We find this ratio to be equal to 0.35 and 0.29 for Pd and Pd/Pd<sub>0.75</sub>Co<sub>0.25</sub>, respectively, suggesting that adsorbed oxygen makes stronger covalent bonds to Pd than to Pd/Pd<sub>0.75</sub>Co<sub>0.25</sub> as shown in tables 1 and 2.



**Figure 7: Spin-summed LDOS of the surface Pd atom and adsorbed oxygen calculated for Pd(111).**

The next question to rise is why the O–Pd covalent bonding is stronger on pure Pd than on the Pd/Pd<sub>0.75</sub>Co<sub>0.25</sub> surface. To answer this question we analyze LDOS of surface atoms of these systems without adsorbate. LDOS of surface Pd atoms calculated for Pd(111) and Pd/Pd<sub>0.75</sub>Co<sub>0.25</sub> (111) are plotted in Figure 9. Note that for Pd/Pd<sub>0.75</sub>Co<sub>0.25</sub> there are two kinds of Pd surface atoms: one has no Co neighboring atoms and the other has one Co neighbor. LDOS of the latter is shown in Figure 9. One can see that the density of the surface Pd d-states around the Fermi-level for Pd/Pd<sub>0.75</sub>Co<sub>0.25</sub> is significantly reduced and the entire d-band is shifted towards lower energies compared to those for Pd(111). As seen from Figure 9, these effects are more pronounced for Pd<sub>0.75</sub>Co<sub>0.25</sub> and even more for Pd<sub>0.5</sub>Co<sub>0.5</sub>. It is important to note that the surface Pd atom in Pd(111) naturally has no Co neighbors, while in Pd/Pd<sub>0.75</sub>Co<sub>0.25</sub>, Pd<sub>0.75</sub>Co<sub>0.25</sub>, and Pd<sub>0.5</sub>Co<sub>0.5</sub> it has one, three, and six nearest Co neighbors, respectively. We thus find a close correlation between energetic position of the d-band of surface Pd atom and the number of its Co-nearest neighbors, this is: the more Co neighbors Pd atom has the deeper its d-band is located. This correlation reflects the discussed above effect of the hybridization between Pd d-states and Co d-states, which causes a low energy shift of the Pd d-band. The position of the Pd d-band center with respect to the Fermi-level, plotted versus number of Pd-Co bonds, clearly illustrates this correlation (see Figure 10). This finding is very important, because the quantity of our interest – strength of covalent O–Pd bonding is determined by hybridization of both occupied and non-occupied oxygen and metal states, which in turn depends on the density of the metal d-states around the Fermi-level. If the d-band shifts towards lower energies upon composition variation, the density of d-states around the Fermi-level decreases which causes weakening the oxygen metal bond. This effect is depicted in the simple and widely used model [57] which

correlates the d-band center position with the adsorption energy of oxygen or other species. We can thus conclude from our results that the hybridization of Pd d-states and Co d-states in Pd/Pd<sub>0.75</sub>Co<sub>0.25</sub> causes a low-energy shift of the d-band center of the surface Pd atoms, with respect to that of the Pd(111), which in turn leads to a weakening of the O – Pd covalent bond and a decrease in the O binding energy. Note that, as we move from Pd and Pd/Pd<sub>0.75</sub>Co<sub>0.25</sub> to Pd<sub>0.75</sub>Co<sub>0.25</sub> and Pd<sub>0.5</sub>Co<sub>0.5</sub>, the Pd d-band center is shifted toward lower energies, while the O bonding is strengthening significantly. This happens because Pd<sub>0.75</sub>Co<sub>0.25</sub> and Pd<sub>0.5</sub>Co<sub>0.5</sub> have surface Co atoms and the O binding energy is determined rather by the stronger Co–O bonding.

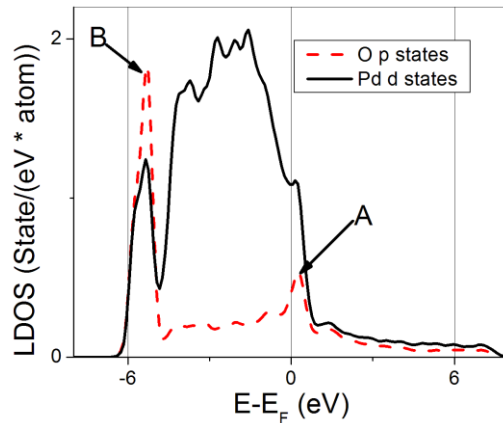


**Figure 8:** Spin-summed LDOS of the surface Pd atom and adsorbed oxygen calculated for Pd/Pd<sub>0.25</sub>Co<sub>0.75</sub>(111).

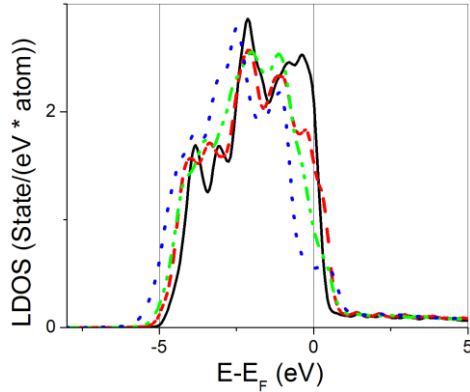


**Figure 9:** Spin-summed LDOS of the Pd(111) surface. Pd atom calculated for pure Pd (solid line), Pd/Pd<sub>0.25</sub>Co<sub>0.75</sub> (dash line), Pd<sub>0.25</sub>Co<sub>0.75</sub> (dash-dot-dot line) and Pd<sub>0.5</sub>Co<sub>0.5</sub> (dot line).

As mentioned in Introduction of this chapter, the authors in [42] propose the contraction of Pd – Pd bonds caused by alloying with Co to be the factor which changes the electronic structure and binding energy of oxygen. Our results bring us to a different conclusion. As seen from Figure 9 and Figure 10, the Pd d-band center is deeper for Pd<sub>0.75</sub>Co<sub>0.25</sub> than for Pd/Pd<sub>0.75</sub>Co<sub>0.25</sub> even though these two systems have the same lattice parameter and hence the same Pd–Pd bond length. Furthermore, as shown in Figure 11, two non-equivalent Pd surface atoms of Pd/Pd<sub>0.75</sub>Co<sub>0.25</sub>, have significantly different LDOS: the Pd atom that has a Co nearest neighbor has lower density of states around the Fermi-level and deeper the d-band center than the other Pd surface atom that has only Pd nearest neighbors. The results thus bring us to the conclusion that the d-states hybridization between Pd and Co atoms is the main factor which controls the LDOS of Pd atoms and the oxygen binding energy in Pd–Co alloys with surface segregation.

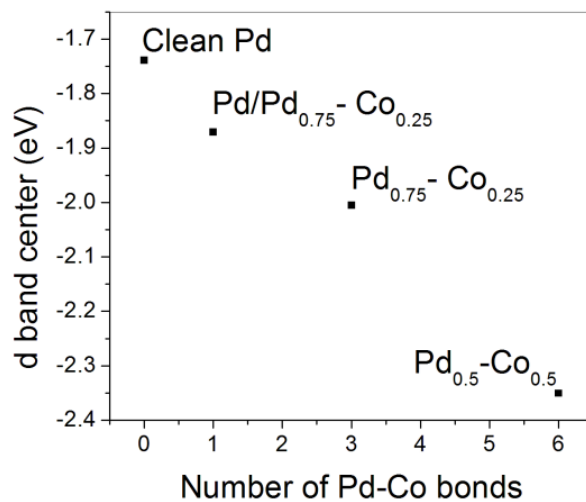


Figure 10: Energy of the Pd d-band center counted for the Fermi-level as a function of the neighboring Co atoms.

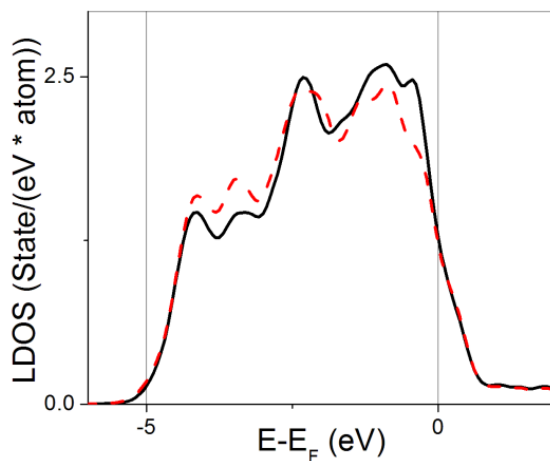


Figure 11: Spin-summed Pd LDOS calculated for Pd/Pd<sub>0.25</sub>Co<sub>0.75</sub>(111) for the surface Pd atoms which have no Co neighbor (solid line) and has one Co neighbor (dash line).

### 3.2.6 Conclusions

The Pd segregation towards the surface in the Pd-Co alloys observed in experiment is essential for improving electro-catalytic properties of these materials. Indeed, the binding energy of the ORR intermediates on Pd/Pd<sub>0.75</sub>Co<sub>0.25</sub> are found to be lower than that on Pd(111) which is

favorable for the reaction, while the Pd<sub>0.75</sub>Co<sub>0.25</sub> and Pd<sub>0.5</sub>Co<sub>0.5</sub> surfaces are too reactive for ORR due to bonding to the surface Co atoms. The results show that the hybridization between Pd d-states and Co d-states causes the low energy shift of the d-band of surface Pd in Pd/Pd<sub>0.75</sub>Co<sub>0.25</sub>, which causes weakening the bonding of the intermediates to the surface.

Co-adsorption of the ORR intermediate and water is found to change the reaction energetics significantly. We have built the ORR free energy diagrams for the Pd and Pd/Pd<sub>0.75</sub>Co<sub>0.25</sub> and estimated the onset electrode potential for the reaction. For the intermediates adsorbed with 0.25 ML coverage, the estimated from the calculations  $U_0$  is found to be much lower than in experiment. Co-adsorption with water slightly improves the results, while the diagrams built for the O – OH and OH – OH co-adsorption configurations provide  $U_0$  which are in a good agreement with experiment. The oxygen binding energies, obtained for Pd and Pd/Pd<sub>0.75</sub>Co<sub>0.25</sub> support the assumption [32, 33] that  $E_B(O)$  can be used as a descriptor of the ORR activity.

### **3.3 First Principle Calculations on Pd/X/Pd Sandwich Like Structures**

As mentioned on previous sections, considerable effort has been made to reduce the content of Pt used in the FC electrodes as well as to enhance the catalytic activity of such systems by depositing a Pt monolayer on different substrates[58, 59, 60, 61].

Concerning Pt free materials, Pd-based alloys have been extensively studied. In particular Pd-Co alloys have shown promising catalytic properties towards the ORR [36, 37, 38, 39]. Among the theoretical studies on Pd-Co alloys concerning the study of the ORR, for the

purposes of this section, is worth mentioning the work done by Son and Takahashi[62] where they study Pd-Co alloys finding that maximizing the number of Co atoms at the second atomic layer underneath a Pd skin enhances the catalytic activity of the system. Also, experimental results on the literature have shown a Pd segregation towards the surface in Pd-Co alloys, resulting in a Pd rich skin [39, 58, 63]. On the other hand, Shao and co-workers [64] have shown that on Pd-Fe systems exhibit an enhancement in the catalytic activity towards the ORR surpassing the one achieved by carbon supported Pt.

There are indications that the interaction between the substrate and the catalytic active monolayer on top is responsible for the previously mentioned enhancement in the catalytic activity of Pd-Co and Pd-Fe systems, where the system's surface is rich in Pd. This idea has been used by the authors of ref[65], who proposed a rational design of electro catalytic systems towards the ORR based on the hybridization between substrate and surface layer. The results on Pd-Co alloy systems described in the previous section and published in ref[66] have shown that the hybridization of Pd and Co d-states reduces the d-band center of Pd atoms as well as the LDOS around the Fermi level, making the Pd atoms less reactive towards O adsorption. Based on this idea we propose Pd/M/Pd (M=Co or Fe) systems as a promising ORR catalysts. In this section we present our results on such systems comprised of a Pd substrate covered by a monolayer of Co or Fe and Pd monolayer on top. Three systems will be described and analyzed in this section: Pd slab and Pd slab with a Co or Fe monolayer deposited on the surface followed by a Pd skin (Pd/Co/Pd) and (Pd/Fe/Pd) respectively. These three systems have the same lattice constant, therefore no strain effects will be present, allowing us to focus on the effects caused by the hybridization between the top two layers.

We have a reason to believe that these materials will be stable because of a number of experimental works studying similar structures. For example, in the case of Pd-Fe systems, Ueno et al.[67] deposited Fe and Pd on Pd(001) surface via an e-beam evaporation source at a temperature of 310 K, the authors were able to fabricate Fe/Pd and Pd/Fe/Pd systems. Using low-energy electron diffraction measurements, the authors were able to determine that in the case of Fe/Pd system, the surface was comprised of 35% of Fe atoms and 65% of Pd atoms, while the 65% of Fe atoms were located at the second layer. On the other hand, for the Pd/Fe/Pd sample, the authors found that the surface was comprised only by Pd atoms, the second layer contained 10% of Fe atoms, while the 90% of the Fe atoms were localized at the third layer. Lehnert and coworkers[68] have prepared similar systems where Fe and Co ultrathin layers (1 monolayer) have been deposited on Rh(111) and Pt(111) substrates.

The Pd-Co and the Pd-Fe bonds are stronger than the Pd-Pd bonds. Also the Co-Co and the Fe-Fe bonds are stronger than the Pd-Co and the Pd-Fe bonds. Therefore it is energetically more favorable to have a Pd/M/Pd (M=Co or Fe) than a M/Pd system, this behavior will be shown on subsection 3.3.5. A deeper analysis on this sandwich-structure system can be found in ref[65]. A similar system has been studied by Wadayama et al. in ref[69], where the authors deposited Ni onto a clean Pt(111) surface with an electron-beam evaporator at different temperatures. Infrared reflection absorption spectroscopy (IRRAS) measures were performed, allowing them to make a comparison between the C-O stretch frequency of the CO adsorbed on the Ni/Pt sample treated at temperature of 823 K and the CO adsorbed on a second fabricated Pt/Ni/Pt(111) “sandwich” sample. The results indicated that the Ni/Pt sample treated at a temperature of 823 K has a Pt/Ni/Pt sandwich-like structure, where the Ni atoms are localized at

the second layer. Also the authors show that the catalytic activity towards the ORR is higher in the Pt/Ni/Pt structure than in the Pt(111) surface.

In order to characterize the Pd/M/Pd (M=Co or Fe) systems, we will continue using the idea of relating the d-band center and the O adsorption as was described in [57] ( as is shown for different metals on ref[39] and ref[70]) and we will use the O, OH and OOH binding energies as a descriptor of the ORR. It is important to highlight the linear relation between the binding energies of O,OH and OOH described by Norskov and coworkers[31]. As we will see, this effect is present also for the systems under consideration.

The results of this study are organized as follows: subsection 3.3.1 starts by giving a short description of the computational details. In sub-section 3.3.2 we discuss the change in the d-LDOS of Pd atoms due to hybridization with Co and Fe atoms on the second layer and how these changes affect the binding energy of the intermediates (O, OH and OOH). In sub-section 3.3.3 we compare the binding energy of the intermediates for a 0.25 monolayer (ML) with and without OH and H<sub>2</sub>O co-adsorption for the three systems under consideration. In sub-section 3.3.4 we compare the catalytic activity of the three systems by making a comparison between the free energy diagrams as described in the introduction of this chapter. Sub-section 3.3.5 discusses the stability of the system in vacuum, against oxidation and in acidic media, which is one of the major concerns in fuel cell systems. Finally, the conclusions will be found in sub-section 3.3.6.

### **3.3.1 Computational Details**

For all system under consideration, the electronic structure and the equilibrium position of the atoms were obtained using the code VASP 5.2[46], with projector augmented wave

potentials [47] and the Perdew-Burke-Ernzerhof (PBE) version of the generalized gradient approximation (GGA) for the exchange and correlation functional ref[48]. All systems, except for clean Pd, were calculated taking into account spin polarization. In order to simulate the surface we use a supercells with a 7 layer slab and vacuum layer of 14 Å. For all calculations the supercells had the  $(2 \times 2)$  in-plane periodicity. The  $(7 \times 7 \times 1)$  k-point samplings in Brillouin zone used in this work provide sufficient accuracy for the characteristics obtained by integration in the reciprocal space. The cutoff energies of 400 eV and 600 eV were used for the plane wave expansion of wave functions and charge density, respectively. To achieve structural relaxation, a self-consistent electronic structure calculation was followed by calculation of the forces acting on each atom. Based on this information the atomic positions were optimized to obtain equilibrium geometric structures in which forces acting on atoms do not exceed 0.02 eV/Å.

To obtain the zero point energies (ZPE), we have calculated the vibrational frequencies of the intermediates O, OH, OOH and H<sub>2</sub>O using the finite-difference method. Since masses of the ORR intermediates are much smaller than those of the substrate, only the intermediates vibrational modes were taken into account leaving the slab atoms frozen. Five displacements were used for each direction with a step of 0.02 Å.

The geometric structures of clean and adsorbed surfaces shown in this article have been plotted using the Xcrysden software ref[49].

According to our results on bulk Pd, for the three systems under consideration the lattice constant was set to 3.962 Å. The lattice constant mismatch between Pd and Fe or Co has no relevance due to the small concentration of Co and Fe in the Pd slab (Co and Fe form an atomic

monolayer below the Pd atoms at the surface, followed by Pd bulk). For the Pd/Co/Pd system, the layer stacking follows the ABCABC pattern of the Pd(111) surfaces, but in the case of Pd/Fe/Pd our results shown that the Pd layer, deposited on top of the Fe layer, prefers to align with the Pd layer below the Fe atoms, forming a ABA stacking pattern for the three top most layer of the system (Pd/Fe/Pd). The rest of the slab maintains the ABCABC stacking configuration.

### 3.3.2 Results on the Local Density of States

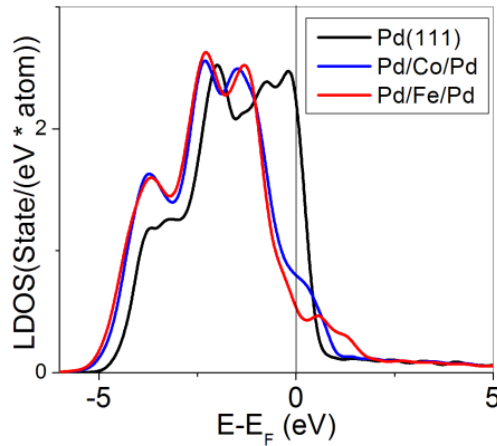


**Figure 12: Spin summed LDOS of d-states Pd atoms on the system surface for clean Pd(111) (black line), Pd/Co/Pd (blue line) and Pd/Fe/Pd (red line).**

Figure 12 shows the spin summed d-LDOS of one surface Pd atom in each one of the systems under consideration (Pd (111) surface, Pd/Co/Pd and Pd/Fe/Pd). As can be seen, the magnitude of the LDOS around the Fermi level follow the order Pd(111)> Pd/Co/Pd> Pd/Fe/Pd. Using the LDOS shown Figure 12, the d-band center of the Pd surface atoms for each one of the system under consideration were calculated, finding that the d-band center of Pd atoms in the

Pd/Co/Pd and Pd/Fe/Pd are shifted by 0.260 and 0.307 eV respectively, towards lower energies with respect to the Pd(111) system. This shift of the d-band and consequent reduction of the LDOS at the Fermi level is expected to lead to a reduction in the intermediates binding energy and a consequent increment in the catalytic activity of the system, as we will show in following sub-sections.

In the previous section we have shown that the hybridization of d-states between Pd and Co atoms is responsible for the low energy shift of the d-band center of the Pd atoms. In Figure 13 panel **a** we show the spin up and spin down d-LDOS of the Pd and Fe atoms at the surface and the second layer respectively, it can be seen that overlapping of the spin down (spin minor) states of the Pd and Fe atoms is small, while the spin up (spin major) states (the occupied d states of Pd and Co atoms) strongly overlap and thus hybridize determining the alloying effect on the LDOS and shifting the d-band center to lower levels and reducing the density of states around the Fermi level of the surface Pd atoms. In Figure 13 panel **b** we present the spin up and spin down d-LDOS of the Pd and Co atoms at the surface and the second layer respectively, the analysis of the figure is completely analogous to the one done for the Pd/Fe/Pd system (Figure 13 panel a) described above.

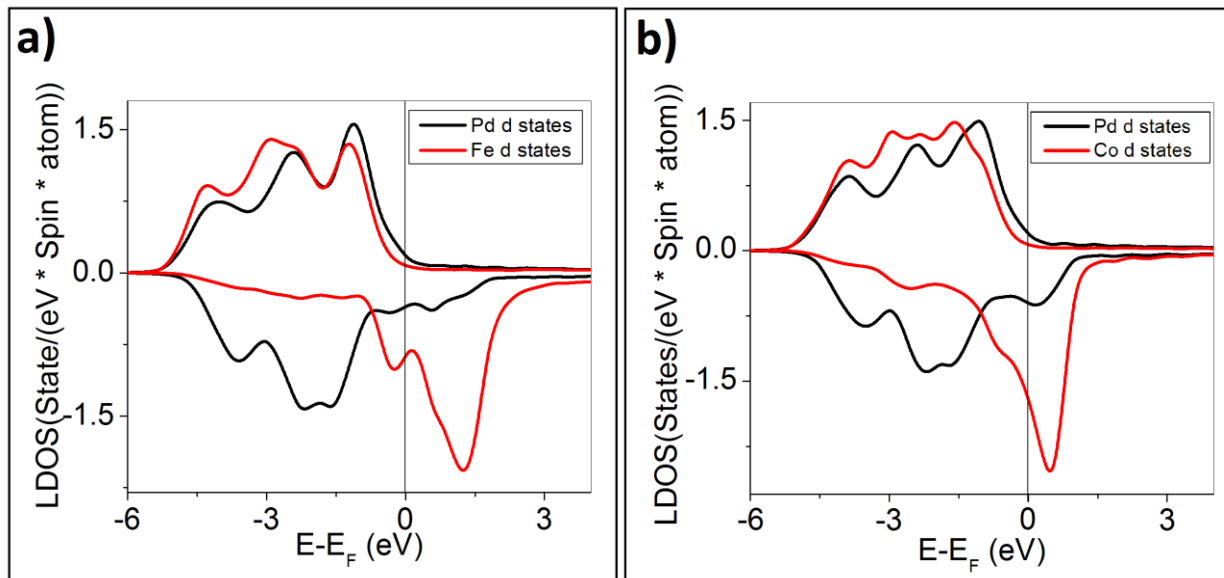


Figure 13: Spin resolved d-LDOS. Panel a: Pd/Fe/Pd system. Panel b: Pd/Co/Pd system. Black lines denote the d-states of Pd atoms at the top layer, while red lines denote the d-states of Fe or Co atoms (Fe d-states for panel a and Co d states for panel b) on the second layer.

### 3.3.3 Results on O, OH and OOH Binding Energies

For the three system under consideration the O, OH and OOH binding energies were calculated on all the non-equivalent adsorption sites with a 0.25 coverage (one intermediate per unit cell), finding that the fcc hollow site is preferred for the O, OH adsorption, while the bridge site is preferred for the OOH adsorption.

Table 3: O, OH and OOH binding and zero point energies for 0.25 ML coverage on Pd, Pd/Co/Pd and Pd/Fe/Pd, on the preferred adsorption site.

Adsorbate	Slab	$E_B$ (eV)	ZPE (ev)
<b>O</b>	Pd	4.634	0.072
	Pd/Co/Pd	4.071	0.066
	Pd/Fe/Pd	3.853	0.064
<b>OH</b>	Pd	2.594	0.320
	Pd/Co/Pd	2.534	0.290
	Pd/Fe/Pd	2.427	0.300
<b>OOH</b>	Pd	1.165	0.423
	Pd/Co/Pd	1.094	0.426
	Pd/Fe/Pd	0.937	0.430

Table 3 presents the binding energies and the zero point energies of intermediates (O, OH and OOH) adsorbed on Pd(111), Pd/Co/Pd and Pd/Fe/Pd. In this table it can be seen the linear relation between the binding energies of O, OH and OOH mentioned in the introduction. The binding energies of the intermediates in the three systems follow the order Pd(111) > Pd/Co/Pd > Pd/Fe/Pd. This, as mentioned above, was an expected result since the surface Pd atoms d-band center is lower for the Pd/Co/Pd and Pd/Fe/Pd than for Pd(111) systems (see Figure 12). Similar results for O binding energy have been reported on Pt-(Co or Fe) systems[71].

It is worth noticing that the largest difference in the zero point energy between systems is not higher than tens of meV, which is negligible and allow us to take the term “ $\Delta ZPE_i - T\Delta S_i$ ” in equation (3.11) as constant values for the three systems. As we have mentioned earlier this is:  $\Delta ZPE_i - T\Delta S_i = -0.046, 0.252$  and  $0.263$  eV for O, OH and OOH respectively.

**Table 4: Binding energies of intermediates co-adsorbed with 0.25 ML coverage of OH and H<sub>2</sub>O, on the preferred adsorption site.**

Slab	Co-adsorbate	O binding energy (eV)	OH binding energy (eV)	OOH binding energy (eV)
Pd	OH	4.230	2.767	1.603
	H <sub>2</sub> O	4.770	2.874	1.653
Pd/Co/Pd	OH	3.893	2.773	1.193
	H <sub>2</sub> O	4.203	2.957	1.692
Pd/Fe/Pd	OH	3.482	2.495	1.111
	H <sub>2</sub> O	4.147	2.941	1.651

To simulate a more realistic scenario, the binding energies of the intermediates shown in Table 3 were calculated also with the co-adsorption of OH and H<sub>2</sub>O, leading to 0.50 ML coverage of the intermediates on the surface. This results are presented in Table 4. Comparing Table 3 and 4 three different trends are observed: a) the O binding energy decreases with the co-

adsorption of OH for the three systems, b) OH co-adsorption stabilizes other OH molecules adsorbed on the surface and c) water stabilizes all the intermediates (O, OH and OOH). This behavior can be explained appealing to the electrostatic interaction between intermediates adsorbed on the Pd surface as follows: Upon adsorption, the O and H atoms of the intermediates become negatively and positively charged respectively, creating an electrostatic interaction between intermediates. Analysis of the geometry and energetics of co-adsorption reveals the following trends: despite the attraction between the negative charge O atoms and the positive charge H (the H that comprise the OH adsorbed molecule), the electrostatic repulsion between the negative charged O atoms, of O and OH, reduces the binding energy. A similar observation is done for co-adsorption of O and OH: the positive charged H atoms tilts and rotates towards neighboring charged O atoms, see Figure 14, due to the electrostatic attraction between H and O atoms, increasing the binding energy of the intermediates (O, OH and OOH). The geometries of the intermediates co-adsorbed with other OH and H<sub>2</sub>O molecules on Pd/Co/Pd and Pd(111) surfaces are very similar to the Pd/Fe/Pd ones (see Figure 14), therefore are not present in this section.

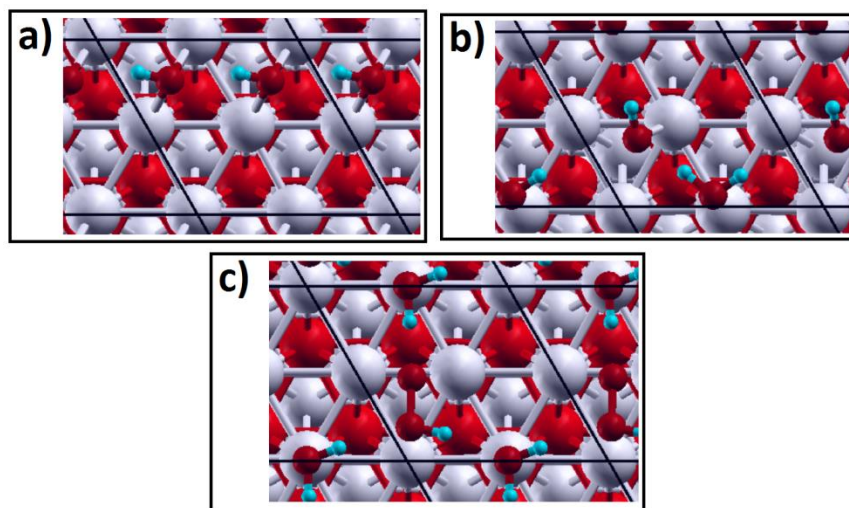


**Figure 14: Intermediates adsorbed on Pd/Fe/Pd system. Panel a: relaxed OH co-adsorbed with OH on Pd/Fe/Pd (0.5 ML coverage). Panel b: relaxed OH co-adsorbed with H<sub>2</sub>O on Pd/Fe/Pd (0.5 ML coverage). Panel c: relaxed OOH co-adsorbed with H<sub>2</sub>O on Pd/Fe/Pd (0.5 ML coverage).**

### 3.3.4 Free Energy Diagrams

In order to link the intermediates binding energy to the ORR, we have used equation (3.11) and the intermediates binding energies presented in tables 3 and 4 to construct the free energy diagrams of the ORR in presence of 0.25 ML coverage of water (see Figure 15). On panel **a** the electrode potential is set to 0 eV ( $U=0$ ), while in panel **b** the electrode potential was set to 0.548 eV ( $U=0.548$  eV). At  $U=0$  eV (see Figure 15 panel **a**), the reaction is exothermic for the three systems under consideration. Now, Figure 15 panel **b** shows that at  $U=0.548$  eV the only system maintaining the exothermic character of the reaction is Pd/Fe/Pd, while the ORR reaction on the Pd/Co/Pd and Pd(111) systems becomes non-exothermic in the last two steps. These results allows us to conclude that the onset potential and the catalytic properties towards the ORR of the three systems under consideration follow the order Pd/Fe/Pd > Pd/Co/Pd > Pd(111).

The enhancement in the catalytic activity of the Pd/Fe/Pd system is in good agreement with the experimental results obtained in [64]. The Authors in [64] explain the experimentally observed catalytic activity enhancement, by arguing a change in the DOS due to strain effects caused by the lattice constant mismatch between Fe and Pd atoms. On the contrary, our results suggest that the enhancement in the catalytic activity exhibit by Pd-Fe systems is due to hybridization effects between the Pd atoms at the surface and the Fe atoms localized in the second layer of the system.

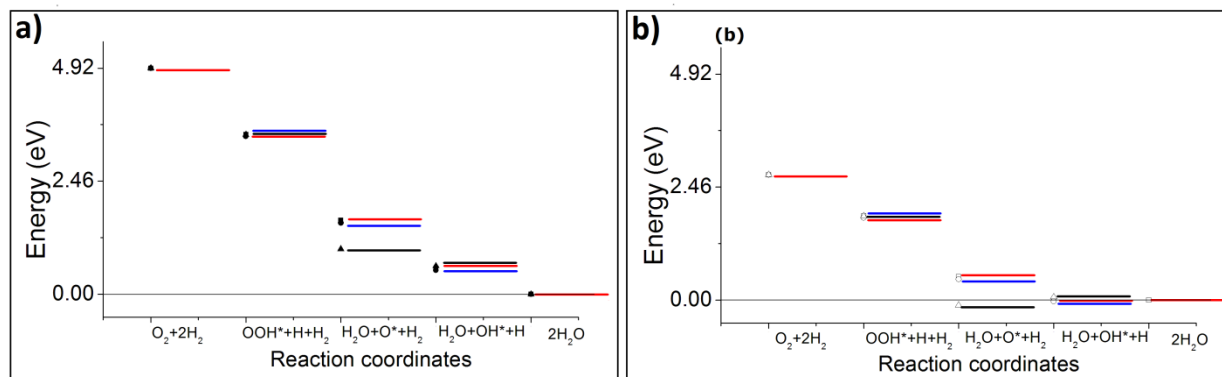


**Figure 15: ORR free energy diagrams for Pd(111) (black line), Pd/Co/Pd (blue line) and Pd/Fe/Pd (red line) in presence of 0.25 ML of  $H_2O$ . Panel a:  $U=0$  eV, panel b:  $U=0.548$  eV.**

### 3.3.5 Results on the Stability of the System

It has been shown above that the hybridization of the  $d_{Pd} - d_{(Co, Fe)}$  states is the key factor in reducing the reactivity of the system towards the adsorption of the intermediates (O, OH and OOH), leading to the enhancement in the catalytic activity of the system. However, it is well known that Co and Fe atoms are very reactive towards the adsorption of O (and as a consequence towards OH and OOH, see Table 1), making the segregation of Co or Fe atoms towards the surface an undesired effect. With this in mind, we performed calculations on the energy

difference between the Pd/X/Pd (X=Co or Fe) system and a second system where all the Co or Fe have been segregated towards the surface (X/Pd), finding that the segregation of Co and Fe atoms towards the surface increases the energy of the system by 0.556 and 0.751 eV per surface atom respectively. This allows us to conclude that this particular segregation is energetically not favorable. We expected this because the Pd-Co or Pd-Fe bonds are stronger than the Pd-Pd and a segregation of Fe or Co towards the surface would reduce the number of Pd-Co and Pd-Fe bonds from six to three.

Another concern is the penetration of O from the surface to the second layer making a bond with the Co or Fe atoms, in other words the oxidation of the second layer. This oxidation will lead to a new shift in the d band center towards the Fermi level of the surface Pd atoms, making the system more reactive toward the adsorption of the intermediates and leading to a reduction of the catalytic activity of the system. This effect can be seen in Figure 16 where we show a comparison between the d-LDOS of Pd atoms at the surface with and without oxygen bonded to Fe atoms on the second layer. Regarding this issue, our calculation shows that the energy of the system increases when the oxygen goes from the surface to the second layer (making a bond with the Fe or Co atoms) by 0.332 eV and 0.01 eV respectively. In the first case, we can conclude that the Pd/Fe/Pd system is stable toward oxidation. However, for the second system (Pd/Co/Pd), even though the difference in energy is small, the oxidation is unlikely to happen due to the expected energy barrier between the two states.

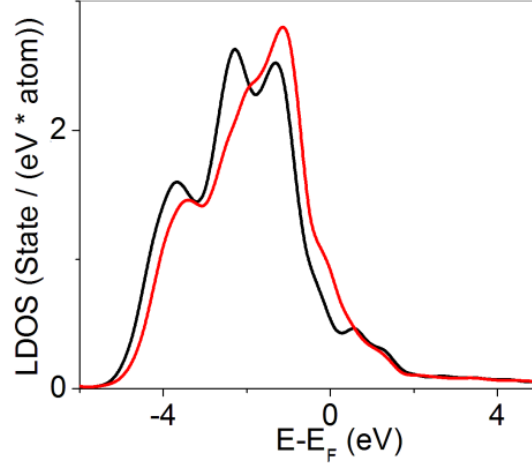


**Figure 16: Spin summed d-LDOS of surface Pd atoms on the Pd/Fe/Pd system. Black line corresponds to the pristine Pd/Fe/Pd system. Red line corresponds to the Pd/Fe/Pd system with one O atom in between the Pd and Fe layer (oxidized system).**

Now, since the final goal is to use the systems under consideration in FC devices, the dissolution potential in acidic media is a major concern in this kind of systems. It is well known from literature that the dissolution potential for Pd is 0.95 V (pH0)[72]. Based on the work done by Greeley and Norskov [73], if the dissolution potential  $U^0$  of a given system is known, the dissolution potential  $U$  of a related system can be calculated through the following equation:

$$l(U - U^0) = E_{Pd,Bulk} - \frac{E_{Pd/X/Pd} - E_{X/Pd}}{N}. \quad (3.15)$$

Where “ $l$ ” is the number of electrons transfer ( in this case  $l=2$ ),  $E_{Pd,Bulk}$  is the DFT calculated energy per Pd atom (Pd bulk calculation),  $E_{Pd/X/Pd}$  corresponds to the Pd/X/Pd (X=Co,Fe) system’s energy,  $E_{X/Pd}$  is the energy of the Pd/X/Pd (X=Co,Fe) system without the Pd atoms on the first layer (X atoms on top of the Pd (111) surface) and finally  $N$  is the number of Pd surface atoms in supercell (for the systems under consideration  $N=4$ ).

Using equation (3.15) we calculated that the dissolution potential (at pH0) for the two systems Pd/Co/Pd and Pd/Fe/Pd are 1.23 and 1.32 V respectively, which is higher than the ideal onset potential for a proton exchange membrane fuel cell, allowing us to conclude that both systems are stable in acidic media.

### **3.3.6 Conclusions**

In this project we proposed the sandwich like structures Pd/Co/Pd and Pd/Fe/Pd as two new catalytic materials towards the ORR. Our calculations predict an enhancement in the catalytic activity toward the ORR over Pd surfaces due to the reduction in the binding energy of the intermediates O, OH and OOH. The lower reactivity of the surface towards the adsorption of the intermediates was traced to the hybridization of dPd and d(Co,Fe), which causes a shift to deeper energy levels in the d-band center of the surface Pd atoms. Furthermore, according to our calculations both systems are stable on vacuum, against oxidation and have a dissolution potential higher than the optimal onset potential of a proton exchange membrane fuel cell.

## **3.4 Strain and Hybridization Effect on Catalytically Active Monolayers on Metal Substrates**

As we have mentioned in chapter 1, Pt is a widely used material used in both electrodes of PEMFC and DMFC. However, several problems have to be overcome before a large scale implementation can be possible. For example, the performance of both PEMFC and DMFC suffers from low rate of the oxygen reduction reaction (ORR) on the Pt cathode. When Pt is used as anode catalysts, it suffers from poisoning by CO, which comes with hydrogen produced from

natural gas in the case of PEMFC and as a product of methanol (ethanol) decomposition in the case of DMFC (DEFC), without mentioning the scarcity of the element.

A great amount of work has been done in order to solve the above mentioned problems. For example, a Pt monolayer supported on Au(111) substrate has been reported to be more active towards the methanol and ethanol electro-oxidation than Pt(111)[74]. Pt sub-monolayer deposited on Ru nano particles[75, 76] and other Pt monolayers on Ir [77] have shown a higher CO poisoning tolerance than Pt systems.

The reduction in the amount of Pt has been achieved by core-shell nanoparticle designs[2, 5, 78, 79], in most of these cases the system is comprised by depositing an active element (AE), in this case Pt, on top of a metal substrate (MS). This causes two different effects: a) In general, a mismatch between the AE and MS lattice constant will occur, the AE will retain the pattern of the MS causing a change in the AE-AE bonds, which is a very well-known effect called strain and b) the contact of the AE monolayer with the MS causes the hybridization of the electronic states. Both effects have a direct impact on the reactivity of the AE towards to O or OH adsorption (good descriptors of the ORR, as mentioned in this work). For example, if the AE layer in AE/MS is expanded as compared to its bulk bond length, the AE-AE wave function overlapping is reduced. This causes a narrowing of the AE d-band, resulting in a shift of the d band center towards the Fermi level and the increase of the LDOS at the Fermi level, making the AE/MS more reactive towards the O and OH adsorption. Also it is clear that the AE-MS hybridization has a direct impact on the AE d-states changing the d-band center and the LDOS at the Fermi level. For example, if the reactivity of the AE is low due to deep position of the d-

states and d-band center and if the MS has a high density of states at the Fermi level, the AE-MS hybridization will cause the shift in the d-band center and the increase in the LDOS around the Fermi level. This will increase the reactivity of the AE/MS system towards the O and OH adsorption[65]. This effect is illustrated in sections 3.2 and 3.3

Nevertheless, several authors[74, 39, 80] focus on the strain effect, paying little attention to the hybridization effects. In this section we will focus on Pt/MS (MS= Ru, Pt or Au) system, studying and analyzing the strain and hybridization effects and its contributions to the change of the Pt d-states. We will use the OH binding energy as a descriptor of the system's reactivity because appears as a key intermediate in different reactions such as the ORR, CO removal from anodes in FC and the oxygen evolution in the photo-catalytic splitting of water.

### **3.4.1 Computational Details**

For all system under consideration, the electronic structure, energetics and equilibrium atomic configurations are obtained using the VASP5.2 code [46] with projector augmented wave potentials [47] and the Perdew-Burke-Ernzerhof (PBE) version of the generalized gradient approximation (GGA) for the exchange and correlation functional [48]. For all the system under consideration, a 2x2 Pt(111) layer deposited on top of 5 layer of MS (MS=Pt, Ru(0001) and Au(111)) followed by a vacuum of 12 Å were used. Concerning the K point sampling of the Brillouin zone, a (7x7x1) grid around the  $\Gamma$  point was used. The cut of energy of 400 eV was used for the plane wave expansion of wave functions and the 605 eV cut of energy was used for the charge density. The atoms were allowed to relax until the force acting on each one of the atoms in the system was less than 0.02 eV/Å or less was achieved in each atom.

The figures showing the positions of the atoms were plotted using the Xcrysden software ref[49].

### 3.4.2 Results on the LDOS

To evaluate the strain and interlayer hybridization effects, we have selected five systems: Pt(111) surface, Ru slab covered with a Pt monolayer (Pt/Ru) and a Au slab covered with a Pt monolayer (Pt/Au). The lattice constant of the 3 systems, Pt, Pt/Ru and Pt/Au, were set according to our DFT calculations of bulk Pt, Ru and Au respectively. In addition to these three systems two additional systems were taken under consideration: Pt(111) with lattice parameter contracted and expanded to the a-parameter of hcp Ru (Pt-contr) and fcc Au (Pt-expnd). We should mention that in the chosen reference frame, all the surfaces are oriented in the xy plane.

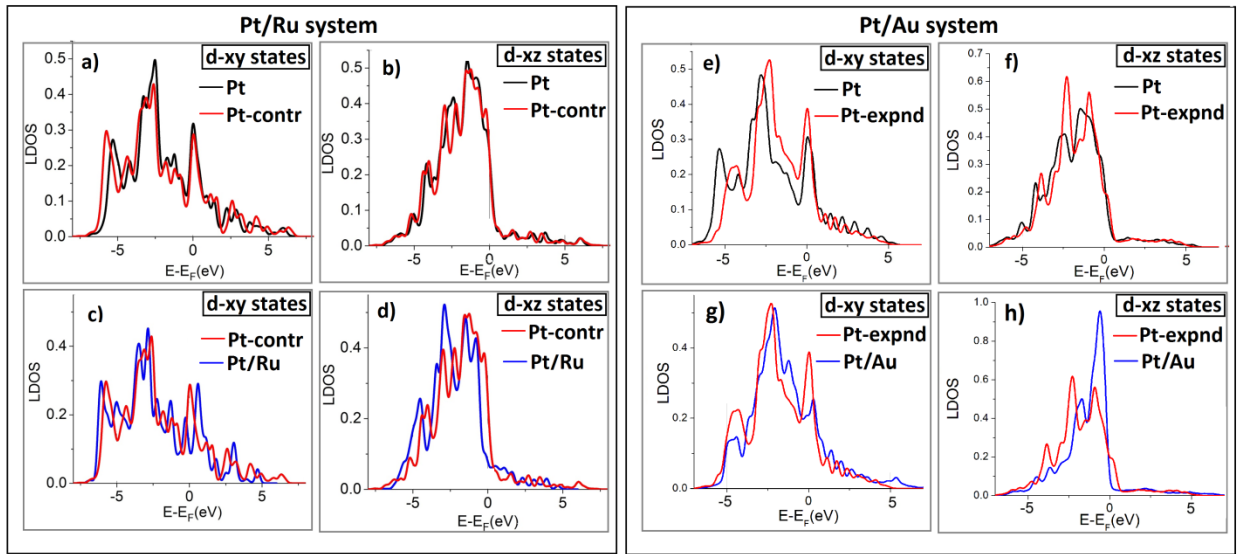


**Figure 17: Surface Pt atoms d-xy and d-zx LDOS. Left panels: Comparison between Pt/Ru and Pt-contr systems, right panels: Comparison between Pt/Au and Pt-expnd systems. Pt-contr stands for Pt slab contracted to the a-parameter of the hcp Ru bulk system, while Pt-expnd stands for Pt slab expanded to the a-parameter of the fcc Au bulk system.**

In Figure 17 we plot, compare and contrast the d-xy and d-xz LDOS of the surface Pt atom in the following systems: Pt/Ru(001), Pt/Au(111), Pt(111), Pt-expnd and Pt-contr. As can be seen from panel **a**, the d-xy states respond to the bond contraction and expansion as expected: the sub-band is shifted toward lower energies. The d-xz states, however, hardly change upon contraction (see panel **b** of Figure 17).

The difference in the strain effect on the d-xy- and d-xz states is naturally explained by the fact that the in-plane oriented d-xy states are sensitive to the change in lattice parameter due to their geometry. In addition, lattice contraction is usually accompanied by increase in the first–second layer separation that compensates the contraction effect on overlapping of the surface atom d-xz-states with the second layer electronic states.

What is very important here is that surface reactivity is determined by the z-oriented states, because they are involved in the hybridization with the adsorbate electronic states. However, the z-oriented states hardly react to the contraction. We thus should not expect a noticeable decrease in the Pt(111) reactivity upon the lattice contraction even though the d-band center moves toward lower energies due to the in-plane state contribution.

Next, we compare the d-xy and d-xz states of surface Pt atoms in the contracted Pt(111) and Pt/Ru(0001) (see panels **c** and **d** in Figure 17). Importantly, both structures have the same in-plane Pt–Pt bond lengths, therefore, all differences in the projected LDOS should be totally attributed to the interlayer hybridization. One can see that, in this case, the difference in the d-xy LDOS is not quite pronounced, whereas the d-xz-sub-band is significantly shifted toward lower energies as compared to that of the contracted Pt. This shift should cause a decrease in surface

reactivity. We thus can expect the Pt/Ru surface reactivity to be lower than that of Pt(111) that purely results from interlayer hybridization of the z-oriented d-states of Pt.

We have performed a similar analysis for Pt(111), Pt/Au(111), and Pt(111) with the lattice parameter expanded to that of Au (see panels **e**, **f**, **g** and **h** of Figure 17 ) and came to similar conclusions: the lattice expansion of Pt causes a noticeable narrowing of the d-xy-sub-band (see panel **e** of Figure 17), while the d-xz-sub-band hardly responds to the expansion (see panel **f** of Figure 17 ). On the other hand, the Pt d-xz sub band in Pt/Au is found to be much narrower than that in Pt with both equilibrium and expanded lattice parameters (see panel **h** of Figure 17). This narrowing is caused by the interlayer hybridization of Pt and Au d-states, which is weak because of energetic separation of the d-bands of Au and Pt (Au states are localized at lower energies than the Pt d-states, see Figure 18).

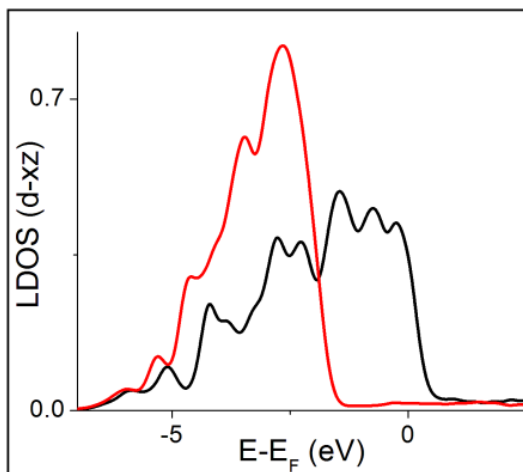


**Figure 18: d-xz LDOS comparison between Pt and Au slabs. Red line: d-xz states of the Au surface atom, black line: d-xz states of the Pt surface atom.**

### 3.4.3 Results on the system's reactivity towards the OH adsorption

In order to gain more insight into the factors controlling the surface reactivity and to test the idea of a major role of the hybridization in the reactivity of layered surfaces, the OH binding energies on Pt, Pt/Ru, Pt/Au, Pt-contr and Pt-expnd have been calculated. The results are listed in the Table 5, as well as the d-band center positions of the d-xy and d-xz states. Pt is used as reference for all the numbers. We find that, as suggested by the analysis of the projected Pt LDOS,  $E_B(\text{OH})$  is significantly lower for Pt/Ru(0001) than for Pt(111) due to the interlayer hybridization. These results are presented in Figure 19 where it can be seen that the correlation between the OH binding energy and the d-xz band center is clearer than the correlation between the OH binding energy and the d-xy or total d-band center (It is not the case for Pt/Au and we will come back to this system next). Therefore, we propose to relate the surface reactivity to the z oriented d-states rather than to the entire d-band[81].

**Table 5: Binding energies of OH on Pt, Pt-contr, Pt/Ru, Pt-expnd and Pt/Au systems and the d-band center change of Pt atoms on the surface of these systems. Pt is used as reference for all the numbers.**

	$\Delta E(\text{d-tot}), \text{eV}$	$\Delta E(\text{d-xy}), \text{eV}$	$\Delta E(\text{d-xz}), \text{eV}$	$\Delta E_B(\text{OH}), \text{eV}$
Pt(111)	0	0	0	0
Pt-contr	-0.12	-0.24	-0.05	-0.01
Pt/Ru	-0.37	-0.35	-0.37	-0.22
Pt-expnd	0.26	0.50	0.11	0.10
Pt/Au	0.58	0.69	0.49	0.08

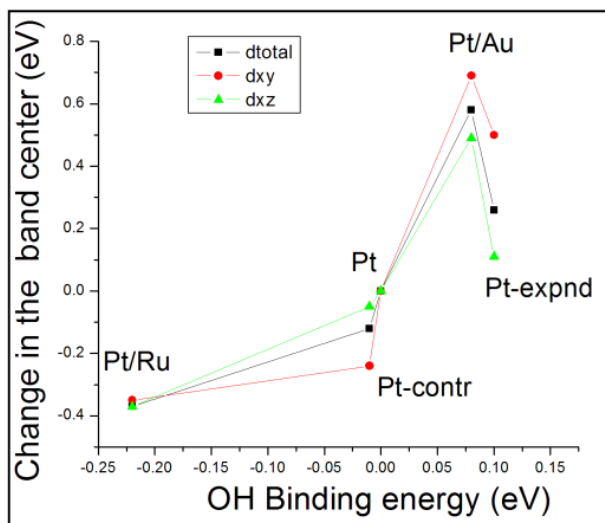


**Figure 19: Band centers changes (respect to Pt slab surface atoms) Vs OH binding energy for Pt/Ru, Pt-contr, Pt, Pt/Au, Pt-expnd. Black line: total d-band center, red line: d-xy band center, green line: d-xz band center.**

As we have mentioned above, the results for the OH binding energy on Pt/Au do not follow the d-band center or the proposed d-xz band center model, suggesting other contributions and mechanism involved on the OH binding energy for this particular system, other than the LDOS change. In all the systems under consideration, except for Pt/Au, the adsorption of OH does not alter the upper Pt monolayer configuration. In contrast, the OH adsorption on Pt/Au generates a surface reconstruction, as shown in Figure 20 (OH adsorbed on Pt/Ru has been included in the figure for comparison purposes, see panel **b** of Figure 20). This effect changes the system's electronic structure and cost extra energy, which results in a break in the correlation between the OH binding energy and the change in the LDOS, as shown in Figure 19 and Table 5.

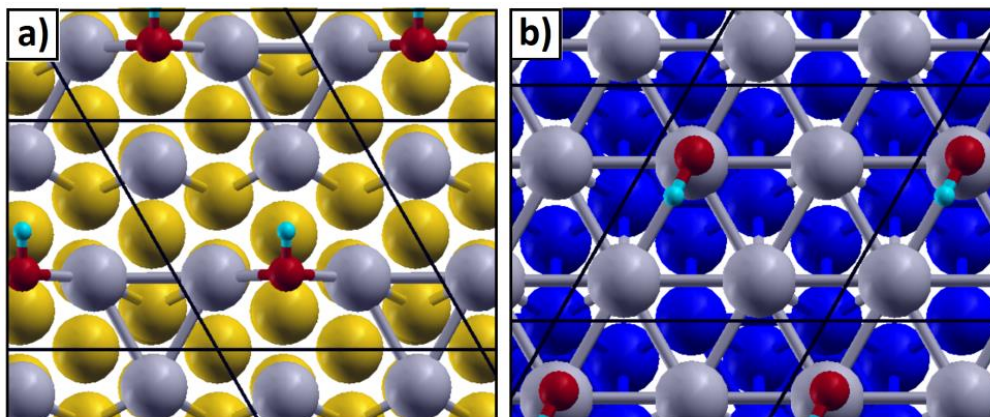


**Figure 20:** OH adsorbed on Pt/M surfaces. Panel a: M=Au, panel b: M=Ru. Grey, yellow, red, blue and light blue spheres denote Pt, Au, O, Ru and H atoms respectively.

The surface reconstruction upon adsorption is a well-known phenomenon that occurs when an adsorbate significantly changes the potential energy surface of the system[82]. To give an explanation of the observed surface reconstruction on Pt/Au, the Pt monolayer formation energy was calculated for all the systems under consideration. The results show that Pt binds weaker to Au than to Pt or Ru. More specifically, we found the Pt layer formation energy in Pt/Au is 0.464 eV/atom less than the Pt layer formation energy on Pt. On the other hand, the Pt layer formation energy in Pt/Ru is 0.632 eV/atom higher than the Pt layer formation energy on Pt. Therefore, since the Pt-Au bonds are weaker than the Pt-Pt bonds, and the Pt-Pt bonds have been elongated or expanded (due to the gold substrate in the Pt/Au system), the adsorption of OH induces the reduction of the Pt-Pt bonds distance, leading to the surface reconstruction. It is worth mentioning that to ensure that clean Pt/Au(111) does not undergo the reconstruction, the Pt/Au structure was relaxed starting from various perturbed configurations. In particular, it was started with the reconstructed Pt/Au configuration shown in Figure 20 panel **b**, but removing the

OH atoms. After relaxation the Pt-Pt bonds reached the original length found in our previous results for Pt/Au system, restoring the non-reconstructed surface geometry.

### **3.4.4 Conclusions**

In this project we have shown that the hybridization between layers is the main factor controlling the reactivity of the Pt monolayer/substrate systems, whereas contribution of the well-known strain effect to the reactivity is not significant. Also it was shown that since in-plane d-states are not actively involved in the adsorption process, the changes in the d-z LDOS are a better descriptor of the reactivity of the surface. Finally, it was found that for systems where the Pt monolayer is weakly bound to the substrate, reconstruction of the monolayer is likely to happen upon adsorption, destroying the correlation between the LDOS and the reactivity of the system.

## **3.5 First Principles Studies on Chalcogen Modified Ru Surfaces**

Ru catalytic properties towards the ORR are known to be inferior to the ones obtained with Pt. As we have mentioned above, the adsorption of O and OH are good descriptors of the catalytic activity towards the ORR and according to authors in [30] a reduction in the O and OH binding energy has to be made in order to improve the catalytic activity of Ru surfaces. In 1986 Alonso-Vante and Tributsch shown a high catalytic activity for  $\text{Mo}_{0.2}\text{Ru}_{1.8}\text{Se}_8$  systems comparable to Pt[83]. Since then, chalcogen modified Ru systems have attracted the attention of several groups, it has been shown by several experimental groups that the catalytic activity of Ru is enhanced by modifying the Ru system with Se[84, 85, 86, 87] up to a Se concentration of 15%

[86, 88]. For higher concentrations, the Se atoms block the active Ru nanoparticles sites reducing the catalytic activity of the system. The catalytic activity of Ru has also been enhanced with the addition of S and Te[84, 89, 90, 91] but to the extent of our knowledge, the reasons behind this enhancement have not been studied. Our previous work on Se modified Ru nano particles[92] and the author's work in ref[93] explains the ORR catalytic activity enhancement due to the electrostatic repulsion between the O and Se atoms on the surface, which leads to a weaker O adsorption.

Dassenoy and coworkers[97] have performed x ray diffraction (XRD) pattern experiments on the Ru nanoparticles modified with Se, finding that the particles maintain the hcp structure and are more resistant to oxidation than the Ru monometallic nanoparticles. Concerning the structure of the Ru nanoparticles, authors in ref[94, 99, 100] have performed x ray diffraction pattern experiments finding that the Ru nanoparticles maintain the hcp Ru core while the Se is coordinated at the surface of the nanoparticle. Zehl et al.[86] performed XRD experiments and were able to determine that the core of the Ru nanoparticle modified with Se had an hcp Ru core. Also the authors performed anomalous small-angle X-ray scattering experiments, their results allow them to suggest that the nearly spherical Ru nanoparticles with a mean diameter of 2.5 nm was decorated with small Se clusters with diameters less than 0.6 nm. Zaikovskii and coworkers[101] have synthesized similar Ru clusters modified with Se, they assume that the Ru nano particles are not decorated with Se island, but with Ru selenide clusters with sizes smaller than 1 nm. Concerning S and Te modified Ru clusters, Alonso-Vante et al.[90] performed extended X-Ray absorption fine structure (EXAFS) experiments on Ru nanoparticles modified

with chalcogens (S, Se and Te) and were able to determine that the particles have a Ru hcp core, while the chalcogens were coordinated outside the metal core.

In summary, Ru systems are known for having poor catalytic activity towards the ORR. However, it has been shown that its catalytic activity towards the ORR is improved by modifying the system with chalcogens (S, Se and Te). Experimental results have shown that the core of the Ru nano particle maintains a Ru hcp structure while the chalcogens are localized on the surface and first layers of the nano particles, still, to the extent of our knowledge there are no works in the literature explaining in detail this adsorption. In this section we will study in detail the chalcogen adsorption on flat Ru(0001) facets. Since it is known that the O and OH binding energies should be reduced in order to improve the catalytic activity of Ru systems, we will use these binding energies as descriptors of the ORR. The similarities and differences of the mechanisms enhancing the catalytic activity of Ru surfaces when modified with S, Se and Te will be discussed.

This section on Ru surface modified with chalcogens is organized as follows: in subsection 3.5.1 we give a description of the computational details. In sub section 3.5.2 we focus on the study of the chalcogen island formation and the redistribution of the valence charge density upon chalcogen adsorption. In 3.5.3 we show our results for O and OH coadsorbed with chalcogens, the results on the effect of chalcogens adsorption on the local density of states (LDOS) of the Ru surface atoms and finally in section 3.5.4 we present our conclusions.

### 3.5.1 Computational Details

According to experiments, chalcogen modified Ru nanoparticles have sizes ranging from 0.6 to 4 nm [89, 90, 91, 94]. Particles with these dimensions have flat facets on their surfaces, therefore we will model the Ru system using the (0001) facets, which is known to be the most stable.

For all the systems under consideration the electronic structure and the equilibrium position of the atoms were obtained using the code VASP 4.6[46], with projector augmented wave potentials[47] and the Perdew-Burke-Ernzerhof (PBE) version of the generalized gradient approximation (GGA) for the exchange and correlation functional[48]. we used a 3x3 in plane periodicity with 5 layers slab and a vacuum of 13 Å to simulate the surface. A (4x4x1) K point sampling in the Brillouin zone was used to obtain relaxed structures and energies, while a (7x7x1) sampling was used in DOS (density of states) calculations. A cutoff energy of 400 and 605 eV were used for the plane wave expansion of wave functions and charge density respectively. To achieve structural relaxation, a self-consistent electronic structure calculation was followed by calculation of the forces acting on each atom. Based on this information the atomic positions were optimized to obtain equilibrium geometric structures in which forces acting on atoms do not exceed 0.02 eV/Å.

In order to calculate the electronic charge corresponding to a particular atom in the system, a three dimensional surface around the atom is constructed, assigning the charge inside the surface to that particular atom. This surface has the particularity that is defined as the points

in space where the charge density reaches a minimum in the direction perpendicular to the surface. This is known as Bader analysis[95].

The valence charge redistribution upon X adsorption (X= O, S, Se or Te) was calculated using equation (3.10), the binding energy of the intermediates (O and OH) and the chalcogens (S, Se and Te) adsorbed on the surface was calculated using equation (3.9), while the formation energy per atom is defined as:

$$E_{for}(X) = \frac{n E(X) + E(slab) - E(X/slab)}{n}, \quad (3.16)$$

where the first term on the right hand side is the calculated DFT energy of a free (insolated) intermediate or chalcogen, the second term refers to the Ru slab's energy, the third term is the energy of the chalcogen or intermediate adsorbed on the Ru surface and finally  $n$  is the number of adsorbed atoms per supercell. It is important to note that a positive binding energy represents a binding between the intermediate/chalcogen and the surface.

Xcrysden software [49] was used to plot the atom positions, while the charge density figures in this paper were plotted using the Vesta software [96]

### **3.5.2 Results on Chalcogens Binding to the Ru Surface**

The chalcogen (O, S, Se and Te) binding energy to the Ru surface was calculated using equation (3.9), finding that the hcp is the preferred adsorption site with binding energies of 6.19, 5.87, 5.26 and 4.87 eV for O, S, Se and Te respectively. The chalcogen distribution over the Ru surface is an important aspect since it has profound effects on the O adsorption and as a consequence on the catalytic activity of the system. To the extent of our knowledge there has not

been a clear study concerning the chalcogen adsorption distribution on Ru surfaces. It is known[90] that the Ru particle maintain its Ru hcp core while the chalcogens stay near the surface. Some authors[86] have suggested a model where Se islands decorate the surface of the Ru particle, while others[97] have suggested a statistical distribution of the chalcogen (Se) over the surface. Our results for Ru clusters[92] and the author on Ref. [98] show that the Se island formation is not energetically favorable due to the electrostatic repulsion between Se atoms which acquire negative charge upon adsorption. To the extent of our knowledge these kind of analysis have not been performed for S or Te adsorption. Two cases will be considered in this section: a) chalcogen atoms adsorbed uniformly on the Ru surface and b) chalcogens atoms adsorbed as first neighbors, this will lead to the formation of dimers and trimers and we will refer to this case as island formation.

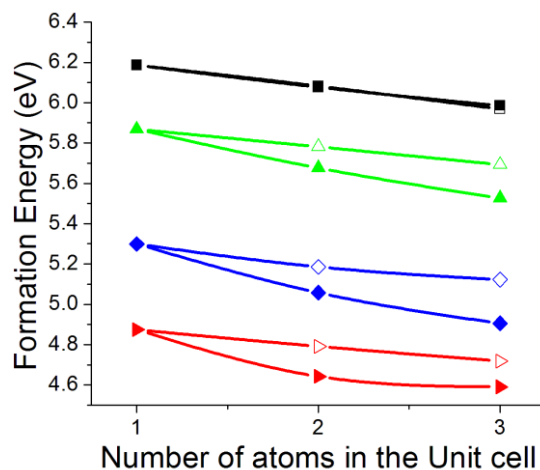


**Figure 21: Chalcogens formation energy. Hollow symbols denote uniform chalcogen adsorption and solid symbols denote island formation (dimer and trimer). Black, green, blue and red lines denote formation energy of O, S, Se and Te respectively.**

The formation energies corresponding to the island and uniform distribution of chalcogen over the Ru(0001) surface have been calculated using equation (3.16), the results are plotted in

Figure 21. It is important to note that the formation energy, for island and uniform distribution, decreases for all the chalcogens as the number of atoms in the unit cell increases, revealing an interaction between the adsorbed chalcogens in both cases. Furthermore and more important it is the fact that for all the chalcogens under consideration, except for O (we will address this issue at the end of this subsection), the uniform distribution over the surface is energetically preferred. In order to explain this behavior a Bader analysis was performed for the case of O, S, Se and Te adsorption (see Figure 22 panels **e**, **f**, **g** and **h**) showing an increment of 0.86, 0.47, 0.28 and a decrease of 0.02 electrons respectively, allowing us to conclude that the electrostatic repulsion between negatively charge O, S and Se atoms plays a major role in the decrease of the formation energy as the number of chalcogens in the supercell increases (see Figure 21), but does not allow us to draw any conclusion concerning the mechanisms controlling the Te adsorption or explain the behavior for the Te formation energy shown in Figure 21. It is interesting to compare the similarities of O adsorption on Ru and Pd surfaces, in both cases the O atom acquire negative charge. We would like to highlight the fact that the O binding energy reduction observed for O co-adsorbed with other O atom on Pd surfaces shown in Table 2, section 3.2, is due to this effect.

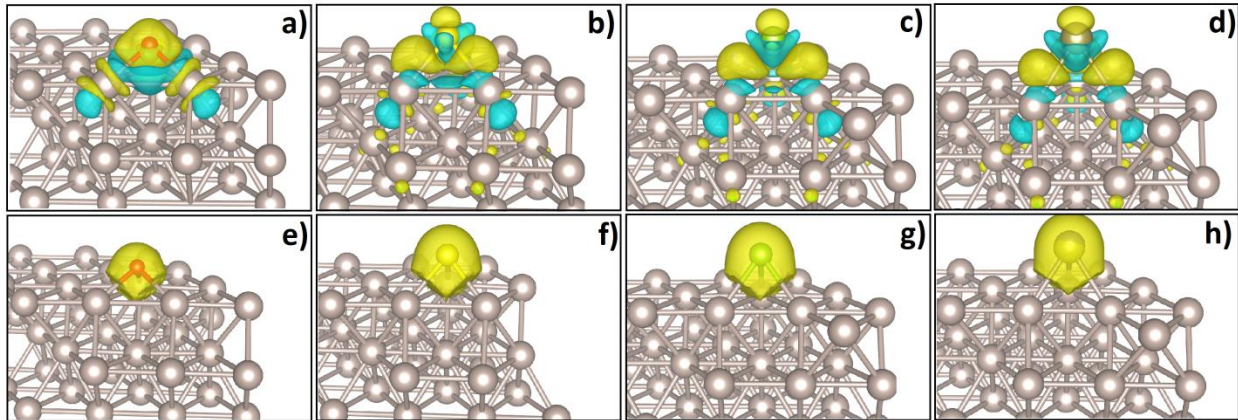


**Figure 22:** Upper panels: charge density redistribution upon chalcogen adsorption with isosurface set to  $\pm 0.024 \text{ e}/\text{\AA}^3$ , yellow and blue spots represent excess and depletion of charge respectively. Grey balls represents Ru atoms. Lower panels: total charge density volume used in the Bader analysis with isosurface set to  $0.3 \text{ e}/\text{\AA}^3$ . Panels a and e correspond to O adsorption, panels b and f corresponds to S adsorption, panels c and g corresponds to Se adsorption and panels d and h corresponds to Te adsorption.

We plotted in Figure 22 panels **a**, **b**, **c** and **d**, the valence charge density redistribution upon adsorption of the chalcogens under consideration (O, S, Se and Te). Panel **a** reveals the strong ionic character of the O-Ru bond, while panels **b**, **c** and **d** shows that for S, Se and Te, the character of the bond becomes more covalent as we go from S, through Se to Te. This is in good agreement with the Bader analysis previously discussed and confirms the electrostatic repulsion between negatively charged neighboring O, S and Se.

To get more insight into the nature of the chalcogen-Ru bond, in Figure 23 we plot the LDOS of the adsorbed chalcogens (p states) and Ru surface atom (d states). Panel **a** shows the deep energy localization of the O p states, which do not appreciable hybridize with the Ru d states, confirming the strong ionic character of the O-Ru bond. To evaluate the covalent contribution to the bonding, the percentage of non-occupied p states was calculated for each one of the chalcogens adsorbed on the surface finding an increase as we go from O to Te ( 17.21%,

18.76%, 20.92% and 22.97% in the case of O, S, Se and Te respectively), see panels **a**, **b**, **c** and **d** of Figure 23. This confirms the increasing covalent bonding of chalcogens when moving from S, through Se to Te.

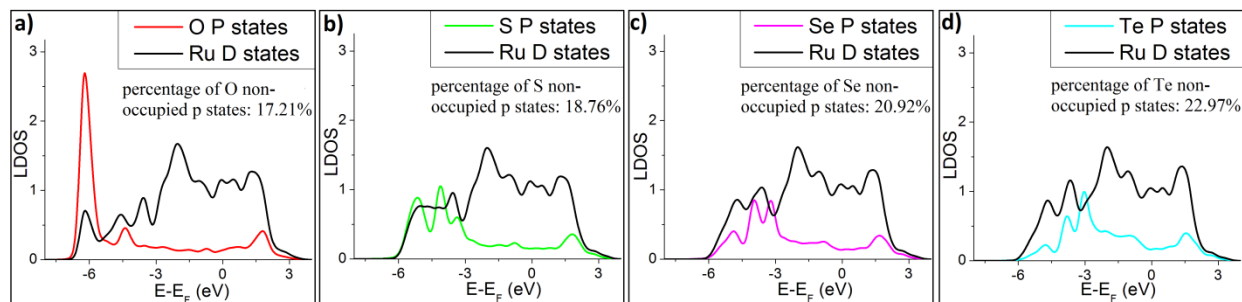


**Figure 23: LDOS for Ru Surface atoms and the adsorbed chalcogen atoms coordinated to the Ru atoms. Panel a: O adsorption, panel b: S adsorption, panel c: Se adsorption, panel d: Te adsorption. Black lines represent the d states of the surface Ru atoms coordinated to the chalcogen atom, while red, green, purple and blue lines denote O, S, Se and Te p states.**

To shine more light on the factors controlling the island formation energies depicted in Figure 21 and more precisely to understand the reduction of binding energy as the number of Te atoms in the island increases, in Figure 24, we show the charge density redistribution  $\Delta\rho$  upon adsorption of two chalcogen atoms (S and Te with the isosurface set to  $\pm 0.08 e/\text{\AA}^3$ ) adsorbed in neighboring hcp sites (dimer formation). Figure 24 Panel **a** shows  $\Delta\rho$  for of two co-adsorbed S atoms while panel **b** shows it for two co-adsorbed Te atoms. It can be seen that the charge coming almost entirely from the Ru atoms has been accumulate in the zone between the Ru atoms and the chalcogens. This accumulation of charge between the chalcogens (S or Te) and Ru electrostatically repels with neighboring S or Te accumulation of charge. Also in Figure 24 panel **a** and **b**, it can be seen a lower accumulation of charge at the bond with the common Ru (marked with red crosses in Figure 24), this is interpreted as a weaker covalent bond due to the higher coordination of this Ru atom. In conclusion: in the case of O, S and Se, an electrostatic repulsion

between chalcogens is observed due to the electrostatic charge gained upon adsorption. On the other hand, for all the chalcogens except for O (which has a high electronegativity and a strong ionic character in its bond with the Ru surface) a weaker covalent bond between the chalcogens and the Ru (the Ru bonded to neighboring chalcogens) is observed. These two effects are responsible for the reduction of the formation energy per atom with the increase of the number of atoms in the island as well as making a uniform chalcogen distribution on the Ru surface preferred over the chalcogen island formation.

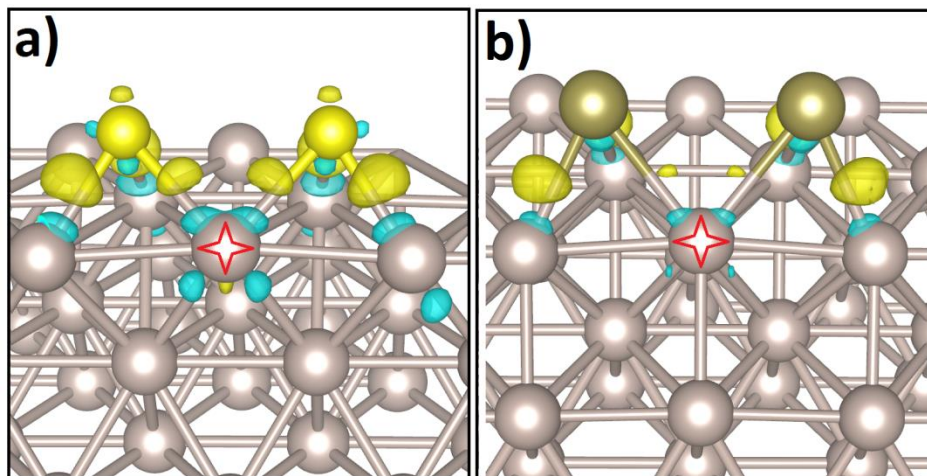


**Figure 24: Electronic charge density redistribution upon two chalcogens (S and Te) adsorbed on neighboring hcp sites. Red and blue spots denote accumulation and depletion of charge respectively. Iso-surface value is set to  $0.08 \text{ e}/\text{\AA}^3$ . Panel a: S atoms adsorption, panel b: Te atoms adsorption. Grey, yellow, and brown spheres denote Ru, S and Te atoms respectively.**

Now we will address the issue concerning the O formation energy for island formation and uniform distribution over the surface depicted in Figure 21, this is: the O island and uniform distribution formation energies adopt the same values. In other words, the distance between adsorbed O atoms does not affect the formation energy. This behavior may seem to contradict the previously discussed model where the electrostatic repulsion between negative charged

chalcogens (except for Te) atoms was suggested as one of the origin of the decrease in the formation energy as the number of atoms in the system increases and the cause of the uniform distribution preference over island formation. This behavior can be easily explained by comparing two scenarios: a) two O atoms adsorbed on the Ru(0001) surface as first neighbors (2.92 Å between O atoms) and b) two O atoms adsorbed as second neighbors (4.73 Å between O atoms). According to our Bader analysis, the amount of electronic charge gained by the O atom adsorbed as first and second neighbors in both cases is the same (around 0.8 electrons). On the other hand, the charge donated from the Ru surface atoms towards the O atoms is 0.22 electrons for all the cases except for the case of two O atoms adsorbed on the surface as first neighbors. In this case, the Ru atom coordinated to two O experiences a depletion of 0.42 electrons (all other Ru atoms coordinated to O atoms experience a depletion of 0.22 electrons) enhancing the ionic character of the O-Ru bond and the electrostatic attraction between this Ru and the O atoms. In summary, the increment in the electrostatic repulsion between O atoms caused by reducing the distance between them is compensated with the increase of the electrostatic attraction between the O atom and the doubled-coordinated Ru atom.

### 3.5.3 O and OH Binding Energy in Presence of Chalcogens

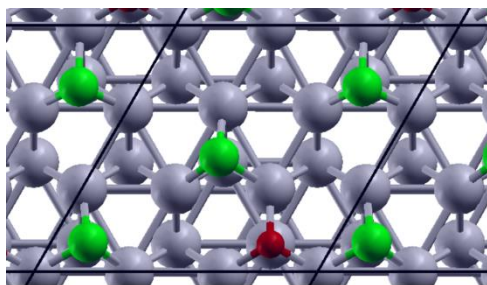


Figure 25: O adsorbed on the chalcogen modified Ru surface. Red, green and gray spheres denote O, chalcogens and Ru atoms. Black lines symbolize the Unit cell.

To evaluate the catalytic properties of Ru surfaces modified by different chalcogens, we will use the O and OH binding energy as a descriptor of the reactivity. As already mentioned in previous sections and discussed by other authors [30], the O and OH binding energies are good descriptors of the ORR. The O and OH binding energy were calculated on Ru surfaces with 1/3 chalcogen coverage (O, S or Te) and are presented in Table 6 (due to the dimensions of the unit cell, two nonequivalent adsorption sites are available for calculate the O binding energy. Table 6 shows the O and OH adsorption energy on the hcp site. Figure 25 provides a visual description of the adsorption geometry in the case of O adsorbed on the chalcogen modified Ru surface). As it can be seen, the O and OH binding energies are higher for the clean Ru(0001) surface, followed by the O, S, Se and Te modified Ru surfaces, with the Te modified surface the less reactive. This allows us to predict a catalytic activity of the chalcogen modified Ru surface in the following order: Ru +Te > Ru +S > Ru which is in good agreement with experimental results[91]. In Table 6, it is important to note that the O binding energy in the Ru surface with a 1/3 of O coverage is the highest (except for clean Ru). This is an interesting result because it tells us that the electrostatic repulsion is not the main factor contributing to the reduction of the O binding energy and the experimentally observed enhancement in the catalytic activity towards the ORR already mentioned on chalcogen modified Ru systems.

**Table 6: Binding energy of the intermediates, O and OH, on clean Ru and 1/3 chalcogen covered Ru surfaces.**

Surface \ Intermediate	Clean Ru	Ru + 1/3 O coverage	Ru +1/3 S coverage	Ru +1/3 Te coverage
O	6.187	5.695	5.372	5.177
OH	3.524	3.178	2.676	2.292

The reduction in the binding energy of the intermediates in the presence of chalcogens is due to two different effects: one is the electrostatic repulsion between the negatively charged O and chalcogen atoms (S and Se), or in the case of Te the redistribution of valence charge accumulated between Te and the surface Ru atoms. The second contribution to the decrease in the O binding energy is an indirect effect starting as a weakening of the bond between the chalcogen and Ru surface atom, due to the higher coordination of the Ru atoms making a bond with the O and chalcogen atoms. This causes a decrease in the total energy of the system and a decrease in the O binding energy in an indirect way, see equation (3.9). In Figure 26, panel **a** and **b**, we show the valence charge redistribution upon adsorption of (O and S) and (O and Te) respectively. The excess of charge around the O atom loses the symmetry exhibited in the panel **a** of Figure 22. This excess of charge is displaced away from the Ru atom making a bond with the O and the chalcogen (Ru atom marked with a red cross) due to the Coulomb repulsion with the excess of charge gain by the S atom upon adsorption (our Bader analysis shows an increase of 0.41 and 0.84 electrons in the valence charge of S and O respectively, for the configuration described in panel **a** of Figure 26) and the valence charge redistribution (covalent bonds) between Te and Ru atoms. The second effect can be easily seen in the lower valence charge density redistribution (which is understood as a weaker covalent bond) observed between the Ru atom marked with a red cross and the S or Te atom shown in Figure 26 panel **a** and **b** respectively. The valence charge density redistribution results for O and Se co-adsorption are not shown due to its high resemblance with the ones shown in Figure 26.

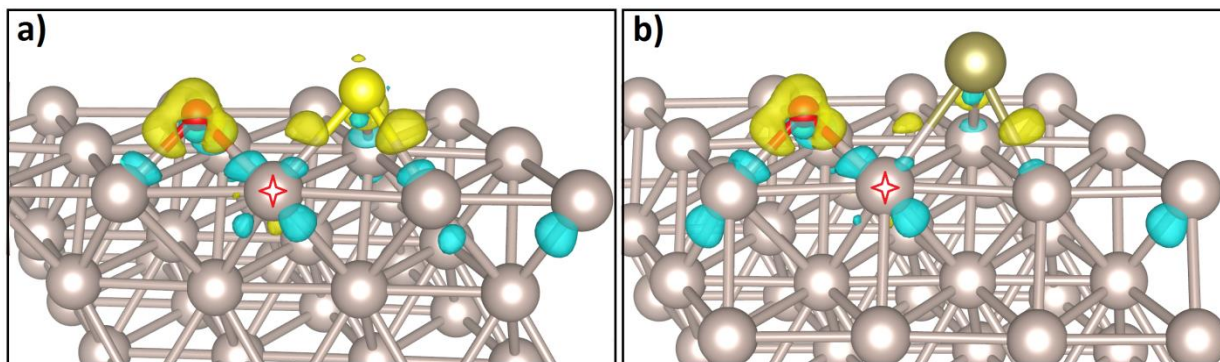


**Figure 26:** Valence charge density redistribution upon adsorption of O, S and Te, isosurface is set to  $0.08 \text{ e/\AA}^3$ . Panel **a**: O and S adsorbed in hcp neighbor sites, panel **b**: O and Te adsorbed in hcp neighbor sites. Yellow and blue spots denote excess and depletion of charge. Grey, red, yellow and brown balls denote Ru, O and S atoms.

To rule out the possibility of a reduction in the intermediates binding energy due to a change in the densities of electronic states of the Ru surface atoms with the adsorption of the chalcogens on the surface, in Figure 27, we present the d states of surface Ru atoms with and without one chalcogen as a first or second neighbor, see panel **a** and **b** respectively. The Table 7 presents the d-band center of the surface Ru atoms with one chalcogen as first neighbor. From Table 7 it can be seen that the change in the d-band center of Ru atoms with one chalcogen as first neighbor does not exceed 0.1 eV which may cause a slight effect on the O and OH binding energy. Figure 27 shows us that the change in the Ru d-states is very small for the Ru atoms with one chalcogen as first neighbor (panel **a**) and negligible for second neighbors (panel **b**), in other words it is a local effect. Therefore we conclude that the reduction in the binding energy of the intermediates and the enhanced catalytic activity of Ru with the addition of chalcogens (observed by other experimental groups) is due to the previously mentioned charge density redistribution upon adsorption of the chalcogens and not to a change in the Ru LDOS, as happen in other systems such as Pd-Co.

**Table 7: Ru surface atoms d-band center with one chalcogen as first neighbor**

System	d-band center (eV)
Clean Ru	-1.363
O as first neighbor	-1.468
S as first neighbor	-1.458
Te as first neighbor	-1.418

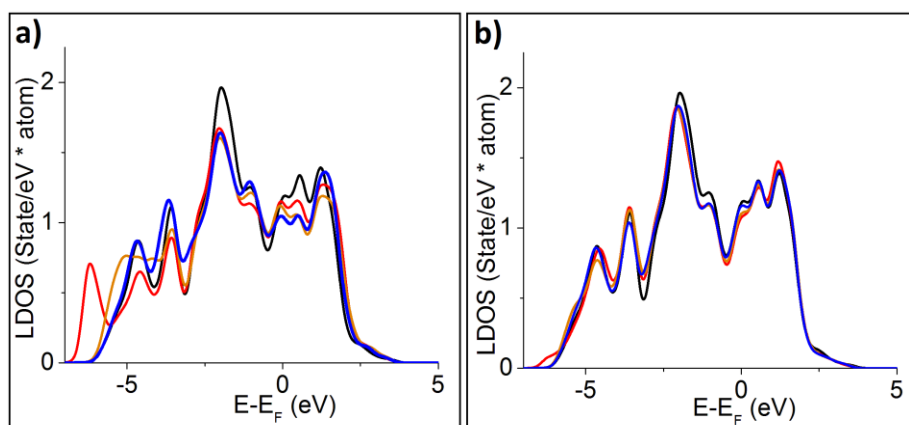


**Figure 27: Surface Ru atoms LDOS, panel a: chalcogens as first neighbors, panel b: chalcogens as second neighbors. Black lines denote Ru atoms with no chalcogen neighbors, while red, orange and blue lines denote Ru atoms with O, S and Te atoms as first or second neighbors respectively.**

### 3.5.4 Conclusions

Our results show that the chalcogen island formation is not energetically favorable due to two reasons: in the case of O, S and Se, electrostatic repulsion between chalcogens is observed due to the charge gained upon the chalcogen adsorption. On the other hand, for all the chalcogens, except O (which has a high electronegativity and a strong ionic character in its bond with the Ru surface) a weaker covalent bond between the chalcogens and the Ru (the Ru bonded to neighboring chalcogens) is observed.

For the ORR intermediates adsorption, we found that the O and OH binding energy are reduced by the presence of co-adsorbed chalcogens, making the O binding energy the lowest for

the Te modified Ru surface. Two mechanisms have been found to be responsible for this O and OH binding energy reduction: the first one is the electrostatic repulsion between negative charged chalcogen atoms (S and Se) and the intermediates (O and OH), while the second mechanism is an indirect effect where the chalcogen covalent bond with the surface is weakened due to the higher coordination of the Ru atoms making a bond with the O and chalcogen atoms.

Finally we found that the small change in the d-band center and LDOS of Ru surface atom caused by chalcogen atoms adsorbed on the surface is negligible and is not responsible for the enhancement in the catalytic activity observed in experiments.

### **3.6 First Principle Studies of the Size and Shape Effects on the Reactivity of the Se Modified Ru Nanoparticles**

In the previous section we focused on chalcogen (S, Se, Te) modified Ru surface (0001), briefly mentioning the effect of Se on the catalytic activity towards the ORR in Ru surfaces and doing special emphasis on S and Te. In this section we will focus on Se modified Ru systems. More precisely, we study the Se adoption on small Ru nanoparticles and the effect of Se on the O and OH binding energy, which are good descriptors of the ORR.

This section starts by highlighting the recent studies showing the enhancement in the electro-catalytic performance achieved with the  $\text{Ru}_x\text{Se}_y$  nanoparticles [94, 99, 100, 101, 102, 103, 104, 105, 106] . The main conclusions drawn from these works are: a) the best catalytic activity is achieved for the few nanometer particles with the Ru core covered with Se at composition  $\text{Ru}_{85}\text{Se}_{15}$ , b) these systems have an excellent tolerance to the methanol oxidation, c)

the systems have high selectivity for the four-electron oxygen reduction to water (small fraction of  $\text{H}_2\text{O}_2$ ), d) the systems exhibit a high stability towards oxidation, e) the Ru core has the bulk-like hcp structure and f) it is not clear how Se is distributed over the Ru particle surface. In the previous section we showed that the chalcogens, except Te, accept electronic charge coming from the Ru atoms, causing an electrostatic repulsion between neighboring Se atoms. The experimental data using the nuclear magnetic resonance and X-ray photoelectron spectra also suggest the electron charge transfer from Ru to Se [107]. As a result, Se atoms tend to scatter over the surface rather than from 2D islands or 3D structures [98, 108].

The properties of Se modified Ru systems have been extensively studied [109]. It is well known, as we previously showed, that in Ru flat facets (0001) the Se atoms accept charge from the Ru surface atoms causing an electrostatic repulsion between neighboring Se atoms. On the other hand, the author of Ref. [93] has shown that the electrostatic repulsion between O and Se atoms is responsible for the reduction of the O and OH binding and the enhancement in the catalytic activity towards the ORR in Se modified Ru nanoparticles. However, these results were obtained for a selenium modified Ru(0001) surface and it still needs to be understood how the geometry of small Se/Ru nanoparticles affects this mechanism, which, to the extent of our knowledge, has not been done.

In the present section we address the questions raised above. We obtain from first principles calculations the formation energies of the Se sub-monolayers on Ru nano-particles as a function of the Se coverage, as well as oxygen binding energies for different configurations of Se on the Ru particles. The calculations have been performed for two Se/Ru particles of  $\sim 1.2$  nm

size and different geometries. Such a choice allows us to study in details the effects of under-coordinated Ru sites on the energetics of Se and O adsorption and the electronic structure of the system. Our comparison of the results to those obtained for the flat Ru(0001) surface provides a clear suggestion of what energetics and electronic structure one can expect for the 2 nm – 5 nm particles, which have been observed in experiment and whose systematic first principles studies are still not feasible

### **3.6.1 Computational Details**

In this work we study the Se/Ru particles with 105 and 93 Ru atom core. The 93 Ru atom particles exhibit relatively large facets, while the 105 Ru atom particle exhibit under-coordinated adsorption sites.

All calculations in this work have been performed using the VASP5.2 code [46] with projector augmented wave potentials [47] and the Perdew - Burke - Ernzerhof (PBE) version of the generalized gradient approximation (GGA) for the exchange and correlation functional [48]. In order to simulate an insulated nanoparticle and maintain the periodicity, the nanoparticles were situated in a cubic unit cell of side 24 Å.

Since no dispersion of the electronic states occurs in such systems, the calculations were performed only for  $\Gamma$  point of the Brillouin zone, as it is usually done for non-periodic systems modeled by a periodic computational method. The cut of energies of 400 eV and 600 eV were used for the plane wave expansion of wave functions and charge density, respectively. To achieve structural relaxation, the atomic positions were optimized to obtain equilibrium geometric structures in which forces acting on atoms do not exceed 0.02 eV/Å.

Xcrysden software ref[49] was used to plot the atoms positions, while the charge density figures in this paper were plotted using the Vesta software [96]

### 3.6.2 Geometry and General Results on the Ru Nanoparticles

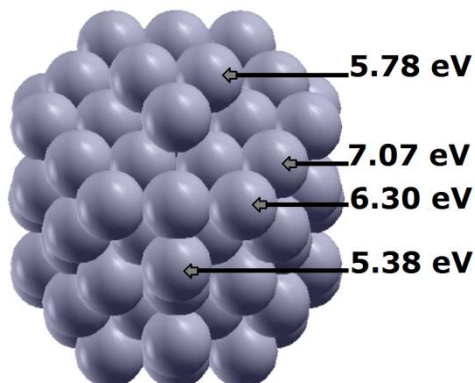


**Figure 28: Optimized geometric structure of the 105-atom Ru cluster. The inserted numbers provide the binding energies for some Ru atoms**

The two Ru cluster systems (93 and 105 atoms) under consideration are very similar, the optimized shape of the 105-atoms cluster is shown in Figure 28. The initial shape of the Ru cluster was chosen as a spherical cut of the hcp bulk. To avoid unphysical force cancelations between atoms (due to the symmetry of the system) all the atoms were randomly moved by 0.02 Å before performing the relaxation of the system. We found that the relaxed system maintains the hcp structure although some of the bond lengths deviate from the hcp Ru bulk. We realized that the relaxed structures of the clusters may not represent the lowest energy configuration. However, we consider them rather as prototype systems whose geometries include under-coordinated Ru atoms, which are typical for clusters of this size. The 105-atoms Ru cluster is comprised of a central Ru atom, two complete shells and twelve under-coordinated atoms. The twelve under-coordinated atoms are comprised of three Ru atoms on top and three Ru atoms

below the cluster with binding energies of 5.78 eV, while the remaining six Ru atoms are localized on the sides of the cluster with binding energy of 5.38 eV (see Figure 28). The Ru 93-atoms cluster looks like the 105-atoms Ru cluster without the twelve under-coordinated atoms. As it can be seen from Figure 28, the binding energy of Ru atoms to the cluster depends on the local geometry and, in particular, on the coordination numbers. Nevertheless, all surface Ru atoms bind to the cluster strongly enough to ensure its stability. For comparison, the binding energy of a Ru adatom on Ru(0001) is 5.804 eV.

### **3.6.3 Results on the Se Formation Energy and Adsorption on the Ru Nano-Cluster**

In order to understand the mechanisms controlling the Se adsorption on the Ru cluster, four different Se/Ru structures were taken under consideration (see Figure 29), where 1, 18, 30 and 42 Se atoms are evenly distributed over the Ru 105-atoms cluster, which approximately corresponds to 1.6%, 30%, 50% and 65% Se coverage respectively. The results on the relaxed Se/Ru systems show an expansion of the Ru-core caused by the Se atoms adsorbed on the surface. If we define the expansion of the cluster as the average distance of a given shell to the central atom in the Ru cluster, the under-coordinated Ru surface atoms expand by 0.127, 0.144 and 0.180 Å upon adsorption of 18, 30 and 40 Se atoms respectively. While the complete outer shell expands only by 0.019, 0.027 and 0.065 Å for these adsorption configurations.

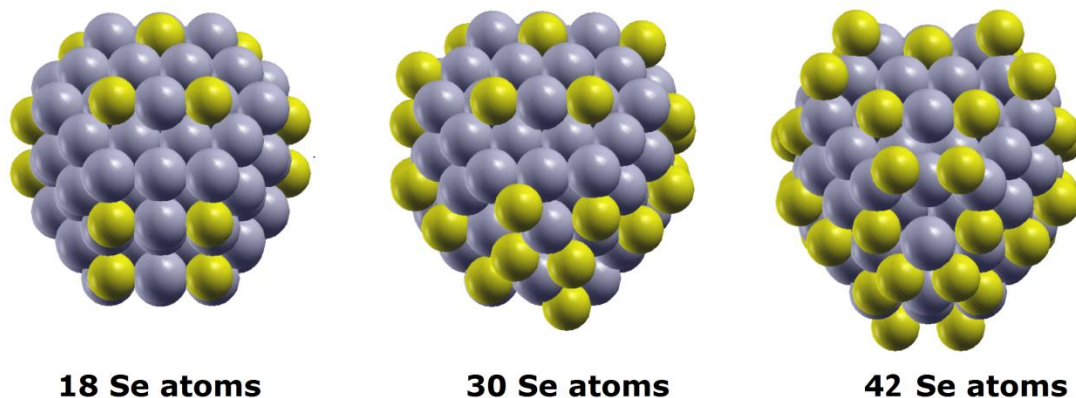


**Figure 29: Relaxed Se/Ru system for 30, 50 and 65% Se coverage over the Ru 105-atoms cluster.**

Using equation (3.16) the Se formation energy was calculated for the four different Se coverages under consideration (1.6, 30, 50 and 65%) on the Ru 105-atoms system. These results are shown in Figure 30 where the formation energy for uniform Se coverage over the Ru (0001) surface has been included for comparative purposes. As seen from the figure, the Se formation energy decreases with the increase in the Se coverage. The coverage dependence of the Se formation energy is found to be similar to that obtained for Se on Ru(0001), however the absolute values of the Se formation energy are higher on the Ru cluster than on Ru(0001), that is due to the higher reactivity of the under-coordinated atoms in the Ru clusters, which are not present in the Ru(0001) surface. A Bader analysis shows that the Se atoms accept 0.44, 0.33 and 0.26 electrons in average for the Se/Ru case of 1.6, 30 and 50% Se coverage respectively. This charge transfer is higher than the charge accepted by a Se atom on flat Ru(0001) facets reported in the previous section (an increment of 0.28 electron was found for Se atoms adsorbed on Ru(0001) surface), confirming a stronger ionic character in the Ru-Se bond in the Ru clusters. The reduction in the amount of charge accepted by the Se atom as the Se coverage increases has its origin in the increment of the Ru-Se bonds of the surface Ru surface atoms.

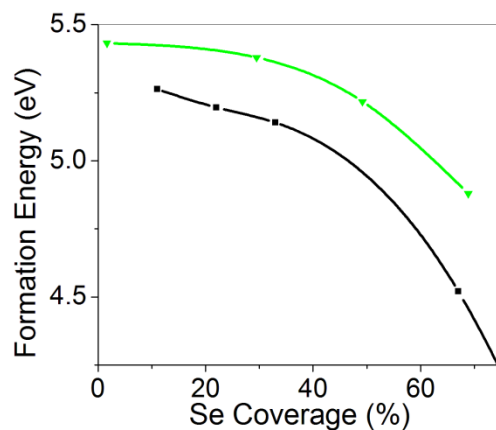


**Figure 30: Se formation energy as a function of the Se coverage. Green line: Ru 105-atoms cluster, black line: Ru(0001) facet.**

The reduction in the formation energy as the Se coverage increases in the Ru cluster has its origin in two different effects: a) the already mentioned reduction of the charge accepted by Se atoms (which is interpreted as a weakening of the ionic bond character) as the Se coverage increases and b) the electrostatic repulsion between charged Se atoms.

To understand the similarities and differences between Se adsorption on the flat Ru(0001) surface and the Ru cluster, we calculated the valence charge density redistribution upon adsorption of two Se atoms on a flat(0001) facet of the Ru 93-atom cluster and around an apex of the Ru 105-atom cluster. Figure 31, panel **a**, shows a strong Se-Ru covalent bond. On the other hand, a Bader analysis of the situation depicted on panel **a** of Figure 31 shows an increase of 0.2 electrons in the adsorbed Se electronic charge, revealing a strong ionic component of the bond (not revealed in the charge density redistribution). As can be seen, these results are qualitative similar to the ones obtained in the previous section for the chalcogen adsorption on Ru(0001) facets (see Figure 22 and Figure 24). In summary, the electrostatic repulsion between adsorbed Se atoms plays a major role in the Se formation energy reduction as the Se coverage increases.

However, if Se atoms are adsorbed around an under-coordinated Ru apex, the character of the Se–Ru bonding is found to be more complicated: in panel **b** of Figure 31 it can be seen a lower accumulation of charge between the Se-Ru bond than the one seen in panel **a**, suggesting a weaker covalent character in the Se-Ru bond when Se atoms make a bond with under-coordinated Ru atoms. On the other hand, a Bader analysis shows an increase of 0.32 electrons in the electronic charge of the Se atoms at the apex (0.12 electrons more than the charge gained by Se in the configuration depicted in panel **a** of Figure 31), revealing a stronger ionic bond. Furthermore, under-coordinated atoms are very reactive towards the Se adsorption and are able to screen the repulsion between electronegatively charged Ru atoms. Therefore we expect to see the formation of small Se islands around the under-coordinated Ru atoms, while a uniform distribution of Se atoms is expected in large flat Ru facets due to the electrostatic repulsion between Se atoms.

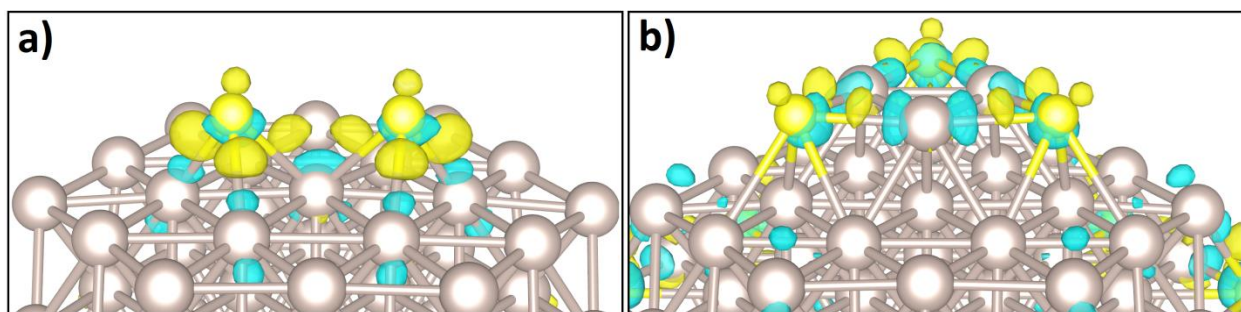


**Figure 31:** Valence charge density redistribution upon Se adsorption on Ru 93- and Ru 105-atom clusters cluster. Yellow spots denote excess of charge, while blue spots denote depletion of charge. Panel a: Two Se atoms adsorbed on a flat facet of the Ru 93-atom cluster, panels b: Se adsorption around the apex of the Ru 105-atom cluster. The isosurface was set to  $\pm 0.06 e/\text{\AA}^3$ . Grey and yellow spheres denote Ru and Se atoms respectively.

The LDOS of two Ru atoms atom with coordination numbers 9 and 5 (corresponding to a Ru atom in the flat facet of the Ru 93-atoms cluster and a second Ru atom in the apex of the Ru

105-atoms cluster) with and without Se atoms as first neighbors were calculated. These results are presented in Figure 32. As can be seen in panel **a**, the Se atom causes a negligible effect on the LDOS of the high-coordinated Ru atoms (the d-band center is shifted only by 0.033 eV toward the Fermi-level), while the Se adsorbed around the Ru apex (Figure 32 panel **b**) causes widening of the Ru d-band and a negative shift of the d-band center by 0.106 eV due to hybridization between the Se p-states and Ru d-states, which is not large enough to cause a noticeable effect on the reactivity of the system associated to the distribution of Se atoms on Ru nanoparticles.

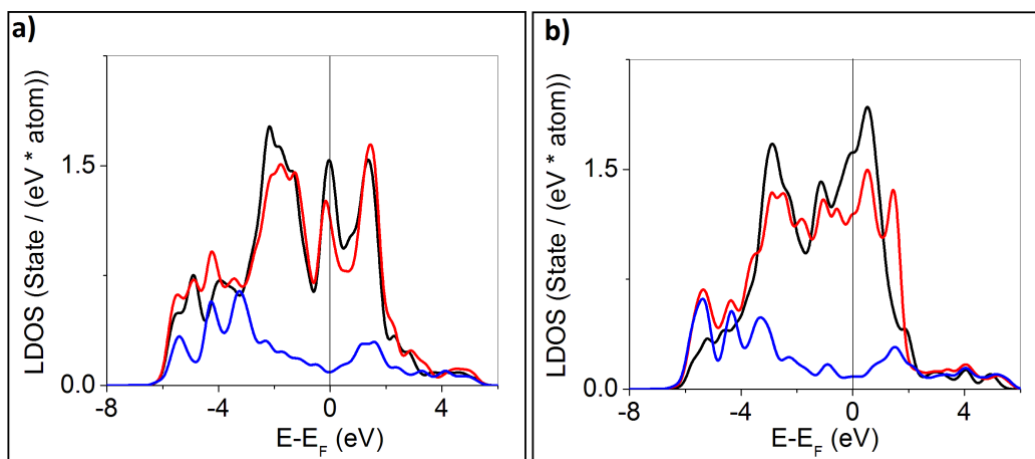


**Figure 32:** LDOS calculated for Ru atoms with and without Se bonded as first neighbors. Panel **a**: Ru atom in flat facet of the Ru 93-atom cluster, panel **b**: Ru atom belonging to the apex of the Ru 105-atom cluster. The black and red lines represent the densities of the Ru d-states calculated for the clean and Se-adsorbed clusters respectively, while the blue lines represent the Se p-states.

### 3.6.4 Results on the Oxygen Adsorption on the Se Modified Ru Nano-Cluster

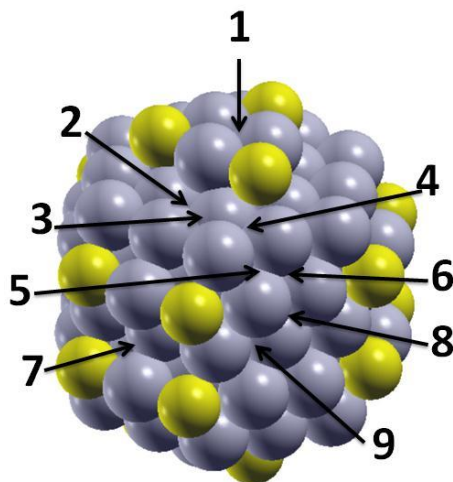


Figure 33: Oxygen adsorption sites on the Ru and Se/Ru 105-atom cluster.

As we have mentioned in chapter 1, the O and OH binding energies are good descriptors of the ORR, in particular the O binding energy (due to the linear relation between O and OH binding energies[31]). Also it has been shown that in order to improve the catalytic activity of Ru systems, towards the ORR, the O and OH binding energies have to be reduced[30]. With this being said, we calculate the O binding energy for nine different non-equivalent adsorption sites of the clean Ru 105-atom core and on the core pre-adsorbed with eighteen Se atoms (see Figure 33), which corresponds to about 30% Se coverage. These results are listed in Table 8, it can be seen that for the clean Ru core the O binding energies range from 5.71–6.53 eV, which is determined by a variety of local geometries including the coordination number of Ru atoms and number of O–Ru bonds. For example, the highest O binding energy values are obtained for the adsorption sites #1 and #5, for which O makes three bonds with under-coordinated Ru atoms, while oxygen adsorption on the sites #2 and #3 with higher-coordinated Ru atoms results in the

lowest O binding energies. It is important to note that, in general, the Ru 105-cluster is found to be more reactive than the Ru(0001) surface, for which the O binding energy is 6.18 eV (see Table 6). On the other hand, the presence of Se reduces the O binding energy, that is found to be in the range 5.24–6.10 eV. Furthermore, is important to notice the correlation between the O binding energies on the Se modified Ru cluster and the number of neighbor Se atoms and its distances to the O atoms. For example, the presence of three neighboring Se decreases the O binding energy at the #1 site by 1.26 eV, while one Se neighbor of approximately the same O–Se distance (site #3) causes a O binding energy reduction of only 0.36 eV. On the other hand, one Se neighbor, located closer to the O, reduces O binding energy at the #4 site by 0.87 eV.

**Table 8: Se effects on oxygen adsorption on the Ru nanoparticle.**

Adsorption Site	# of O-Ru bonds	O-Ru bonds lengths (Å)	# of Se neighbors	Distance to Se atoms (Å)	$E_B(O)$ on clean Ru cluster (eV)	$E_B(O)$ on Se/Ru cluster (eV)
1	3	2.10	3	3.26	6.53	5.27
2	2	1.91/2.08	2	3.41	5.91	5.39
3	3	2.03	1	3.23	5.95	5.59
4	2	1.98	1	2.91	6.47	5.60
5	3	2.05	1	3.58	6.53	6.00
6	3	2.04	2	4.40	6.21	6.10
7	3	1.98/2.16	4	3.42	5.71	5.24
8	3	2.04	2	4.40	6.30	5.97
9	3	2.07	1	3.61	6.29	5.64

Now, comparing the O binding energies on the Se/Ru cluster to the ones obtained by the author on [93] for flat Se/Ru(0001) facets, it can be seen that in general the Se/Ru cluster binds the O atoms stronger than the flat Se/Ru(0001) structure. This effect is due to the under-coordinated and thus more reactive Ru atoms towards the O adsorption. Therefore we can

conclude that large Se/Ru nanoparticles with well-developed flat facets are more favorable for the ORR than small Se/Ru clusters.

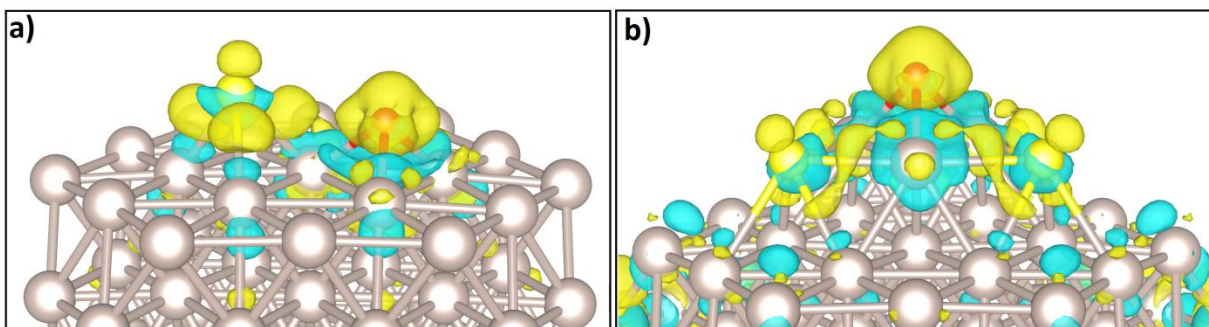


**Figure 34: Electronic charge density redistribution upon Se and O adsorption on Ru clusters, isosurface was set to  $0.04 e/\text{\AA}^3$ . Panel a: Ru 93-atoms cluster, panel b: Ru 105-atoms cluster. Yellow and blue spots denote excess and depletion of charge respectively. Grey, red and yellow spheres denote Ru, O and Se atoms respectively.**

In order to trace the obtained Se effect on the O binding energy to the electronic structure of the system, we go back to Figure 32 panel **a**, where it can be seen that for high-coordinated Ru atoms the change in the LDOS due to Se adsorption is negligible and it is not possible to attribute the reduction of the O binding energy. In the same way, in the previous section we have shown that for flat Ru(0001) facets the effect of Te and S on the LDOS of the Ru atoms is negligible. Figure 32 panel **b** shows a small change in the d band center (0.106 eV shift towards negative values) of under-coordinated atoms belonging to the apex of the Ru 105-atom cluster, that may lead to the above mentioned significant reduction in the binding energy of oxygen adsorbed on the apex top, see Table 8 adsorption site #1.

For further understanding of the nature of the Se effect on oxygen bonding to Ru, we analyze the charge density redistribution upon Se and O adsorption on the Ru cluster. As shown in Figure 34 panel **a**, when Se and O are adsorbed on a flat(0001) facet of the Ru 93-atoms

cluster, the O accepts a significant amount of electronic charge coming from the Ru atoms, while the character of the Se-Ru bond has a higher covalent component. A Bader analysis on the O and Se adsorption shows an increase of 0.20 and 0.81 electrons in the electronic charge of the O and Se atom respectively, confirming the already mentioned ionic character of the O bond and revealing an important ionic character of the Se-Ru bond, not observed on the Figure 34.

The reduction in the O binding energy has two contribution analogues to the ones already discussed in the previous chapter, these are: a) the electrostatic repulsion between O and Se atoms due to the electronic charge accepted by the atoms upon adsorption; b) an indirect effect of weakening of bond between the chalcogen and Ru surface atoms, due to the higher coordination of the Ru atoms making a bond with the O and chalcogen atoms. This causes a decrease in the total energy of the system and reduction in the O binding energy in an indirect way, see equation (3.9). In summary, the charge density redistribution for chalcogen adsorption on the flat facets of the Ru 93-atoms nanoparticle is found to be similar to that shown in the previous section for chalcogens adsorption on Ru(0001). For the O adsorption on the apex of the Ru 105-atom depicted in Figure 34 panel **b**, the analysis and conclusions are completely analogous to the one mentioned above, with the difference that the Bader analysis shows a slightly increase of 0.1 electrons in the charge gained by the Se (this is due to the low coordination of the Ru atoms comprising the apex).

### **3.6.5 Conclusions**

The results and analysis performed in this section show that small Se/Ru particles are not favorable for the ORR due to the under-coordinated Ru atoms presents in such structures, which

are very reactive towards the O adsorption. We thus conclude that the activity of Se/Ru catalyst toward the ORR can be improved by synthesizing the material in the form of relatively large nanoparticles (larger than 4–5 nm) with well-developed Ru(0001) facets.

We have shown that the Se island formation in the flat facets of Ru nanoparticles is not energetically favorable due to the electrostatic repulsion between Se atoms. While under-coordinated Ru atoms may cause the formation of small Se islands around them, due to the high reactivity of the under-coordinated Ru atoms towards Se adsorption and the capability to screen the electrostatic repulsion between negative charged neighboring Se atoms.

## CHAPTER 4: FIRST PRINCIPLES CALCULATIONS ON PHOTO-CATALYTIC SYSTEMS TOWARDS THE HYDROGEN EVOLUTION

### 4.1 Introduction

Photo-catalytic water splitting is a promising means for clean production of hydrogen from a renewable source. The process is the following: when a photon strikes an electron in the valence band of the anode, the excited electron may occupy the conduction band, creating an electron-hole pair. If the Fermi level of the cathode is lower than the bottom of the conduction band of the anode, it is favorable for the electron to transfer to the conduction band of the cathode. Once two holes have been generated by two different photons and a difference in potential has been established between the two electrodes, due to the two excited electrons now in the cathode, the reaction continues as ordinary electrolysis. This is, the water is oxidized losing two protons,  $1/2O_2 + 2H^+$  (at the anode). Next these the two protons may travel towards the cathode, where they will be reduced to  $H_2$ . This reaction is depicted in equations (4.1) through (4.3).



where \* denotes the anode.

Although oxygen evolution was first reported by Boddy[7] in 1968, only after Fujishima and Honda [8] reported the photo-electro-chemical water splitting in 1972, various semiconductor materials started to be tested as photo-catalysts, as already mentioned in the introduction to this work. For example  $\text{TiO}_2$ , among others, have been widely studied. These materials have not been successfully implemented due to its wide band gap, which restricts the light absorption to the ultraviolet (UV) range, while the solar spectrum contains only the 4% of UV irradiation. Others materials such as CdS, with more suitable band gap width (2.4 eV), suffer from low stability in the reaction environment. Therefore, considerable effort has been made in searching for new stable materials that are photo-catalytically active under visible light irradiation [110, 111, 112].

In general, materials used as photo-anodes suffer from three main problems: a) the band gap is too wide in order to efficiently use solar radiation, b) once the electron-hole pair is generated, low carrier mobility promotes the recombination of the electron hole pair and c) the top of the valence band is not lower than the  $\text{O}_2/\text{H}_2\text{O}$  potential making the water oxidation unfavorable. In this work, we will focus on the electronic structure and the band gap of the anode, and how its width can be tuned to desirable values by doping the semiconductor with different elements.

#### **4.2 Doping Effects on the Electronic and Geometric Structure of Graphitic $\text{C}_3\text{N}_4$**

As mentioned in the introduction to this chapter, several materials have been studied as possible candidates to be implemented as the photo-catalytic anode. In this work, we studied the

properties of the graphitic carbon nitride (g-C<sub>3</sub>N<sub>4</sub>), which is a promising photo-catalytic material and it has been subject of several studies[113,114, 115, 116, 117, 118]. Among its properties, three are important to highlight: 1) it is a metal free layered material with a 2.7 eV band gap, which means is able to absorb blue light with wavelength up to 450 nm, 2) the H<sup>+</sup>/H<sub>2</sub> reduction and O<sub>2</sub>/H<sub>2</sub>O oxidation potentials are situated within the band gap and 3) it is the most stable allotrope of carbon nitrides at ambient conditions, comprised of abundant elements.

The g-C<sub>3</sub>N<sub>4</sub> photo-catalytic properties can be improved by resolving the following issues: 1) the top of the valence band is too close to the O<sub>2</sub>/H<sub>2</sub>O oxidation potential lowering the ability to oxidize water, 2) the absence of interlayer hybridization of the electronic states restricts the carrier mobility, making the electron hole recombination more likely to happen and 3) the band gap is still too wide for optimal use of solar energy.

The above mentioned issues have been extensively studied and several attempts have been made to solve these problems, mainly, by doping or altering the system. For example, other authors have tried to dope the material with B[119], C self doping[120], O[121], P[122], S[123], CdS[124], Fe[125] and Ag[126] among others. It has been reported that doping causes important changes in the g-C<sub>3</sub>N<sub>4</sub> electronic structure and its photo-catalytic activity. For example the authors in ref[121] have reported a 0.21 eV reduction in the band gap of the system when the system is doped with O, the authors in ref[122] found that the system acquires a metallic character with P doping, while the authors in ref[119] reported a negligible decrease of 0.04 eV in the band gap with B doping and a dependence of the band gap on the sample fabrication temperature.

In this work we study and systematically analyze the changes in the electronic structure of  $g\text{-C}_3\text{N}_4$  caused by the introduction of B, C (C self doping), N (N self doping), O, P and Si atoms into the  $g\text{-C}_3\text{N}_4$  system. Si and P were chosen as dopants because these elements contain the same number of valence electrons as C and N respectively, B has one valence electron less than C, while O contains one valence electron more than N. Therefore these elements are expected to be good candidates to replace N or C atom, by slightly altering the band gap without destroying the electronic structure of the system. To the extent of our knowledge, there are no studies in the literature explaining factors controlling the mentioned doping effects, except for our previous work on S doped  $g\text{-C}_3\text{N}_4$  systems[127].

This section starts by giving a short description of the computational details; in subsection 4.2.2 we will study the formation energy of the doped systems and the energy barriers involved in the N replacement; on subsection 4.2.3, 4.2.4 and 4.2.5 we make an analysis of the doping effects on the  $g\text{-C}_3\text{N}_4$  system's band gap and finally the conclusions can be found on section 4.2.6.

#### **4.2.1 Computational Details**

To study the doping effects of  $g\text{-C}_3\text{N}_4$ , two systems were considered: the first one with a (1x1) in-plane periodicity, consisting of 28 atoms (12 C and 16 N) with two layers per supercell, while the second system has a (2x1) in-plane periodicity and is comprised of 56 atoms (24 C and 32 N) with two layers per supercell.

For all systems under consideration, the energetics and equilibrium atomic configurations are obtained using the VASP5.2 code[46] with projector augmented wave potentials[47] and the

Perdew-Burke-Ernzerhof (PBE) version of the generalized gradient approximation (GGA) for the exchange and correlation functional[48]. A 750 eV cutoff energy for the plane wave expansion of the wave function was used, all atoms in the system were allow to relax until the forces acting on the atoms were smaller than 0.015 eV/A, For the k-point sampling in the Brillouin zone, we used a (5x5x5) and (3x6x5) (for the (1x1) and (2x1) supercell respectively) grid centered at the  $\Gamma$  point, that provided sufficient accuracy for the characteristics obtained by integration in reciprocal space. To take into account the Van der Waals interaction between layers the semi-empirical potential proposed by Grimme [128] was added, as implemented in the VASP5.2 code. Our calculations on the g-C<sub>3</sub>N<sub>4</sub> structure optimization shows a lattice constants a=b=7.14 Å, in excellent agreement with the experimental value of 7.13 Å [113]. On the other hand we found c=6.15, which is 7 % less than the experimental value [113, 116]. This error is attributed to the semi-empirical potential used to reproduce the Van der Waals interaction between layers.

Since it is well known that DFT poorly reproduces the band gap in semiconductors, the GW method in the G<sub>0</sub>W<sub>0</sub> approximation was used[26]. A cutoff energy of 90 eV was used for the response function, while 140 and 200 band were used (for the (1x1) and (2x1) supercell respectively) to calculate the dielectric matrix and the Green function. Using these parameters the calculated band gap for the pristine g-C<sub>3</sub>N<sub>4</sub> system is in good agreement with experiments, as it is shown in our previous work [127].

The Xcrysden[49] and the Vesta[96] software were used to plot the atom position, as well as the charge density redistributions.

The binding energies and the valence charge redistribution upon addition of an atom were calculated using equations (3.9) and (3.10) respectively, while the valence charge redistribution upon formation of the system was calculated using the following equation.

$$\delta\rho = \rho_{system}(r) - \sum \rho_{atoms}(r), \quad (4.4)$$

where the first term on the right hand side correspond to the valence charge density of the system under considerations, while the second term denotes the summation of the valence charge density of the insolated atoms comprising the system, at the position on the original system.

#### **4.2.2 Formation Energy and Geometry of the doped g-C<sub>3</sub>N<sub>4</sub> System**

There are two main configurations for the stacking of the layers in the g-C<sub>3</sub>N<sub>4</sub> system, these are: in the AA configuration, one layer lies perfectly on top of the other one. In the second one, AB configuration, one layer is displaced respect with the other by a certain distance giving rise to a family of AB stacking, depending on the displacement. We chose the minimum energy AB configuration according to our previous work [127].

Due to the nature of the AB stacking configuration, there are four nonequivalent C and N atoms, but due to the small hybridization between layers, we will only consider three and two nonequivalent N and C atoms respectively. These are: corner, middle and border N atoms and corner and middle C atoms (see Figure 35 panel **a**). Special cases of doping where hybridization between layers plays an important role will be discussed separately.

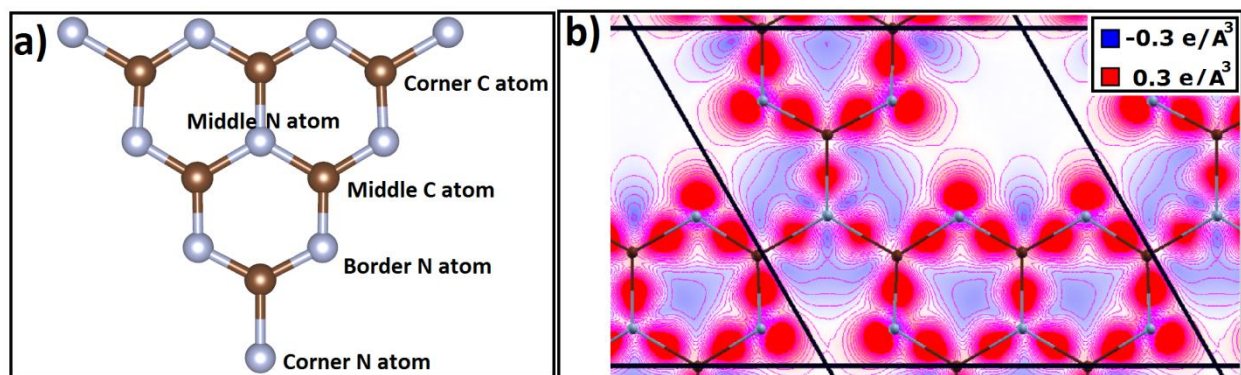


**Figure 35: G-C<sub>3</sub>N<sub>4</sub> structure. Panel a: Tri-s-triazine structure. Panel b: Valence charge density redistribution upon formation of the system, red and blue spots denotes accumulation and depletion of charge respectively.**

The valence charge density redistribution upon formation of g-C<sub>3</sub>N<sub>4</sub> was calculated using equation (4.1) and is plotted in Figure 35 panel **b**. As seen from panel **b** of Figure 35, the charge density redistribution reflects typical sp<sup>2</sup> hybridization between C and N atoms, while two dangling bonds belonging to the two border N atoms can also be seen in the plot (lone pairs). These dangling bonds are assumed to be the most reactive sites of the system where a third atom added to the system will prefer to bind. It is important to notice that a weaker covalent bond is formed between the corner C and N atom (represented as a lower accumulation of charge between the corner C and N atom, see panel **b** of Figure 35). This weak bond suggest that corner C atoms is be more likely to be replaced by the dopants than by middle C atoms, this will be confirmed later by our results.

As mentioned earlier, we studied the g-C<sub>3</sub>N<sub>4</sub> system doped with B, C, N O, Si and P. In each of these cases, three scenarios are possible: a) addition of the atom to the system (dopant binding to the dangling bonds), b) replacement of C atoms by dopants and c) replacement of N atoms by dopants. These cases where studied by defining the doping formation energy as:

$$F_E = E_{d-C_3N_4} - (E_{C_3N_4} + \mu_d - \mu_{replaced-a}), \quad (4.5)$$

where  $E_{d-C_3N_4}$  denotes the energy of the doped g-C<sub>3</sub>N<sub>4</sub> (DFT energies), the second term  $E_{C_3N_4}$  is the energy of the pristine g-C<sub>3</sub>N<sub>4</sub> system (DFT energies), the third term  $\mu_d$  is the chemical potential of the dopant atom added to the system, while  $\mu_{replaced-a}$  is the chemical potential of the replaced atom. In this formula we are not taking into account vibrational contribution since these makes a small contribution compared to the electronic parts [129]. It is important to note that the negative formation energy, in this case, denotes an energetically favorable reaction.

The chemical potentials  $\mu$  were calculated using the standard enthalpy of formation, the difference in entropy between atoms in gas phase and the corresponding species at 298.15 K listed in tables [130], as well as the DFT energies of the insolated atoms obtained by us. Concerning the chemical potentials of C and N, depending on the experimental conditions,  $\mu_C$  and  $\mu_N$  can change, taking the values between an upper and lower limit. The C-rich condition and the N-rich condition define the upper boundaries for the chemical potentials of C and N respectively. Under extreme C-rich condition, the chemical potential of C,  $\mu_C$ , is defined as  $\mu_C = \mu_{C[Bulk]}$ . For higher C chemical potentials we will be precipitating graphitic Carbon. In the same way, for N-rich condition, the N chemical potential,  $\mu_N$ , is defined as  $\mu_N = 1/2 \mu_{N_2}$ . These are the upper limits for the N and C chemical potentials. The lower limits will be defined using the following expression:

$$3\mu_C + 4\mu_N = \mu_{C_3N_4}, \quad (4.6)$$

where  $\mu_{C_3N_4}$  is approximated by the total energy per formula unit. In this way, the lower limit for the N chemical potential will be defined by:

$$\mu_{N[min]} = \frac{\mu_{C_3N_4} - 3\mu_{C[Bulk]}}{4}, \quad (4.7)$$

while the lower limit of the C chemical potential is defined as:

$$\mu_{C[min]} = \frac{\mu_{C_3N_4} - 4(1/2\mu_{N_2})}{3}, \quad (4.8)$$

The formation energies corresponding to the C-rich condition (upper and lower limit of the C and N chemical potentials respectively) and the N-rich condition (upper and lower limit of the N and C chemical potentials respectively) are presented in table in Tables 9, 10, 11, 12 and 13. These tables correspond to the doping formation energies of B, C and N, Si and P, respectively. From these tables it can be seen that the addition of atoms to the dangling bonds, in all the cases, results in higher formation energy than the substitution of C or N atoms. Our results show negative formation energies (energetically favorable) for the replacement of at least one nonequivalent N atom for each dopant, except for Si. This result was expected since, with the exception of O, N is the most electronegative atom, while Si is the less. Furthermore the big size of Si causes the system to experience a considerable in-plane lattice distortion, resulting in an increase in the formation energy (if no hybridization between layers occurs).

**Table 9: Formation energies for B doping at T=298.15 K**

	Formation energy in the C rich condition (eV)	Formation energy in the N rich condition (eV)
B substituting corner N atom	0.114675967	0.690245512
B substituting border N atom	-0.361015033	0.214554512
B substituting middle N atom	-0.012321033	0.563248512
B addition	0.805205085	0.805205085
B substituting corner C atom	-1.683875675	-2.451301735
B substituting middle C atom	-1.592727675	-2.360153735

**Table 10: Formation energies for C and N self-doping at T=298.15 K**

	Formation energy in the C rich condition (eV)	Formation energy in the N rich condition (eV)
N substituting corner C atom	4.730999358	3.388003752
N substituting middle C atom	4.647334358	3.304338752
N addition	3.034424118	2.458854572
C substituting corner N atom	-0.630512358	0.712483248
C substituting border N atom	0.875104642	2.218100248
C substituting middle N atom	-0.705011358	0.637984248
C addition	1.828442759	2.59586882

**Table 11: Formation energies for O doping at T=298.15 K**

	Formation energy in the C rich condition (eV)	Formation energy in the N rich condition (eV)
O substituting corner N atom	0.64266456	1.218234105
O substituting border N atom	-1.78068644	-1.205116895
O substituting middle N atom	-0.66826244	-0.092692895
O substituting middle C atom	3.281619918	2.514193857
O substituting corner C atom	6.083151918	5.315725857
O addition	2.506775677	2.506775677

**Table 12: Formation energies for Si doping at T=298.15 K**

	Formation energy in the C rich condition (eV)	Formation energy in the N rich condition (eV)
Si substituting corner N atom	1.898465686	2.474035231
Si substituting border N atom	1.396327686	1.971897231
Si substituting middle N atom	1.027639686	1.603209231
Si substituting corner C atom	-0.665083956	-1.432510016
Si substituting middle C atom	0.776707044	0.009280984
Si addition	0.668966804	0.668966804

**Table 13: Formation energies for P doping at T=298.15 K. “\*” denotes nonequivalent substitutions of middle C atoms due to the stacking configuration. This nonequivalent substitution leads to the higher hybridization between layers and the distortion of the in-plane symmetry of the system.**

	Formation energy in the C rich condition (eV)	Formation energy in the N rich condition (eV)
P substituting corner N atom	0.566464221	1.142033767
P substituting border N atom	-0.367164779	0.208404767
P substituting middle N atom	1.113167221	1.688736767
P substituting corner C atom	0.72520458	-0.042221481
P substituting middle C atom*	1.61316158	0.845735519
P substituting middle C atom*	0.85102058	0.083594519
P substituting corner C atom	0.28852658	-0.478899481
P addition	0.419667339	0.419667339

Due to the difference in nature of the atoms under consideration used to dope the system, Tables 9, 10, 11, 12 and 13 do not provide a general pattern to explain which N atoms are energetically preferred to be replaced (there are three nonequivalent N atoms in the system). Nevertheless, for B, O and P the substitution of the border N atom is energetically preferred. This behavior is due to the fact that the C-N bond is very strong. Then, three C-N bonds are broken when a corner or middle N atom is replaced, while the replacement of a border N atom only requires the elimination of two C-N bonds (see Figure 35 panel a). At this point is important to mention that the negative formation energy obtained for O replacing a middle N atom is due to a reconstruction of the in-plane symmetry of the system (after relaxation of the system, the O atom only binds to two of the C atoms).

Now, Table 10 shows that for the C self-doping case, it is energetically preferred to replace middle and corner N atoms, which are atoms with three C-N bonds and even though these are very strong bonds, the substitution of a corner or middle N atom with C atom generates three C-C bonds which are stronger than the C-N bond. In order to test this last idea, in Figure 36,

we have plot the charge density redistribution using equation (4.1) for a system where the corner N atom has been replaced by a C atom. Indeed the higher accumulation of charge between the C-C bonds than that between the C-N bonds indicates a stronger C-C covalent bond ( see Figure 36).

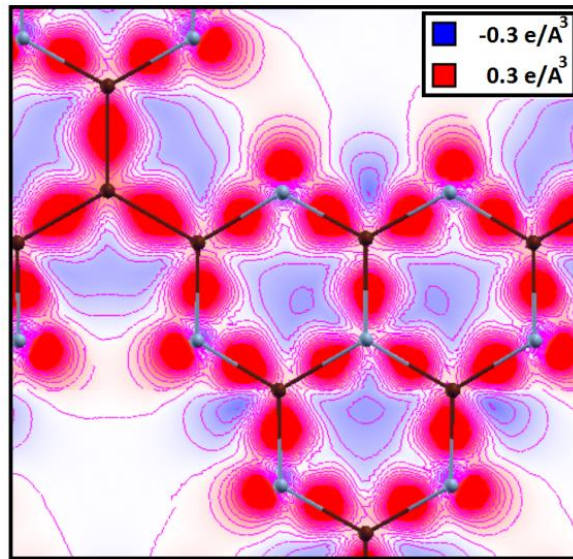


**Figure 36: Valence charge density redistribution upon formation of the system where the corner N atom has been replaced by C. Blue and red spots denotes depletion and excess of charge respectively. Grey and brown spheres denote N and C atoms respectively.**

For the C replacement, the results in Tables 9, 12 and 13 show negative formation energy for B, Si and P. P and Si are the biggest atoms in the system and highly distort the lattice when replacing a C atom, causing hybridization between layers and reducing the doping formation energy of the system. As an example of this behavior, we have included the formation energy for the two replacements of nonequivalent C atoms by P atoms (these two C atoms are nonequivalent due to the layer stacking configuration of the system as discussed earlier). These results are shown in Table 13, where it can be seen that the system with higher in-plane lattice

distortion has lower formation energy. In general the replacement of the corner C atom is energetically preferred due to the weaker covalent bond with the corner N atom, as already mentioned and shown in Figure 35 panel **b**. It is important to mention that the replacement of middle C atoms by O is the only case where the replacement of middle C atoms is energetically preferred. This is due to the fact that the replacement of the middle C with O leads to an in-plane reconstruction, breaking the g-C<sub>3</sub>N<sub>4</sub> symmetry. For this case, after optimizing the position of the atoms in the system, the O atom only binds to 2 N atoms. This results lead us to the conclusion that the substitution of C and N atoms is thermodynamically preferred over the addition of dopants to the dangling bonds.

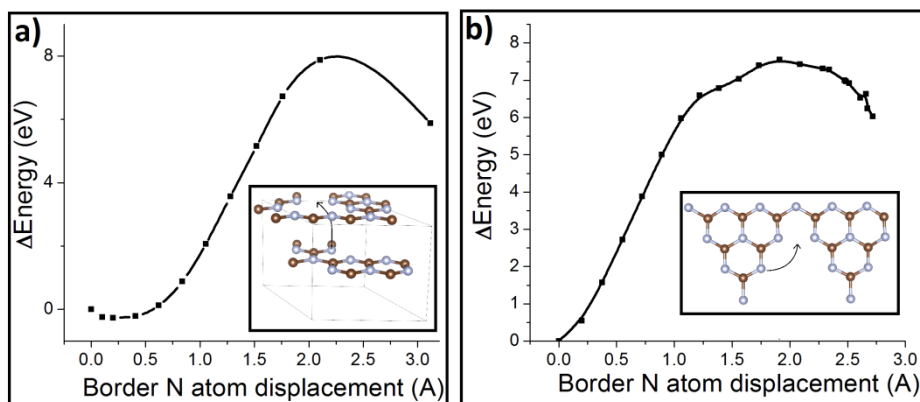


**Figure 37: Energy barrier for N border atom detachment and transfer to the nearest dangling bonds. Panel a: detachment and transfer to upper layer dangling bonds. Panel b: detachment and transfer to in-plane closest dangling bonds. The inserted figures show the position of the N atom in the initial state, while the arrow indicates the position of the N atom in the final state.**

Even though the previous results indicates a thermodynamic preference for the C and N replacement over the addition of dopants to the system, more specific to the dangling bonds, the replacement of a C or N atom is a complicated process involving detachment barriers that may make these substitutions kinetically unfavorable. With this idea in mind, in Figure 37 we present

our results on the activation energy barrier for the detachment of a border N atom and its displacement to the closest dangling bonds (to the upper or in its own layer). As it can be seen from the figure, the detachment of N, in both cases, involves very high energy barrier (8 eV), implying very low rates of such a detachment. Therefore, even though the substitution of C and N upon the doping are thermodynamically more favorable than the dopant addition to the dangling bonds, the latter, the latter are more favorable in terms of kinetics. Based on this, both process will be considered.

#### **4.2.3 Effects on the Electronic Structure of the System due to the Addition of Dopants to the Dangling Bonds in g-C<sub>3</sub>N<sub>4</sub>**

As mentioned earlier, the dangling bonds are the most reactive sites of the system for the addition of a dopant. We will start our analysis by studying the valence charge density redistribution upon the addition of an atom. Due to the high electronegativity of N, when an atom binds to the dangling bonds a donation of electron from the added atom towards the N occurs. This excess of electrons is localized in the nearest N and C atoms as  $p_z$ -states. As an example, the charge density redistribution upon addition of B is shown in Figure 38. We should mentioned that this mechanism and the valence charge density redistribution results are analogous for all the other dopants considered in this work (addition of C, N, O, Si and P). That will not be shown.

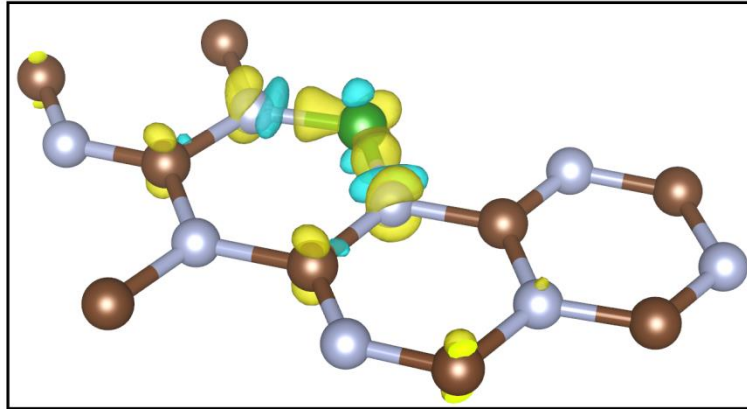


**Figure 38: Valence charge density redistribution upon binding of B to the N's dangling bonds. Yellow and blue surfaces denote accumulation and depletion of charge respectively. The isosurface corresponds to  $\pm 0.15$   $e/\text{\AA}^3$ . Brown, grey and green spheres denote C, N and B atoms respectively.**

The total density of states (TDOS) of all the doped system was calculated within the GW approximation and is shown in Figure 39, revealing that the system becomes metallic when a dopant (B, C, N, O, Si or P) is added to the N's dangling bonds. It is important to note that the metallic character of the system comes from the introduction of occupied states in the middle of the band gap or below the conduction band, depending on the case. The C self-doping is an exception, where the band gap is reduced due to the creation of occupied states in the middle of the band gap, becoming a smaller band gap semiconductor.

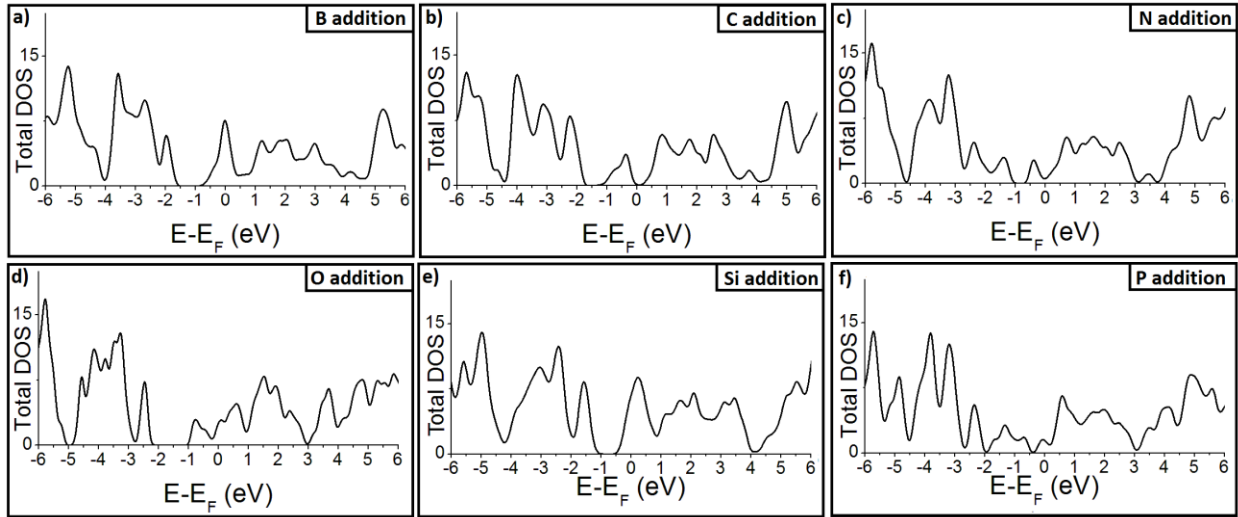


**Figure 39: Total DOS for the doped systems under consideration. Panel a: addition of B to the dangling bonds. Panel b: addition of C to the dangling bonds. Panel c: addition of N to the dangling bonds. Panel d: addition of O to the dangling bonds. Panel e: addition of Si to the dangling bonds. Panel f: addition of P to the dangling bonds.**

Going back to Figure 38, it can be seen that the already mentioned  $p_z$ -states population of C and N atoms in the system may be the reason of the metallic behavior of the doped systems depicted in Figure 39. In order to test this idea, we have calculated the local density of states (LDOS) projection over the  $p_x$ ,  $p_y$  and  $p_z$ -states for all the atoms in the unit cell. Due to the fact that results on the LDOS projection leads to the same conclusion in all the studied cases (addition of B, C, N, O, Si and P), we will only present our results for the addition of C to the dangling bonds.

Figure 40 presents the  $p_x$ ,  $p_y$  and  $p_z$  LDOS projections for the first and second border N neighbor and for the first corner C atom neighbor. From the figure it can be seen that the peak (between -1 and 0 eV) in the middle of the band gap (see Figure 39 panel **b**) has its biggest contribution coming from the second C border neighbor atom (Figure 40 panel **a**). The second contributions comes from the first neighbor N border atom (Figure 40 panel **c**), while the

contribution coming from second neighbors N border atom (Figure 40 panel **b**) is negligible as expected (based on the valence charge density redistribution result depicted in Figure 38). These results allows us to conclude that the occupied states in the middle of the band gap give rise from the creation and population of  $p_z$ -states on the first and second neighbor atoms to the dopant.

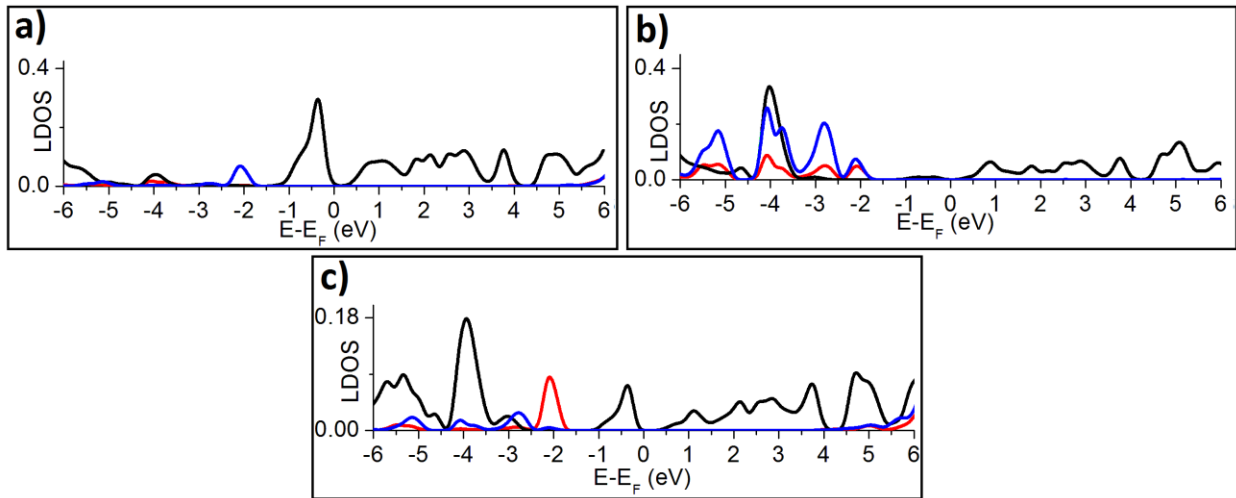


**Figure 40:** Projected LDOS for the system where a C atom has been adsorbed on the dangling bonds of  $g\text{-C}_3\text{N}_4$ . Black line:  $p_z$  states, blue line:  $p_x$  states, red line:  $p_y$  states. Panel a: projected LDOS for corner C atom (first C neighbor to the added C atom). Panel b: projected LDOS for border N atom (second N neighbor to the added C atom). Panel c: projected LDOS for border N atom (first N neighbor to the added C atom).

#### 4.2.4 Results on C and N Substitution

Our results indicate that the  $g\text{-C}_3\text{N}_4$  becomes metallic when any C atom in the system is replaced with any of the dopants atoms under consideration. An exception is the O doping where the semiconductor character of the system is maintained and the band gap is reduced to 2 eV (see Figure 41 panel **a**), which is in good qualitative agreement with experiments[121]. The replacement of corner C atom by O leads to a small elongation of one of the O-(border N) bonds, maintaining the original  $g\text{-C}_3\text{N}_4$  geometry, see Figure 41 panel **a** inserted figure. While the replacement of a middle C atom leads to the breaking of one of the O-(border N) bonds and the

high distortion of the g-C<sub>3</sub>N<sub>4</sub> geometry (see Figure 41 panel **b** inserted figure), which surprisingly barely increase the 2.7 eV band gap of the original g-C<sub>3</sub>N<sub>4</sub> system, see Figure 41 panel **b**.

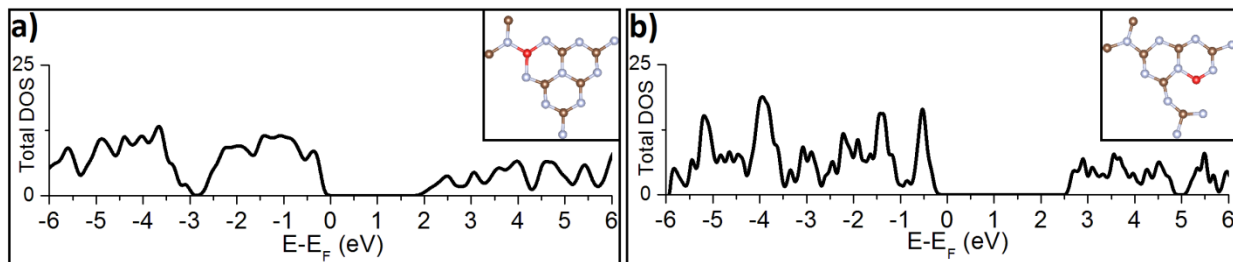


**Figure 41:** Total density of states for the system where one C has been replaced by one O atom. Panel **a**: O replacing corner C atom, no O-N bond is broken, only a small elongation of one of the O-(border N) bond is observed. Panel **b**: replacement of the middle C atom by O, rupture of one O-N bond is observed, leading to a high distortion of the original g-C<sub>3</sub>N<sub>4</sub> structure

The band gap reduction, to 2 eV, observed in Figure 41 panel **a**, originates from the charge transfer from the N atoms towards the O (the charge transfer is only appreciable for the first neighbors. According to our calculations, we observed a depletion of 0.176 electron in the p orbitals of the border N atoms) and the back donation of electrons toward the p<sub>z</sub>-states of N. In order to support this idea, we have calculated the LDOS projection over p<sub>x</sub>, p<sub>y</sub> and p<sub>z</sub> of the corner N atom (first neighbor to the O replacing the corner C atom). These results are plotted in Figure 42 panel **a**, also the results of the projected LDOS over p-states of the corner N atom in pristine g-C<sub>3</sub>N<sub>4</sub> have been included (Figure 42 panel panel **b**) for comparison purposes. As can be seen, the depletion of charge in the p orbitals generates unoccupied p<sub>x</sub>- and p<sub>y</sub>-states below the conduction band (peaks at 2.5 eV in Figure 42 panel **a**), while the back donation of electrons creates p<sub>z</sub>-states above the valence band (peak at -0.5 eV in Figure 42 panel **a**). As a consequence the band gap of the system is reduced.

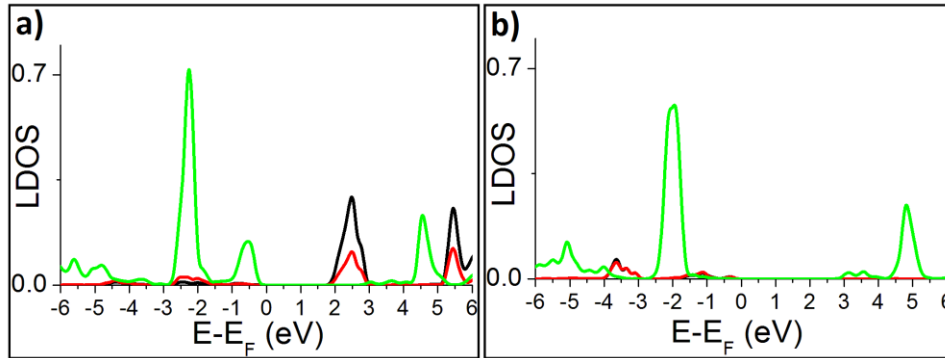


**Figure 42: Local density of states projection on  $p_x$ ,  $p_y$  and  $p_z$  states. Black lines:  $p_x$  states, red lines  $p_y$  states, green lines  $p_z$  states. Panel a: Local density of states of corner N atom first neighbor to O, panel b: Local density of states of corner N with no O neighbors.**

On the other hand, the substitution of N introduces states in the middle of the band gap, making the system metallic for all the dopants under consideration except for the case where N is replaced by B and P, where the system maintains its semiconductor character. The total DOS results corresponding to the replacement of N with B, shows that the band gap is reduced to 1.5 eV when B is replacing a border N atom. For the two other cases (replacement of corner and middle n atoms) the system becomes metallic. On the other hand, the results on N replacement with P show a reduction in the band gap in the range of 1.8 to 2.5 eV depending on the replaced N atom.

In Figure 43 we show the results on the electronic structure corresponding to the replacement of border N atom by B (panel **a**) and P (panel **b**), where it can be seen the above mentioned band gap reduction. Replacement of the border N atoms was chosen to be shown in this work because constitute the lowest formation energy for all the cases under consideration.

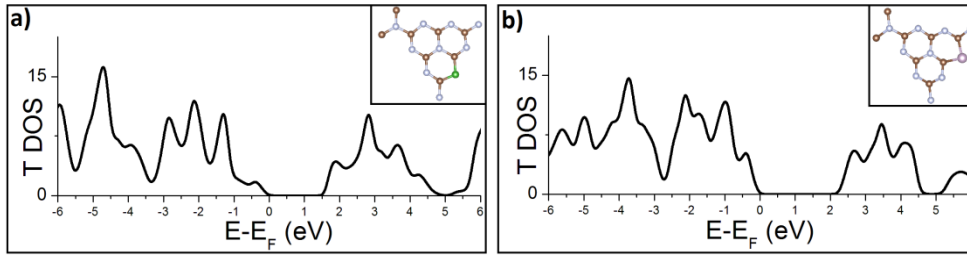


Figure 43: Total DOS for border N atom replaced by B and P. Panel a: B replacement, panel b: P replacement. Inserted figures show the system's structure.

The mechanism responsible for the reduction of the band gap observed in Figure 43 is similar to the one depicted in the O replacement of C already mentioned above, this is:  $p_z$ -states of neighbor atoms to the dopant become occupied. These new populated  $p_z$ -states are localized above the valence band, resulting in the reduction of the band gap. This behavior is depicted in Figure 44 panel a, where the creation of  $p_z$ -states between -2 and 0 eV on the first C neighbor (a middle C atom) to the dopant (in this case B) are shown (the LDOS of a second middle C atom with no B neighbor is shown in Figure 44 panel b for comparison purposes). At this point we should mention that the results concerning N replacement by P will not be shown due to its high resemblance with the ones already shown in Figure 44.

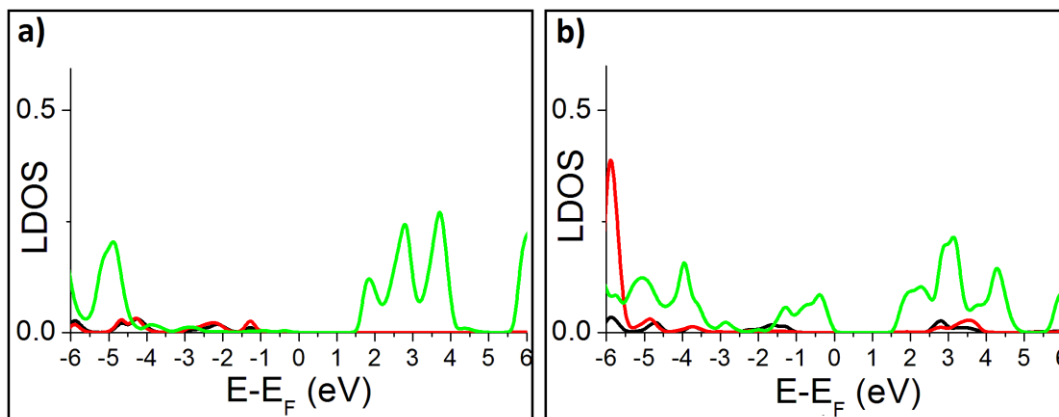


Figure 44: Middle C atom LDOS. Black, red and green lines denote  $p_x$ ,  $p_y$  and  $p_z$  states respectively. Panel a: middle C atom with no B neighbors, panel b: middle C atom coordinated to one B atom.

In order to conclude with this sub section, it is worth mentioning two experimental works: In the first one, the authors on [122] were able to dope  $g\text{-C}_3\text{N}_4$  with P, finding that the system becomes metallic. Also they were able to determine that the P atom were coordinated to N atoms, where the authors suggests a C replacement. We quote “Thus the phosphorus heteratoms most probably replace the corner or bay carbon in the structure forming P-N bonding in the doped  $\text{C}_3\text{N}_4$  framework”. These results are in good agreement with our results shown in the previous subsection, where P doped  $g\text{-C}_3\text{N}_4$  shows a metallic DOS structure for all the cases except for N replacement, leaving P doped  $g\text{-C}_3\text{N}_4$  as a good candidate for photo catalytic purposes. On the other hand, the authors on [119] have reported a negligible change in the band gap of the B doped  $g\text{-C}_3\text{N}_4$ . The authors suggest the attachment of B to corner N atoms, forming of  $\text{NB}_2$  species at the corners of the Tri-s-triazine structure. Our current results are not in agreement with the authors in Ref. [119] and further analysis of the band structure of the all possible configurations of the B doped  $g\text{-C}_3\text{N}_4$  is needed before a conclusion can be made.

#### **4.2.5 Results on the Effects of Co-Doping**

The effects of doping the  $g\text{-C}_3\text{N}_4$  system with two atoms where extensively studied with the idea that the interaction between different dopants could alter the mechanisms responsible for the change in the band gap. In order to study such effect, the size of the supercell was doubled, maintaining the percentage of dopant concentration constant. Unfortunately, the results show that the interaction between different dopants is negligible. Furthermore, our results show that the DOS changes according to the individual contributions of the two dopants. As an example in Figure 45 we show a comparison between P, B and P-B doped  $g\text{-C}_3\text{N}_4$ . Figure 45 Panel c shows

that the P-B doped systems maintains the 1.5 eV band gap achieved in B doped system (panel **a** of Figure 43 and Figure 45 ). On the other hand, from Figure 45 panel **c**, is clear that the 2.7 original g-C<sub>3</sub>N<sub>4</sub> band gap is reduced due to the creation and population of states above the valence band, which are also present in the B and P doping, see panels **a** and **b** of Figure 45.

It should be mention that the DOS corresponding to N replacement by P depicted on panel **b** of Figure 43 and Figure 45 differs from each other because the replaced border N atoms in both cases are nonequivalent because a relatively large P atom causes hybridization between layers.

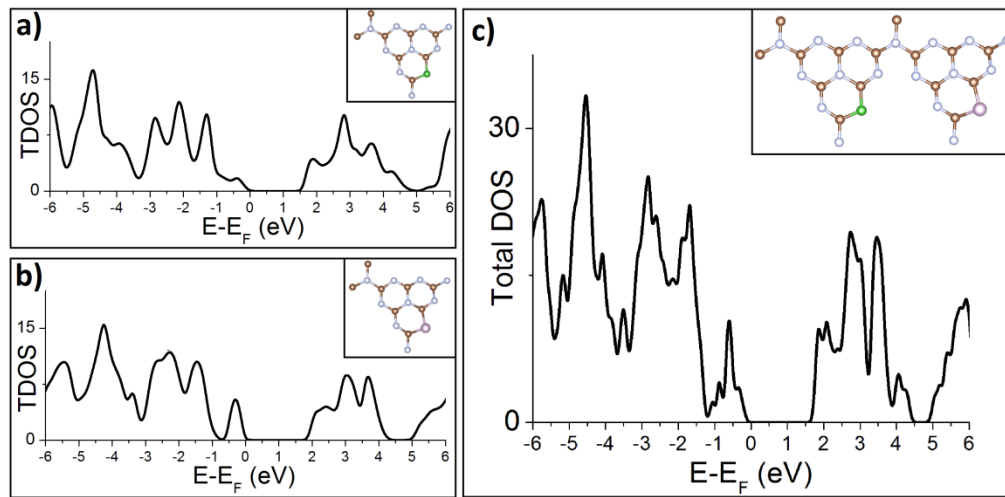


**Figure 45: DOS comparison between B and P replacing a border N atom. Panel a: B doping, panel b: P doping, panel c: B and P co-doping. The inserted figures show the geometry of the systems under consideration.**

The low interaction between dopants has its origins in the local effect of the dopant. As we have shown before, the transfer of electrons from the dopant to the system and the change in the LDOS is a local effect, affecting only the first and second neighbors. Therefore, the

interaction between dopants does not occur unless they are separated by no more than two neighbors, which will require a high concentration of dopants.

#### 4.2.6 Conclusions

The results on the formation energy of the doped systems indicate that the replacement of C and N atoms is thermodynamically preferred over the addition of dopants to the g-C<sub>3</sub>N<sub>4</sub> dangling bonds. However, the results show high kinetic energy barriers for the removal of C and N atoms (these processes are involved in the replacement of C and N by the doping agent), indicating that the addition of atoms to the system is a possible scenario for the doped g-C<sub>3</sub>N<sub>4</sub>.

Concerning the effects of doping on the electronic structure, we have shown that the addition of dopants to the system generates the donation of electrons from the dopant to the system, resulting in the population of p<sub>z</sub>-states of the first N and C neighbors to the dopant. As consequence, the system becomes metallic for all the doped systems under consideration. The energy of the populated states depends on the dopant under consideration.

For the N replacement, we show that the semiconductor character of the system is maintained only for the cases where the N atoms were replaced by B or P. Our results are in good agreement with the experiments in the case of P doping. Concerning the C replacement with O, we show that the system maintains its semiconductor character and the band gap is reduced. This is in good qualitative agreement with the experiments.

Finally, for the case of co-doping, our results show that the DOS changes according to the individual contributions of the two dopants. This behavior is due to the fact that the transfer

of electrons between dopant - system and the consequent change in the LDOS are effects localized to the first and second neighbors of the dopant.

## LIST OF REFERENCES

- 
- [1] Handbook of fuel cells: fundamentals, technology, and applications ( Eds: W. Vielstich, A. Lamm, H. A. Gasteiger). Chichester, England; Hoboken, N. J. : Wiley, (2003)
- [2] R. R. Adzic, J. Zhang, K. Sasaki, M. B. Vukmirovic, M. Shao, J. X. Wang, A. U. Nilekar, M. Mavrikakis, J. A. Valerio, and F. Uribe, *Top. in Catal.* **46**, 249 (2007)
- [3] J. Zhang, M. B. Vukmirovic, Y. Xu, M. Mavrikakis, R. R. Adzic, *Ang. Chem. Intern. Ed.* **44**, 2132 (2005)
- [4] A. Nilekar, M. Mavrikakis, *Surf. Sci.* **602**, L89 (2008)
- [5] W.-P. Zhou, X. Yang, M. B. Vukmirovic, B. E. Koel, J. Jiao, G. Peng, M. Mavrikakis, R. R. Adzic, *J. Am. Chem. Soc.* **131**, 12755 (2009)
- [6] K. Gong, W.-F. Chen, K. Sasaki, D. Su, M. B. Vukmirovic, W. Zhou, E. L. Izzo, C. Perez-Acosta, P. Hirunsit, P. B. Balbuena, R. R. Adzic, *J. Electroanal. Chem.* **649**, 232 (2010)
- [7] P. J. Boddy, *J. Electrochem. Soc.* **115**, 199 (1968)
- [8] A. Fujishima, K. Honda, *Nature* **238**, 37 (1972)
- [9] A. Kudo, Y. Miseki, *Chem. Soc. Rev.* **38**, 253 (2009)
- [10] A. L. Linsebigler, G. Lu, J. T. Yates, *Chem. Rev* **95**, 735 (1995)
- [11] K. Hashimoto, H. Irie, A. Fujishima, *Japanese J. App. Phys* **44**, 8296 (2005)

- 
- [12] T. Ikeda, S. Fujiyoshi, H. Kato, A. Kudo, H. Onishi, *J. Phys. Chem. B* **110**, 7883 (2006)
- [13] Y. Matsumoto, K. Ueda, K. Tomita, Y. Sekine, Y. Miura, N. Yamatani, M. Kakihana, *J. Ceramic Soc. Japan* **117**, 1191 (2009)
- [14] M. Born, R. Oppenheimer, *Annalen der Physik* **389**, 457 (1927)
- [15] D. R. Hartree, *Mathematical Proceedings of the Cambridge Philosophical Society* **24**, 89 (1928)
- [16] D. R. Hartree, *Mathematical Proceedings of the Cambridge Philosophical Society* **24**, 111 (1928)
- [17] J. C. Slater, *Phys. Rev.* **35**, 210 (1929)
- [18] V. A. Fock, *Z. Physik* **61**, 126 (1930)
- [19] V. A. Fock, *Z. Physik* **62**, 795 (1930)
- [20] P. Hohenberg, W. Kohn, *Phys. Rev. B* **136**, 864–871 (1964)
- [21] J. Kohanoff, “Electronic Structure Calculations for Solid and Molecules: theory and computational methods”, Cambridge University Press, New York (2006)
- [22] W. Kohn, L. Sham, *Phys. Rev. B* **15**, 2884-2901 (1965)
- [23] L. Nedin, B. I. Lundqvist, *J. Phys. C: Solid St. Phys* **4**, 2064-2083 (1971)
- [24] J. P. Perdew, A. Zunger, *Phys. Rev. B* **23**, 5048-5079 (1981)

- 
- [25] J. P. Perdew, K. Burke, M. Ernzerhof, *Phys. Rev. Lett.* **77**, 3865–3868 (1996)
- [26] L. Hedin, *Phys. Rev* **139**, 796 (1965)
- [27] R. Adzic, in *Electrocatalysis* (Edited by J. Lipkowski and P. Ross) Wiley/VCH Inc., New York, (1998)
- [28] A. Eichler, F. Mittendorfer, J. Hafner, *Phys. Rev. B* **62**, 4744 (2000)
- [29] J. K. Nørskov, J. Rossmeisl, A. Logadottir, L. Lindqvist, J. R. Kitchin, T. Bligaard, H. Jónsson, *J. Phys. Chem. B* **108**, 17886 (2004)
- [30] Y. Okamoto and O. Sugino, *J. Phys. Chem. C* **114**, 4473 (2010)
- [31] J. Rossmeisl, A. Logadottir, J.K. Nørskov, *J. Chem. Phys.* **319**, 178 (2005)
- [32] F. Abild-Pedersen, J. Greeley, F. Studt, J. Rossmeisl, T. R. Munter, P. G. Moses, E. Skúlason, T. Bligaard, and J. K. Nørskov, *Phys. Rev. Lett.* **99**, 016105 (2006)
- [33] V. Stamenkovic, B. S. Mun, K. J. J. Mayrhofer, P. N. Ross, N. M. Markovic, J. Rossmeisl, J. Greeley, J. K. Nørskov, *Angewandte Chemie* **118**, 2963 (2006)
- [34] Computational Chemistry Comparison and Benchmark Data Base, National Institute of Standards and Technology web site: [cccbdb.nist.gov](http://cccbdb.nist.gov).
- [35] G. S. Karlberg, J. Rossmeisl and J. K. Nørskov, *Phys. Chem. Chem. Phys.* **9**, 5158 (2007)
- [36] O. Savadogo, K. Lee, K. Oishi, S. Mitsushima, N. Kamiya and K. -I. Ota, *Electrochem. Commun.* **6**, 105 (2004)

- 
- [37] H. Liu, W. Li, and A. Manthiram, *Appl. Catalysis B: Environ.* **90**, 184 (2009)
- [38] W. Wang, D. Zheng, C. Du, Z. Zou, X. Zhang, B. Xia, H. Yang, D. L. Akins, *J. Power Sources.* **167**, 243 (2007)
- [39] M. H. Shao, T. Huang, P. Liu, J. Zhang, K. Sasaki, M. B. Vukmirovic, and R. R. Adzic, *Langmuir* **22**, 10409 (2006)
- [40] A. V. Ruban, H. L. Skriver, J. K. Nørskov, *Phys. Rev. B* **59**, 15990 (1998)
- [41] E. J. Lamos and P. B. Balbuena, *J. Chem. Theor. Comput.* **2**, 1388 (2006)
- [42] Y. Suo, L. Zhuang, J. Lu, *Angew. Chem. Int. Ed.* **46**, 2862 (2007)
- [43] V. Tripković, E. Skúlason, S. Siahrostami, J. K. Nørskov, J. Rossmeisl, *Electrochem. Acta* **55**, 7975 (2010)
- [44] P. Hirunsit and P. B. Balbuena, *Surf. Sci.* **603**, 3239 (2009)
- [45] H. Lio, A. Manthiram, *Energy Environ. Sci.* **2**, 124 (2009)
- [46] G. Kresse and J. Furthmüller, *Comput. Mat. Sci.* **6**, 15 (1996)
- [47] G. Kresse, and J. Joubert, *Phys. Rev. B* **59**, 1758 (1999)
- [48] J. P. Perdew, S. Burke, M. Ernzerhof, *Phys. Rev. Lett.* **77**, 3865 (1996)
- [49] A. Kokalj, *Comp. Mater. Sci.* **28**, 155 (2003)

- 
- [50] J. Rossmeisl, G. S. Karlberg, T. Jaramillo, J. K. Nørskov, *Faraday Discuss.* **140**, 337 (2008)
- [51] J. X. Wang, F. A. Uribe, T. E. Springer, J. Zhang, R. R. Adzic, *Faraday Discuss.* **140**, 347 (2008)
- [52] J. Rossmeisl, A. Logadottir, J. K. Nørskov, *Chem. Phys.* **319**, 178 (2005)
- [53] D. C. Ford, A. U. Nilekara, Y. Xu, M. Mavrikakis, *Surf. Sci.* **604**, 1565 (2010)
- [54] Y. Sha, T. H. Yu, Y. Liu, B. V. Merinov, and W. A. Goddard III, *Phys. Chem. Lett.* **1**, 856 (2010)
- [55] Y.-C. Wei, C.-W. Liu, Y.-W. Chang, C.-M. Lai, P.-Y. Lim, L.-D. Tsai, and K.-W. Wang, *Intern. J. Hydrogen Energy* **35**, 1864 (2010)
- [56] J. X. Wang, N. M. Markovic, R. R. Adzic, *J. Phys. Chem. B* **108**, 4127 (2004)
- [57] B. Hammer, Y. Morikawa, J. K. Nørskov, *Phys. Rev. Lett.* **76**, 2141 (1996)
- [58] F. H. B. Lima, J. Zhang, M. H. Shao, K. Sasaki, M. B. Vukmirovic, E. A. Ticianelli, R. R. Adzic, *J Solid State Electrochem* **12**, 399 (2008)
- [59] K. Gong, M. B. Vukmirovic, C. Ma, Y. Zhu, R. R. Adzic, *J. Electroanal. Chem.* **662**, 213 (2011)
- [60] M. Shao, K. Sasaki, N. S. Marinkovic, L. Zhang, R. R. Adzic, *Electrochem. Comm.* **9**, 2848 (2007)

- 
- [61] J. Zhang, F. H. B. Lima, M. H. Shao, K. Sasaki, J. X. Wang, J. Hanson, R. R. Adzic, *J. Phys. Chem. B* **109**, 22701 (2009)
- [62] D. N. Son, K. Takahashi, *J. Phys. Chem. Lett.* **116**, 6200 (2012)
- [63] S. Tominaka, T. Mommab, T. Osaka, *Electrochem Acta* **53**, 4679 (2008)
- [64] M.-H. Shao, K. Sasaki, R. R. Adzic, *J. Am. Chem. Soc.* **128**, 3526 (2006)
- [65] S. Stolbov, M. Alcántara Ortigoza, *J. Phys. Chem. Lett.* **3**, 463 (2012)
- [66] S. Zuluaga, S. Stolbov, *J. Chem. Phys* **135**, 134702 (2011).
- [67] T. Ueno, M. Sawada, K. Furumoto, T. Tagashira, S. Tohoda, A. Kimura, S. Haraguchi, M. Tsujikawa, T Oda, H. Namatame, M. Taniguchi, *Phys. Rev. B* **85**, 224406 (2012)
- [68] A. Lehnert, S. Dennler, P. Błoński, S. Rusponi, M. Etzkorn, G. Moulas, P. Bencok, P. Gambardella, H. Brune, J. Hafner, *Phys. Rev B* **82**, 094409 (2010)
- [69] T. Wadayama, N. Todoroki, Y. Yamada, T. Sugawara, *Electrochem. Comm.* **12**, 1112 (2010)
- [70] M. Shao, P. Liu, J. Zhang, R. Adzic, *J. Phys. Chem. B* **111**, 6772 (2007)
- [71] Y. Xu, A. V. Ruban, M. Mavrikakis, *J. Am. Chem. Soc.* **126**, 4717 (2003)
- [72] CRC Handbook of Chemistry and Physics, D. R. Lide, Ed. CRC Press: New York (1996)
- [73] J. Greeley, J. K. Norskov, *Electrochem. Acta* **52**, 5829 (2007)

- 
- [74] M. Li, P. Liu, R. R. Adzic, *J. Phys. Chem. Lett.* **3**, 3480 (2012)
- [75] S. R. Brankovic, J. X. Wang, R. R. Adzic, *Electrochem. Solid State Lett.* **4**, A217 (2001)
- [76] S. Stolbov, M. Alcántara Ortigoza, R. Adzic, T. S. Rahman, *J. Chem. Phys.* **130**, 124714 (2009)
- [77] A. U. Nilekar, K. Sasaki, C. A. Farberow, R. R. Adzic, M. Mavrikakis, *J. Am. Chem. Soc.* **133**, 18574 (2011)
- [78] Y. Xing, Y. Cai, M. B. Vukmirovic, W.-P. Zhou, H. Karan, J. X. Wang, R. R. Adzic, *J. Phys. Chem. Lett.* **1**, 3238 (2010)
- [79] C. Wang, D. van der Vliet, K. L. More, N. J. Zaluzec, S. Peng, S. Sun, H. Daimon, G. Wang, J. Greeley, J. Pearson, et al, *Nano Lett.* **11**, 919(2011)
- [80] M.Ø. Pedersen, S. Helveg, A. Ruban, I. Stensgaard, E. Lægsgaard, J. K. Nørskov, F. Besenbacher, *Surf. Sci.* **426**, 395(1999)
- [81] S. Stolbov, S. Zuluaga, *J. Phys. Chem. Lett.* **4**, 1537 (2013)
- [82] S. Stolbov, S. Hong, A. Kara, T. S. Rahman, *Phys. Rev.* **72**, 155423 (2005)
- [83] N. Alonso-Vante, H. Tributsch, *Nature* **323**, 431 (1986)
- [84] D. Cao, A. Wieckowski, J. Inukai, N. Alonso-Vante, *J. of Electrochem. Soc.* **153**, A869 (2005)

- 
- [85] K. N. Loponov, V. V. Kriventsov, K. S. Nagabhushana, H. Boennemann, D. I. Kochubey, E. R. Savinova, *Catalysis Today* **147**, 260 (2009)
- [86] G. Zehl, G. Schmithals, A. Hoell, S. Haas, C. Hartnig, I. Dorbandt, P. Bogdanoff, S. Fiechter, *Angew. Chem. Int. Ed* **46**, 7311 (2007)
- [87] N. Alonso-Vante, P. Bogdanoff, H. Tributsch, *Journal of Catalysis* **190**, 240 (2000)
- [88] P. Nekooi, M. K. Amini, *Electrochim. Acta* **55**, 2386 (2010)
- [89] I. V. Malakhov, S. G. Nikitenko, E. R. Savinova, D. I. Kochubey, N. Alonso-Vante, *J. Phys. Chem. B* **106**, 1670 (2002)
- [90] N. Alonso-Vante, I.V. Malakhov, S.G. Nikitenko, E.R. Savinova, D.I. Kochubey, *Electrochimica Acta* **47**, 3807 (2002)
- [91] Y. Hara, N. Minami, H. Itagaki, *Applied Catalysis A: General* **340**, 59 (2008)
- [92] S. Zuluaga, S. Stolbov, *J. of Phys. Con. Matt* **24**, 345303 (2012)
- [93] S. Stolbov, *J. of Phys. Chem. C* **116**, 7173 (2012)
- [94] G. Liu, H. Zhang, J. Hu, *Electrochem. Comm* **9**, 2643 (2007)
- [95] R. W. F. Bader, "Atoms in Molecules: A Quantum Theory", Oxford University Press., New York (1994)
- [96] K. Momma, F. Izumi, *J. Appl. Crystallogr.* **44**, 1272 (2011)

- 
- [97] F. Dassenoy, W. Vogel, N. Alonso-Vante, *J. Phys. Chem. B* **106**, 12152 (2002)
- [98] S. Stolbov, *Phys Rev. B* **82**, 155463 (2010)
- [99] W. Vogel, P. Kaghazchi, T. Jacob, N. Alonso-Vante, *J. Phys. Chem. C* **111**, 3908 (2007)
- [100] C. Delacôte, A. Bonakdarpour, C. M. Johnston, P. Zelenay, A. Wieckowski, *Faraday Discuss.* **140**, 269 (2008)
- [101] V.I. Zaikovskii, K.S. Nagabhushana, V.V. Kriventsov, K.N. Loponov, S.V. Cherepanova, R.I. Kvon, H. Bönemann, D.I. Kochubey, E.R. Savinova, *J. Phys. Chem. B* **110**, 6881 (2006)
- [102] M.-Y. Shen, S.-P. Chiao, D.-S. Tsai, D. P. Wilkinson, J.-C. Jiang, *Electrochim. Acta* **54**, 4297 (2009)
- [103] A. Racz, P. Bele, C. Cremers, U. Stimming, *J. Appl. Electrochem.* **37**, 1455 (2007)
- [104] K. S. Nagabhushana, E. Dinjus, H. Bönemann, V. Zaikovskii, C. Hartnig, G. Zehl, I. Dorbandt, S. Fiechter, P. Bogdanoff, *J. Appl. Electrochem.* **37**, 1515 (2007)
- [105] A. Garsuch, X. Michaud, G. Wagner, O. Klepel, J.R. Dahn, *Electrochim. Acta* **54**, 1350 (2009)
- [106] C. M. Johnston, D. Cao, J.H. Choi, P. K. Babu, F. Garzon, P. Zelenay, *J. Electroanalyt. Chem.* **662**, 257 (2011)
- [107] P.K. Babu, A. Lewera, J.H. Chung, R. Hunger, W. Jaegermann, N. Alonso-Vante, A. Wieckowski, E. Oldfield, *J. Am. Chem. Soc.* **129**, 15140 (2007)

- 
- [108] G.A. Tritsarlis, J.K. Nørskov, J. Rossmeisl, *Electrochimica Acta* **56**, 9783 (2011)
- [109] Y. Feng, A. Gago, L. Timperman, N. Alonso-Vante, *Electrochimica Acta* **56**, 2009 (2011)
- [110] K. Maeda, K. Domen, *J. Phys. Chem. Lett.* **1**, 2655 (2010)
- [111] R. M. Navarro, M. C. Alvarez-Galv´an, J. A. Villoria de la Mano, S. M. Al-Zahrani, J. L. G. Fierro, *Energy Environ. Sci.* **3**, 1865 (2010)
- [112] F. E. Osterloh, B. A. Parkinson, *MRS Bull.* **36**, 17 (2011)
- [113] X. Wang, K. Maeda, A. Thomas, K. Takanebe, G. Xin, J. M. Carlsson, K. Domen, M. Antonietti, *Nature Mater.* **8**, 76 (2009)
- [114] D. L. Yu, F. R. Xiao, T. S. Wang, Y. J. Tian, J. L. He, D. C. Li, W. K. Wang, *J. Mater. Sci. Lett.* **19**, 553 (2000)
- [115] Y. Xu, S-P. Gao, *Int. J. Hydrogen Energy* **37**, 11072 (2012)
- [116] M. J. Bojdys, J. O. Muller, M. Antonietti, A. Thomas, *Chem. Eur. J.* **14**, 8177 (2008)
- [117] X. Zhang, X. Xie, H. Wang, J. Zhang, B. Pan, Y. Xie, *J. Am. Chem. Soc.* **135**, 18 (2013)
- [118] F. Dong, L. Wu, Y. Sun, M. Fu, Z. Wu, S. C. Lee, *J. Mater. Chem.* **21**, 15171 (2011)
- [119] S. C. Yan, Z. S. Li, Z. G. Zou, *Langmuir* **26**, 3894 (2010)
- [120] G. Dong, K. Zhao, L. Zhang, *Chem. Commun.* **48**, 6178 (2012)
- [121] J. Li, B. Shen, Z. Hong, B. Lin, B. Gao, Y. Chen, *Chem. Commun.* **48**, 12017 (2012)

- 
- [122] Y. Zhang, T. Mori, J. Ye, M. Antonietti, *J. Am. Chem. Soc.* **132**, 6294 (2010)
- [123] G. Liu, P. Niu, C. Sun, S. C. Smith, Z. Chen, G. Q. Lu, H-M. Cheng, *J. Am. Chem. Soc.* **132**, 11642 (2010)
- [124] S.-W. Cao, Y.-P. Yuan, J. Fang, M. M. Shahjamal, F. Y. C. Boey, J. Barber, S. C. J. Loo, C. Xue, *Int. J. Hydrogen Energy* **38**, 1258 (2013)
- [125] X. Wang, X. Cheng, A. Thomas, X. Fu, M. Antonietti, *Adv. Mater.* **21**, 1609 (2009)
- [126] L. Ge, C. Han, J. Liu, Y. Li, *Appl. Catal. A: General* **409-410**, 215 (2011)
- [127] S. Stolbov, S. Zuluaga, *J. Phys.: Condens. Matter* **25**, 085507 (2013)
- [128] S. Grimme, *J. Comput. Chem.* **27**, 1787 (2006)
- [129] C. G. Van de Walle, J. Neugebauer, *J. Appl. Phys.* **95**, 3851 (2004)
- [130] J. D. Cox, D. D. Wagman and V. A. Medvedev, CODATA Key Values for Thermodynamics (New York: Hemisphere) (1989)